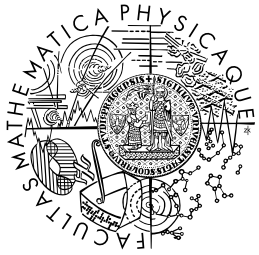

FACULTY
OF MATHEMATICS
AND PHYSICS
Charles University

MASTER THESIS

Bc. Jan Premus

Development of effective code for earthquake dynamic source simulations

Department of Geophysics

Supervisor of the master thesis:	doc. RNDr. František Gallovič, Ph.D
Study programme:	Fyzika
Study branch:	Geofyzika R9

Prague 2019

I declare that I carried out this master thesis independently, and only with the cited sources, literature and other professional sources.

I understand that my work relates to the rights and obligations under the Act No. 121/2000 Sb., the Copyright Act, as amended, in particular the fact that the Charles University has the right to conclude a license agreement on the use of this work as a school work pursuant to Section 60 subsection 1 of the Copyright Act.

In ..... date ..... signature of the author

I would like to thank to my supervisor doc. František Gallovič for invaluable help and guidance during the preparation of this thesis. Also to Alice-Agnes Gabriel, Ph.D. from LMU for the help in implementing the fast velocity weakening friction law.

I acknowledge financial support by the Charles University grant SVV-260447 and the Czech Science Foundation project 18-06716J.

Title: Development of effective code for earthquake dynamic source simulations

Author: Bc. Jan Premus

Department: Department of Geophysics

Supervisor: doc. RNDr. František Gallovič, Ph.D, Department of Geophysics

Abstract: Dynamic rupture modeling coupled with strong motion data fitting offers an insight into physical mechanisms behind earthquake sources [Gallovic et al., 2019]. Running a large number of dynamic model simulations is required due to the nonlinearity of the inverse problem. The goal of this Thesis is a development of an efficient forward solver for the dynamic inversions. The finite difference staggered grid code FD3D by Madariaga and Olsen [1998] served as a basis for the development, offering sufficient speed, but rather low accuracy. Traction at split node implementation of the fault boundary condition and perfectly matched layers as the absorbing boundary condition were required to obtain desirable accuracy. In addition to the slip weakening friction law, fast velocity weakening friction law has been implemented, increasing the applicability of the code. We test the new code FD3D_TSN using USGS/SCEC benchmarks TPV5 (slip-weakening friction) and TPV104 (fast rate weakening friction) [Harris et al., 2018], showing very good agreement with results calculated by advanced numerical codes.

Keywords: Earthquakes, Finite differences, Dynamic rupture simulation, Earthquake source

Název: Vývoj efektivního kódu pro dynamické simulace zemětřesení

Autor: Bc. Jan Premus

Katedra: Katedra geofyziky

Vedoucí práce: doc. RNDr. František Gallovič, Ph.D, Katedra geofyziky

Abstrakt: Dynamické modelování trhliny ve spojení s s vystižením silných pohybů umožňuje získat vhled do fyzikálních mechanismů kontrolujících zdroj zemětřesení [Gallovič a kol., 2019]. Nelinearita inverzního problému vyžaduje spouštění velkého množství simulací. Cílem této diplomové práce je vývoj efektivního kódu pro řešení inverzní úlohy. Původní kód FD3D od autorů Madariagy a Olsena [1998], používající konečné difference s posunutými sítěmi, nabízel dostatečnou rychlost, ale ne přesnost. Byl použit jako základ pro další vývoj. Implementace okrajové podmínky na zlomu metodou trakce v půleném uzlu (traction at split node) a absorbční podmínky pomocí metody perfektně sladěných vrstev (perfectly matched layers) bylo třeba k získání požadované přesnosti. Jako moderní alternativa ke skluzem slábnoucímu (slip weakening) zákonu tření byl implementován s rychlostí rychle slábnoucí (fast velocity weakening) zákon, což dále rozšířilo škálu jevů, které je možné modelovat. Nový kód FD3D_TSN byl otestován pomocí komunitních benchmarků USGS/SCEC [Harris a kol., 2018], konkrétně TPV5 pro skluzem slábnoucí tření a TPV104 pro tření slábnoucí s rychlostí. Výsledky vykazují velmi dobrou shodu s výsledky ostatních pokročilejších kódů.

Klíčová slova: Zemětřesení, Metoda konečných differencí, Dynamické simulace trhliny, Zemětřesný zdroj

Contents

Introduction

Most informations about eartquakes come in the form of seismograms, which is a time graph of ground motion measured at a concrete spot at the Earth's surface. Combination of two physical models is required to calculate the shape of seismogram theoretically – a model of the propagation of seismic waves and a model of the earthquake source. Pameters of these models can be acquired as a solution to an inverse problem.

The elastodynamic equation describes the propagation of seismic waves through the Earth's body at seismic wave frequencies. Izotropic rheology is a reasonable description of the material properties in the litosphere, leaving us with the distribution of the density and Lamé's coefficients as model parameters.

Seismic source can be described by models of varying complexity. The point source double couple model is on the one side of the spectrum, where the source is described by a system of equivalent forces acting at the centroid. This leads to parametrization of the source by a moment tensor, whose components are provided as a solution of the inverse problem. This approach is suitable for earthquakes happening at long distances from the seismic station (longer than the size of the fault rupture), where inverted seismograms are obtained, and low frequencies (lower than the corner frequency).

At local distances, when the size of the source is not negligible, more complicated models are required. We distinguish two groups of such models – kinematic and dynamic.

- Kinematic model describes the source as a discontinuity in the displacement (slip) at a prescribed surface in the body, defining the fault. It does not require the model parameters (time and spatial dependence of the slip) to be physically plausible, which can lead to an ambiguity of the problem.

- Dynamic models prescribe a physical condition at the fault surface. The rupture propagates spontaneously, with the slip being one of the outputs, rather then inputs of the model. Popular approximation is to consider the rupture to be a shear crack on a frictional plane embedded in an elastic material. More complex models, including complicated geometries [Ulrich et al., 2019], off-fault plasticity [Wollherr et al., 2018] or damage [Pelties et al., 2015] are also studied, but to date only in the form of the forward problem, not in an automatic inversion of seismograms.

The major obstacle in the dynamic inversion is the nonlinear relationship between model parameters and seismograms and the high computational complexity of the forward problem (rupture propagation). This limits the allowable complexity of the physical model and achievable accuracy of its numerical solution [Mirwald et al., 2019]. Vertical planar faults are used, as other geometries require numerical methods with irregular grids, increasing the time requirements beyond the boundary where the dynamic inversion is feasible. Dynamic inversions focused at cracks with eliptical shape [Herrera et al., 2017], decreasing the amount of model parameters.

This Thesis describes a development of a forward model solver for the dynamic inversion code fd3d_pt by F. Gallovič (`https://github.com/fgallovic/fd3d_`

pt). Result of strong motion (< 1 Hz) inversion is the distribution of the dynamic parameters (prestress and friction law parameters). FD3D code, originally used as a forward solver for this inversion, was developed by [Madariaga et al., 1998], it is available at `http://www.geologie.ens.fr/~madariag/Programs/README_fd3d_xy.html`.

There were two issues with the original code – thin zone implementation of the fault boundary condition did not compare well with other approaches [Dalguer and Day, 2006] and the absorbing conditions at the border caused unwanted oscillation. Both problems can be minimized, but at the cost of an increase in the time of the calculation – the fault boundary model improves when finer grid is chosen, effect of the reflections from the absorbing boundary conditions can be minimized by a larger computational domain. This decreases the efficiency of the code, therefore significant improvements are required.

Chapter 1 of this thesis contains the formulation of the elastodynamic equation and the description of the finite difference staggered grid method. There were no additional improvements in this part of the code, with the exception of its OpenACC paralelization for GPU by L. Hanyk and F. Gallovic.

Chapter 2 deals with the fault boundary condition. It is formulated in Section 2.1. Two methods for its implementation – thin zone (Section 2.2) and traction at split node (Section 2.3) are described. Thin zone method [Madariaga et al., 1998] was originally used in the FD3D code. The traction at split node method [Andrews, 1973] was chosen as a replacement (Section 2.3), in the version for the staggered grid by Dalguer and Day [2007]. Incorporation of this method led to expected improvements in accuracy in kinematic parameters such as rupture time and slip.

The implementation of the new method revealed a large amount of energy reflecting from the absorbing boundary conditions (placed at the edges of the computational domain), causing continual sliding of the fault, driven by reflected waves. This was not the case for the original code due to additional artificial regularizations of the solution (instantaneous healing).

Update of the boundary conditions at the border was therefore also required. Implemented methods are described in Chapter 3. Small fixes in the free surface implementation (Section 3.1) were done, leading to slight improvements in the arrival time of the waves reflected from the surface. The major change was the implementation of Perfectly matched layers (Section 3.2) as the absorbing boundaries [Collino and Tsogka, 2001]. Although the calculation is significantly slower than for the original Clayton's conditions [Clayton and Engquist, 1977], the reflected waves were eliminated. Further reduction of the computational domain around the fault was allowed, compensating the increase in resource requirements.

The friction at the fault is a leading physical effect in the dynamic model. The slip-weakening friction law (Section 2.4) was used in dynamic simulations for decades and was also included in the original FD3D code. Empirical rate and state laws [Ruina, 1983] were offered as an alternative, describing much broader range of phenomena, from pulse-like beahviour of the rupture to seismic cycles. Their numerical implementation is more complicated, requiring solving additional differential equation at the fault boundary [Kaneko et al., 2008].

Modern high speed friction experiments [Di Toro et al., 2004, Goldsby and Tullis, 2011] offer an additional insight into the friction at earthquake sliding

speeds. The fast decrease of friction strength is observed, related to the flash heating of the fault surface [Rice, 2006]. The version of the rate and state friction law, based on these experiments, is described in the Section 2.5, and was also implemented, based on Rojas et al. [2009].

Updated version of the code, with a working name FD3D_TSN, was tested in community benchmark SCEC/USGS Spontaneous Rupture Code Verification Project [Harris et al., 2018]. Outcomes of these tests, including comparison with the original code, and with the more accurate (and more resource demanding) finite element code FaultMod [Barall, 2009]. Performance was tested for both friction laws. This represents the main part of the Thesis and is discussed in Chapter 4.

1. Wave propagation in the elastic medium

1.1 Elastodynamic equation and Hooke's law

The state of an elastic medium is described by two fields – displacement field u_i and stress field σ_{ij}. Indices i, j denote a component of a given vector or tensor and can have values of $1, 2$ and 3 for x, y and z components, respectively. Time development of both fields is governed by two equations – the elastodynamic equation

$$\rho \frac{\partial^2 u_i}{\partial t^2} = \sigma_{ij,j}, \tag{1.1}$$

and Hooke's law

$$\sigma_{ij} = c_{ijkl} u_{k,l}. \tag{1.2}$$

Einstein summation is assumed, unless stated otherwise. Spatially variable parameters ρ (density) and c_{ijkl} (tensor of elastic moduli) describe material properties. Only isotropic material will be presumed in this work, therefore

$$c_{ijkl} = \lambda \delta_{ij} \delta_{kl} + \mu(\delta_{ik}\delta_{jl} + \delta_{il}\delta_{jk}), \tag{1.3}$$

where λ and μ are Lame's parameters.

Using the combination of equations (1.1) and (1.2) for the description of the wave propagation is called displacement-stress formulation. Extensively used alternative is the velocity-stress formulation [Moczo et al., 2007], which leads to a more symmetric set of equations and will be used throughout this work. Velocity v_i is substituted into the elastodynamic equation as the time derivative of the displacement:

$$\rho \frac{\partial v_i}{\partial t} = \sigma_{ij,j}, \tag{1.4}$$

and Hooke's law is differentiated with respect to time:

$$\frac{\partial \sigma_{ij}}{\partial t} = c_{ijkl} v_{k,l}. \tag{1.5}$$

In the frequency domain, this set of equations has the following form:

$$\rho \iota \omega \hat{v}_i = \hat{\sigma}_{ij,j} \tag{1.6}$$

$$\iota \omega \hat{\sigma}_{ij} = c_{ijkl} \hat{v}_{k,l}, \tag{1.7}$$

where $\hat{v}_i$ and $\hat{\sigma}_{ij}$ are velocity and stress as a function of angular frequency ω and ι an imaginary unit.

One of the analytical solutions of the elastodynamic equation can be found in the form of a plane wave

$$v_j = V_j \exp\left[-\iota(k_1 x_1 + k_2 x_2 + k_3 x_3 - \omega t)\right], \tag{1.8}$$

where V_j represents the amplitude of the j-th component of the plane wave solution, $\mathbf{k} = (k_1, k_2, k_3)$ is a wave vector.

1.2 Grid and finite differences

All calculations will be performed using a three dimensional Cartesian coordinate system (x, y, z) with forth dimension being time t. The space is discretized into a grid of discrete points numbered by four indexes (I, J, K, N). Position of a point is given by four values – (x_I, y_J, z_K, t_N). Only regular grids will be considered, which means that for each I, J, K, N applies:

$$x_I - x_{I-1} = \Delta h \tag{1.9}$$
$$y_J - y_{J-1} = \Delta h \tag{1.10}$$
$$z_K - z_{K-1} = \Delta h \tag{1.11}$$
$$t_N - t_{N-1} = \Delta t, \tag{1.12}$$

where Δh is a spatial and Δt temporal grid spacing. The position of the node will be given by four numbers I, J, K, N, that can have half integer values $0, 1/2, 1, ...$ Fields v_i and σ_{ij} are approximated by their values at these discrete nodes. They can be calculated all at same point (unstaggered grid) or at different points mutually shifted (staggered grid). Partly staggered grids, where all velocity components are at one point and all stress components at another were also used, especially when attenuation came into consideration.

Mutual positions of the components in the staggered grid is shown in Fig 1.1. These positions are chosen with respect to the discretization of the spatial derivatives in the elastodynamic equation and the Hooke's law.

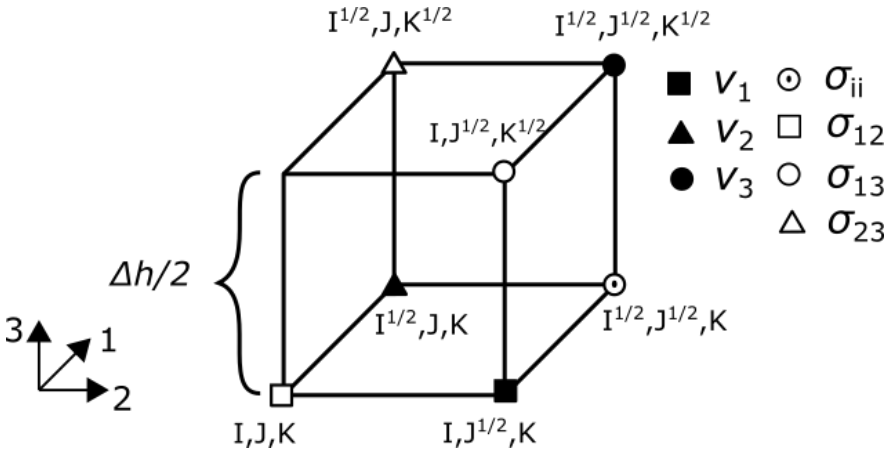

Figure 1.1: Staggered grid cell positioned around the node I, J, K considered in this Thesis. Symbols (triangles, squares, circles) label the positions of spatialy staggered velocity and stress components.

The position of the velocity and stress components is staggered in time also. All velocity components are calculated at $N\Delta t$ time levels, for $N = 0, 1, ..., T/\Delta t$, where T is the maximum simulation time. The stress components are positioned at the time levels shifted by a factor of $\Delta t/2$ as can be seen in Fig 1.2.

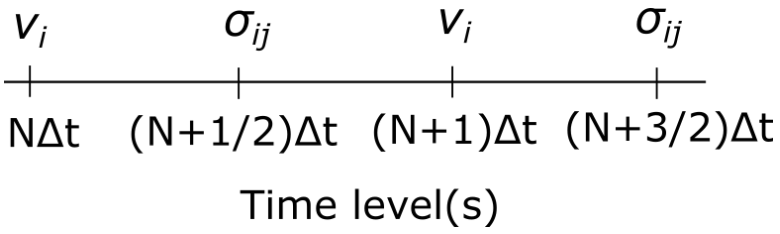

Figure 1.2: Time staggered position of the velocity and stress components.

Solving the set of partial differential equations (1.4) and (1.5) by the finite difference (FD) method requires approximation of the time and spatial derivatives by respective FD formulas. FD formulas of the second order read:

$$(D_1^{(2)}\phi)_{I,J,K} = \left[\phi_{I^{\frac{1}{2}},J,K} - \phi_{I^{-\frac{1}{2}},J,K}\right]/\Delta h \tag{1.13}$$

$$(D_2^{(2)}\phi)_{I,J,K} = \left[\phi_{I,J^{\frac{1}{2}},K} - \phi_{I,J^{-\frac{1}{2}},K}\right]/\Delta h \tag{1.14}$$

$$(D_3^{(2)}\phi)_{I,J,K} = \left[\phi_{I,J,K^{\frac{1}{2}}} - \phi_{I,J,K^{-\frac{1}{2}}}\right]/\Delta h. \tag{1.15}$$

And FD formulas of the forth order read:

$$(D_1^{(4)}\phi)_{I,J,K} = \left[\frac{9}{8}(\phi_{I^{\frac{1}{2}},J,K} - \phi_{I^{-\frac{1}{2}},J,K}) - \frac{1}{24}(\phi_{I^{\frac{3}{2}},J,K} - \phi_{I^{-\frac{3}{2}},J,K})\right]/\Delta h \tag{1.16}$$

$$(D_2^{(4)}\phi)_{I,J,K} = \left[\frac{9}{8}(\phi_{I,J^{\frac{1}{2}},K} - \phi_{I,J^{-\frac{1}{2}},K}) - \frac{1}{24}(\phi_{I,J^{\frac{3}{2}},K} - \phi_{I,J^{-\frac{3}{2}},K})\right]/\Delta h \tag{1.17}$$

$$(D_3^{(4)}\phi)_{I,J,K} = \left[\frac{9}{8}(\phi_{I,J,K^{\frac{1}{2}}} - \phi_{I,J,K^{-\frac{1}{2}}}) - \frac{1}{24}(\phi_{I,J,K^{\frac{3}{2}}} - \phi_{I,J,K^{-\frac{3}{2}}})\right]/\Delta h, \tag{1.18}$$

where ϕ denotes any components of velocity or stress. For convinience we use I^J instead of $I + J$ to express complicated indexes designating position in the FD grid. The direction of the difference is set by a lower index (1 for x, etc.).

The position in time will be marked by an upper index, where index N marks the time level $N\Delta t$. The time difference $D_t\phi$ at the time level $(N + \frac{1}{2})\Delta t$ will be defined as a difference between values of ϕ at time levels shifted by $\Delta t/2$ in both directions:

$$(D_t\phi)_{I,J,K}^{N^{\frac{1}{2}}} = \left[\phi_{I,J,K}^{N} - \phi_{I,J,K}^{N^{-1}}\right]/\Delta t. \tag{1.19}$$

This central finite difference formula is of the second order.

Using (1.16,1.17,1.18) and (1.19) to approximate the spatial and time derivatives in (1.4) and (1.5) leads to an updating scheme that allows for calculation of $\sigma_{ij}^{N^{\frac{1}{2}}}$ and v_i^{N+1} from $\sigma_{ij}^{N^{-\frac{1}{2}}}$ and v_i^N. As a starting point, the initial conditions $\sigma_{ij}^{\frac{1}{2}}$ and v_i^0 for velocity and stress, respectively, are required .

The scheme using the 2-nd order spatial formulas was introduced by [Virieux, 1986] and using the 4-th order formulas by [Levander, 1988], in both cases only for calculation of P-SV seismograms, not the whole elastodynamic equation. The

full staggered FD 4-th order scheme used in this work was introduced by [Graves, 1996]. It consists of nine FD formulas:

$$(v_1)^{N^1}_{I,J^{\frac{1}{2}},K} = (v_1)^{N}_{I,J^{\frac{1}{2}},K} + \frac{\Delta t}{\rho}\left([D_1^{(4)}\sigma_{11}]_{I,J^{\frac{1}{2}},K} + [D_2^{(4)}\sigma_{12}]_{I,J^{\frac{1}{2}},K} + [D_3^{(4)}\sigma_{13}]_{I,J^{\frac{1}{2}},K}\right) \tag{1.20}$$

$$(v_2)^{N^1}_{I^{\frac{1}{2}},J,K} = (v_2)^{N}_{I^{\frac{1}{2}},J,K} + \frac{\Delta t}{\rho}\left([D_1^{(4)}\sigma_{12}]_{I^{\frac{1}{2}},J,K} + [D_2^{(4)}\sigma_{22}]_{I^{\frac{1}{2}},J,K} + [D_3^{(4)}\sigma_{23}]_{I^{\frac{1}{2}},J,K}\right) \tag{1.21}$$

$$(v_3)^{N^1}_{I^{\frac{1}{2}},J^{\frac{1}{2}},K^{\frac{1}{2}}} = (v_3)^{N}_{I^{\frac{1}{2}},J^{\frac{1}{2}},K^{\frac{1}{2}}} + \frac{\Delta t}{\rho}\left([D_1^{(4)}\sigma_{13}]_{I^{\frac{1}{2}},J^{\frac{1}{2}},K^{\frac{1}{2}}} + [D_2^{(4)}\sigma_{23}]_{I^{\frac{1}{2}},J^{\frac{1}{2}},K^{\frac{1}{2}}} + [D_3^{(4)}\sigma_{33}]_{I^{\frac{1}{2}},J^{\frac{1}{2}},K^{\frac{1}{2}}}\right) \tag{1.22}$$

$$(\sigma_{11})^{N^{\frac{1}{2}}}_{I^{\frac{1}{2}},J^{\frac{1}{2}},K} = (\sigma_{11})^{N^{-\frac{1}{2}}}_{I^{\frac{1}{2}},J^{\frac{1}{2}},K} + \Delta t\left((\lambda+2\mu)[D_1^{(4)}v_1]_{I^{\frac{1}{2}},J^{\frac{1}{2}},K} + \lambda[D_2^{(4)}v_2]_{I^{\frac{1}{2}},J^{\frac{1}{2}},K} + \lambda[D_3^{(4)}v_3]_{I^{\frac{1}{2}},J^{\frac{1}{2}},K}\right) \tag{1.23}$$

$$(\sigma_{22})^{N^{\frac{1}{2}}}_{I^{\frac{1}{2}},J^{\frac{1}{2}},K} = (\sigma_{22})^{N^{-\frac{1}{2}}}_{I^{\frac{1}{2}},J^{\frac{1}{2}},K} + \Delta t\left(\lambda[D_1^{(4)}v_1]_{I^{\frac{1}{2}},J^{\frac{1}{2}},K} + (\lambda+2\mu)[D_2^{(4)}v_2]_{I^{\frac{1}{2}},J^{\frac{1}{2}},K} + \lambda[D_3^{(4)}v_3]_{I^{\frac{1}{2}},J^{\frac{1}{2}},K}\right) \tag{1.24}$$

$$(\sigma_{33})^{N^{\frac{1}{2}}}_{I^{\frac{1}{2}},J^{\frac{1}{2}},K} = (\sigma_{33})^{N^{-\frac{1}{2}}}_{I^{\frac{1}{2}},J^{\frac{1}{2}},K} + \Delta t\left(\lambda[D_1^{(4)}v_1]_{I^{\frac{1}{2}},J^{\frac{1}{2}},K} + \lambda[D_2^{(4)}v_2]_{I^{\frac{1}{2}},J^{\frac{1}{2}},K} + (\lambda+2\mu)[D_3^{(4)}v_3]_{I^{\frac{1}{2}},J^{\frac{1}{2}},K}\right) \tag{1.25}$$

$$(\sigma_{12})^{N^{\frac{1}{2}}}_{I,J,K} = (\sigma_{12})^{N^{-\frac{1}{2}}}_{I,J,K} + \mu\Delta t\left([D_2^{(4)}v_1]_{I,J,K} + [D_1^{(4)}v_2]_{I,J,K}\right) \tag{1.26}$$

$$(\sigma_{13})^{N^{\frac{1}{2}}}_{I,J^{\frac{1}{2}},K^{\frac{1}{2}}} = (\sigma_{13})^{N^{-\frac{1}{2}}}_{I,J^{\frac{1}{2}},K^{\frac{1}{2}}} + \mu\Delta t\left([D_3^{(4)}v_1]_{I,J^{\frac{1}{2}},K^{\frac{1}{2}}} + [D_1^{(4)}v_3]_{I,J^{\frac{1}{2}},K^{\frac{1}{2}}}\right) \tag{1.27}$$

$$(\sigma_{23})^{N^{\frac{1}{2}}}_{I^{\frac{1}{2}},J,K^{\frac{1}{2}}} = (\sigma_{23})^{N^{-\frac{1}{2}}}_{I^{\frac{1}{2}},J,K^{\frac{1}{2}}} + \mu\Delta t\left([D_3^{(4)}v_2]_{I^{\frac{1}{2}},J,K^{\frac{1}{2}}} + [D_2^{(4)}v_3]_{I^{\frac{1}{2}},J,K^{\frac{1}{2}}}\right). \tag{1.28}$$

They are derived by the discretization of the elatodynamic equation (1.4) for velocities (1.20 to 1.22), and Hooke's law (1.5) for stress (1.23 to 1.28), for the case of the isotropic material rheology. Formulas are for all velocity and stress components at the nodes in one grid cell, positioned at I, J, K. The material parameters are considered constant through the cell. Fig (1.1) shows mutual positions of the components in the grid cell.

For the FD scheme to be stable, its plane wave solution (1.8) cannot grow when the propagation of the wave is calculated using the scheme [Moczo et al., 2007]. The ansatz of the solution into the concrete FD scheme (this approach is called the Neumann's method) leads to a CFL condition (Courant-Friedrichs-Levy) for discretization steps Δt and Δh. In particular, for the time step we obtain [Moczo et al., 2000]

$$\Delta t < C_{CFL} \Delta h, \tag{1.29}$$

where C_{CFL} is a parameter depending on the particular FD scheme and the wave velocity in a media. The value

$$C^{\alpha}_{CFL} = \frac{6}{v_{alpha} 7\sqrt{3}}, C^{\beta}_{CFL} = \frac{6}{v_{\beta} 7\sqrt{3}} \tag{1.30}$$

was derived by Moczo et al. [2000] for the 4th order staggered grid FD scheme. Velocities of the P and S wave are denoted as v_{α} and v_{β}, respectively. The stability condition (1.29) is more restrictive for the P waves. The time discretization parameter for simulations in heterogenous medium is set to guarantee the stability of the P wave solution in the area with the highest P wave velocity.

The second concept coming from the Neumann's analysis is the grid dispersion. It offers a way to set Δh to obtain a desired accuracy. The grid dispersion is the ratio between the grid wave velocity (v^g_{α} or v^g_{β}) at which the wave propagates when FD method is applied and the true wave velocity (v_{α} or v_{β}). Grid dispersion depends on spatial sampling ratio $\Delta h/\lambda$, where $\lambda = 2\pi v_{\alpha}(v_{\beta})/\omega$ is the wave length of the P(S) wave. The grid dispersion decreases (the discrete wave solution is slowing down) as the spatial sampling ratio increases (less points per wave length). Moczo et al. [2000] recommends setting Δh to have at least 6 grid nodes per wavelength of the S wave at maximum desired frequency. This should bound the error in its velocity by 5 percent.

There are three important concepts in numerical mathematics that need to be taken into account when using dicrete PDE methods – consistency, stability and convergence. The FD method is consistent, when its discrete formulas equal the partial differential equations when limiting $\Delta h, \Delta t \to 0$. This is typically the case and it is easy to check.

The FD method is convergent if the discrete solution converges towards the actual solution of the PDE when limiting $\Delta h, \Delta t \to 0$. It is the desired property of FD methods but it is difficult to check, especially when boundary conditions are taken into account.

The FD method is stable, when the discrete solution is bounded, while the actual solution is also bounded. It can be proven, that the FD method is convergent when it is consistent and stable, therefore testing the stability instead of the convergence is possible. Neumann's method (mentioned above) is a typical method to test boundedness of a solution, although just for the specific shape of the plane wave.

2. Dynamic fault model in finite differences

The mathematical description of an approximate earthquake model and its introduction into the FD wave simulation code as a boundary condition are described in this chapter. While earthquake source is a complex set of mechanical (gouge, damage, lubrication), termal (termal pressurization, melting) and chemical phenomena, theoretical dynamic earthquake models are much simpler. The popular approximation described here (Section 2.1) sets the earthquake as a shear rupture on a frictional (planar) interface between elastic halfspaces. Higher order effects can be added into this model through more complicated friction law, changes to rheology of the off-fault material, or more complicated geometry of the interface.

We consider two types of friction laws in this Thesis – slip weakening law (Section 2.4) and rate-and-state law. The fact that force required to start the sliding is higher then the force required for its continuation is a major idea behind the slip weakening law. Empirical rate and state (Section 2.5) law considers much wider range of experiments, with sliding velocity chaging during the experiment [Dieterich, 1979, Ruina, 1983]. Newer version of this law with fast velocity weakening is considered, based on friction experiments performed at seismic speeds of the order of 1 m/s [Goldsby and Tullis, 2011].

When using staggered/partially staggered grids, components of velocity and stress are not calculated at the same node. Some components will be calculated outside of the fault plane. Historically, there were essentially two groups of methods considered for the introduction of fault boundary into finite differences – inelastic zone methods and split node methods [Moczo et al., 2007].

The first group comprises methods that establish fault as a zone of finite width that surrounds the grid nodes, where velocity and traction is calculated. Their values inside this zone are then considered the same through the zone. Popular methods in this group are thick or thin zone methods (Section 2.2) developed by R. Madariaga.

Splitting the space by the fault into two halves, which are interacting only through chosen nodes at the fault surface is a staple of split node methods. Traction at split node method is described in Section 2.3.

2.1 Fault as a boundary condition

Fault plane divides space into two halfspaces, denoted as '+' and '-' as in Fig 2.1. We define slip s_i as a discontinuity in displacement vector u_i across the fault

$$s_i(\mathbf{x}, t) = u_i^+(\mathbf{x}, t) - u_i^-(\mathbf{x}, t), \tag{2.1}$$

and slip rate as a discontinuity in velocity

$$\dot{s}_i(\mathbf{x}, t) = v_i^+(\mathbf{x}, t) - v_i^-(\mathbf{x}, t), , \tag{2.2}$$

with absoulte values denoted as s and $\dot{s}$, respectively.

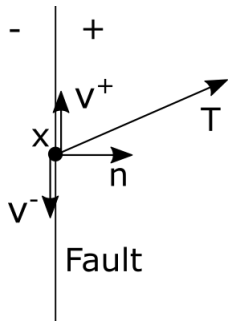

Figure 2.1: Scheme of the fault variables at point $\mathbf{x}$ – normal to the fault n_i, discontinous velicity $v_i^+$and $v_i^-$and continous traction T_i.

Let n_i be a unit normal vector to the fault, that points into '+' halfspace and $T_i(\mathbf{x}, \mathbf{n}, t) = \sigma_{ij} n_j$ is a traction on the fault. Since shear faulting is expected, continuity of normal componets of displacement u_i^n and velocity v_i^n is in place:

$$0 = u_i^{n+}(\mathbf{x}, t) - u_i^{n-}(\mathbf{x}, t), \tag{2.3}$$

$$0 = v_i^{n+}(\mathbf{x}, t) - v_i^{n-}(\mathbf{x}, t). \tag{2.4}$$

Traction $T_i(\mathbf{x}, \mathbf{n}, t)$ is continuus through the fault. Let $S(\mathbf{x}, t)$ be a value of frictional strength. Value of shear traction $T^s(\mathbf{x}, \mathbf{n}, t)$ at the fault is bounded by frictional strength

$$T^s(\mathbf{x}, t) \leq S(\mathbf{x}, t). \tag{2.5}$$

Second condition on traction requires it to act opposite to velocity discontinuity.

$$T_i^s(\mathbf{x}, t)\dot{s}(\mathbf{x}, t) - S(\mathbf{x}, t)\dot{s}_i(\mathbf{x}, t) = 0 \tag{2.6}$$

The magnitude of traction in this slipping case is set to be equal to frictional strength by condition (2.5). In both following sections trial shear traction T_i^T is calculated, that equals the values of traction if slip doesn't occur (frictional strength S higher then T^T). For the case of vertical fault, it has only two non-zero components T_1^T and T_3^T.

Introduction of the non-planar (or even just dipping planar) fault boundary condition into the regular grid is very complicated. Only Cruz-Atienza et al. [2007] managed to do a stable non-planar model for the case of the partially staggered grid. Irregular grids seem to be the most popular way to intoduce the non-planar faults, such as in Duru and Dunham [2016], but these are out of the scope of this work.

Only vertical planar fault will be assumed in this work and all derivations will be done for the fault plane being a $1-3$ plane. The following symmetries and antisymmetries in stress and velocity components along the fault in $1-3$ plane are in place (expecting the same material parameters on both sides of the fault plane):

$$v_1^+ = -v_1^- \qquad v_2^+ = +v_2^- \qquad v_3^+ = -v_3^- \tag{2.7}$$

$$\sigma_{11}^+ = -\sigma_{11}^- \qquad \sigma_{22}^+ = \sigma_{22}^- \qquad \sigma_{33}^+ = -\sigma_{33}^- \tag{2.8}$$

$$\sigma_{12}^+ = +\sigma_{12}^- \qquad \sigma_{13}^+ = -\sigma_{13}^- \qquad \sigma_{23}^+ = +\sigma_{23}^- \tag{2.9}$$

2.2 Thick and thin zone methods

Formulation of the thick zone method of representation of the fault boundary condition was introduced by Madariaga et al. [1998]. Thin zone method is its improved version, whose accuracy should be better [Madariaga, at `http://www.geologie.ens.fr/~madariag/`].

In both cases, the fault plane is chosen to coincide with one of the $1-3$ planes in the staggered grid. The position of the plane along axis 2 is denoted as J_F, which means that for all nodes at the plane $J = J_F$ applies. The fault boundary condition (2.5, 2.6) is then applied, using appropriate velocity and stress components for traction and slip rate. These components are not all positioned in FD nodes at the fault plane, the value of the component at the closest node is taken instead. The position of fault plane in the FD grid for thick and thin zone method is shown in Fig 2.2.

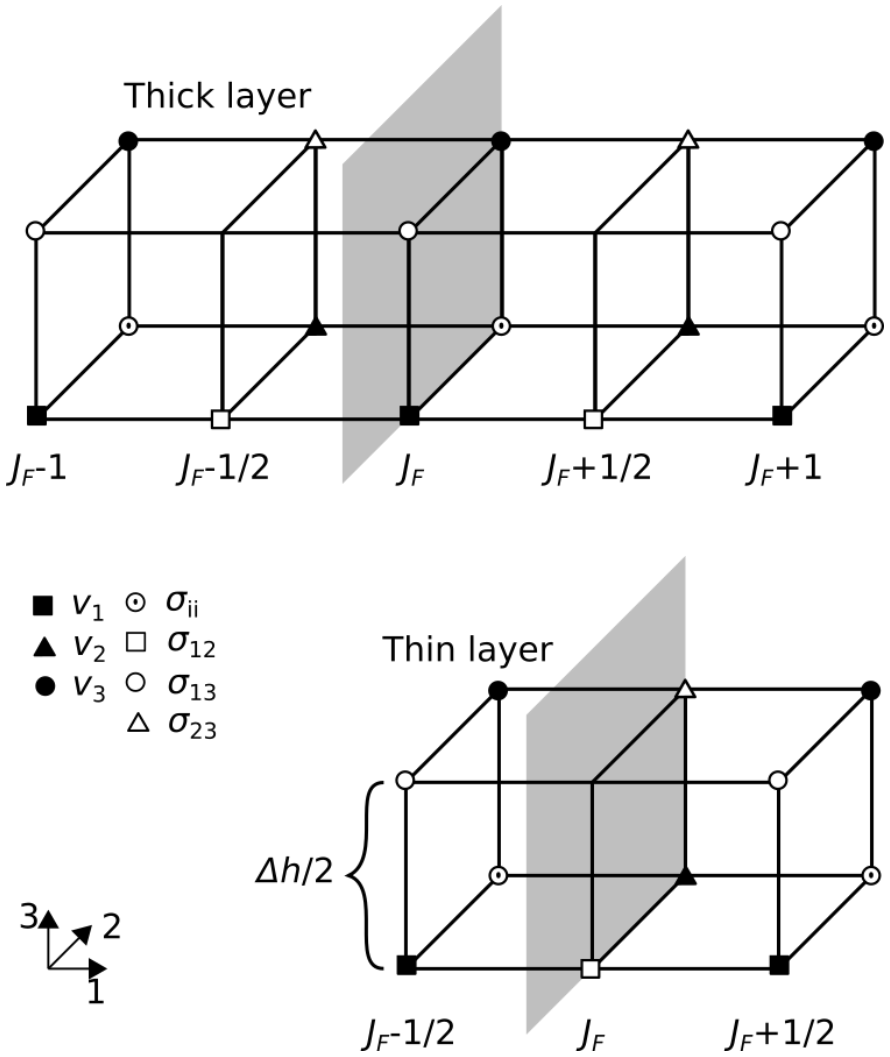

Figure 2.2: Thick and thin layer position in FD staggered grid. The fault plane is denoted by a grey plane at position $J = J_F$.

In the thick zone method, the fault plane is set to cut through the finite difference grid in shear velocity nodes (v_1, v_3). Enforcement of the fault boundary condition using this method requires shear traction components that are cal-

culated at the nodes at the grid plane shifted by $\Delta h/2$ (stress plane) and shear velocity components at the velocity plane shifted by Δh. Size of the zone containing all components, required for fault boundary condition is $2\Delta h$. Assumption, that the traction is the same at the border of the thick zone and in the middle of it, means that inelasticity at the zone around the fault is prescribed. This is only a mathematical approximation, and has no connection to any physical effect in real eartquakes.

First, trial shear traction components are calculated by the FD formula from Hooke's law

$$(T_1^T)^{N^{\frac{1}{2}}}_{I,J_F^{\frac{1}{2}},K} = (\sigma_{12})^{N^{\frac{1}{2}}}_{I,J_F^{\frac{1}{2}},K} = (\mu)\frac{\Delta t}{\Delta h}\Big((D_2^{(4)}v_1)^{N}_{I,J_F^{\frac{1}{2}},K} + (D_1^{(4)}v_2)^{N}_{I,J_F^{\frac{1}{2}},K}\Big) \tag{2.10}$$

$$(T_3^T)^{N^{\frac{1}{2}}}_{I^{\frac{1}{2}},J_F^{\frac{1}{2}},K^{\frac{1}{2}}} = (\sigma_{23})^{N^{\frac{1}{2}}}_{I^{\frac{1}{2}},J_F^{\frac{1}{2}},K^{\frac{1}{2}}} = \mu\frac{\Delta t}{\Delta h}\Big((D_3^{(4)}v_2)^{N}_{I^{\frac{1}{2}},J_F^{\frac{1}{2}},K^{\frac{1}{2}}} + (D_2^{(4)}v_3)^{N}_{I^{\frac{1}{2}},J_F^{\frac{1}{2}},K^{\frac{1}{2}}}\Big), \tag{2.11}$$

with traction on the other plane being equal due to the symmetry:

$$(T_1^T)^{N^{\frac{1}{2}}}_{I,J_F^{-\frac{1}{2}},K} = (T_1^T)^{N^{\frac{1}{2}}}_{I,J_F^{\frac{1}{2}},K} \tag{2.12}$$

$$(T_3^T)^{N^{\frac{1}{2}}}_{I^{\frac{1}{2}},J_F^{-\frac{1}{2}},K^{\frac{1}{2}}} = (T_3^T)^{N^{\frac{1}{2}}}_{I^{\frac{1}{2}},J_F^{\frac{1}{2}},K^{\frac{1}{2}}} \tag{2.13}$$

To acquire absolute value of trial traction at both nodes, missing component needs to be interpolated, for example T_1^T at nodes $(I^{\frac{1}{2}}, J_F^{\frac{1}{2}}, K^{\frac{1}{2}})$ and $(I^{\frac{1}{2}}, J_F^{-\frac{1}{2}}, K^{\frac{1}{2}})$. Alternative approach is to add an extra simplification, by allowing slip only in direction of axis 1 (strike slip) or 3 (dip slip) . The value of one component T_1^T or T_3^T can then be considered instead of the absolute value of the whole trial shear traction $(T^T)^{N^{\frac{1}{2}}}$. The fault conditions (2.5) and (2.6) are then applied to this trial shear traction. The value of the traction is modified to be equal to the friction at all nodes, where it would be larger then friction:

$$(T_i)^{N^{\frac{1}{2}}} = \begin{cases} (T_i^T)^{N^{\frac{1}{2}}}, & \text{if } (T^T)^{N^{\frac{1}{2}}} \le S^{N^{\frac{1}{2}}} \\ S^{N^{\frac{1}{2}}}\frac{(T_i^T)^{N^{\frac{1}{2}}}}{(T^T)^{N^{\frac{1}{2}}}}, & \text{if } (T^T)^{N^{\frac{1}{2}}} > S^{N^{\frac{1}{2}}}, \qquad i = 1, 3. \end{cases} \tag{2.14}$$

Velocity coponents v_1 and v_3 in planes (J_F-1) and (J_F+1) are then calculated already with the modified traction. Slip rate components are defined as

$$(\dot{s}_1)^{N^1}_{I,J_F,K} = (v_1)^{N^1}_{I,J_F^1,K} - (v_1)^{N^1}_{I,J_F^{-1},K} \tag{2.15}$$

$$(\dot{s}_3)^{N^1}_{I^{\frac{1}{2}},J_F,K^{\frac{1}{2}}} = (v_3)^{N^1}_{I^{\frac{1}{2}},J_F^1,K^{\frac{1}{2}}} - (v_3)^{N^1}_{I^{\frac{1}{2}},J_F^{-1},K^{\frac{1}{2}}}. \tag{2.16}$$

On the contrary, thin layer method requires only shear traction components directly at the fault plane and shear velocity components at the velocity plane shifted by $\Delta h/2$. Thin zone thickness is Δh.

Improved thin zone method is acquired by several changes. Fault plane cuts the grid in a stress plane and $T_1 = \sigma_{12}$ and $T_3 = \sigma_{23}$ on this plane are taken as trial traction components. Two velocity planes $(J_F - 1/2)$ and $(J_F + 1/2)$

directly next to the fault plane contain the shear velocity components for the calculation of the slip rate and together they create an inelastic zone of thickness Δh. The whole procedure is then very similar as in the case of the thick zone – the trial traction is calculated, the fault condition is applied, modifying the value of traction, followed by the calculation of the velocity and the slip rate.

2.3 Traction at split node method

In this section, the traction at split node implementation of the fault boundary condition is introduced independently of a chosen FD grid – the values are expected to be all in a single node. The concrete application, using specific staggered grid scheme, is then desribed in the second half of this section.

It was developed independently by Andrews [1973] and Day [1977] and used in combination with partially staggered grid FD method in the first case and finite element method in the second case. Description of its use with staggered grid was given by Dalguer and Day [2007], which is followed closely in the second half of this section.

The fault plane cuts through the domain, dividing it into two half spaces '+' and '-'. Every node on the fault plane belongs to both halfspaces + and −. To obtain the complete partition into the two halfspaces, these nodes are cut into two split nodes, with their distinct masses, velocities, stresses and material properties. The only quantity they share is traction T_i. The mass of the split node is calculated as $M^{\pm} = \Delta h^3 \rho^{\pm}/2$ in the case of fault cutting the split node (and its FD 'cube' with side equal to Δh) in half (Fig 2.3).

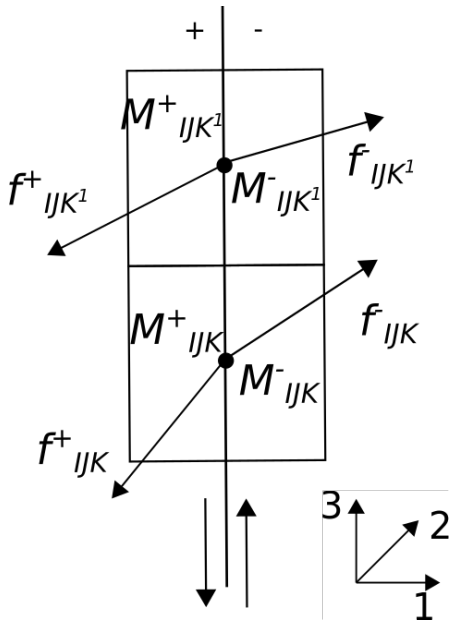

Figure 2.3: Illustration of the split node. Both FD grid nodes at positions given by indexes IJK and IJK^1 are split into two halves denoted as + and −. Halfspace acts upon a split node of mass M with a force f.

In both halfspaces, the elastodynamic force acts upon the split nodes and is

equal to the right hand side of the elastodynamic equation (1.4):

$$f_i^{\pm} = \frac{1}{\rho^{\pm}} \sigma_{ij,j}. \tag{2.17}$$

The formula (2.17) represents the body force of the halfspace, without the surface (fault) force – for the calculation of this force, the fault is considered to be a free surface.

Split nodes are coupled through the traction T_i that generates the surface force f_i^c. This force is of the same magnitude for both split nodes, but of different orientation. For $-$ side it yields:

$$f_i^c = \Delta h^2 (T_i - T_i^0), \tag{2.18}$$

where T_i^0 is a traction at the initial state of equilibrium.

The acceleration in split nodes can be written from the 2nd Newton's law:

$$\frac{\partial v_i^{\pm}}{\partial t} = (f_i^{\pm} \mp f_i^c)/M^{\pm}. \tag{2.19}$$

It is introduced into the FD formulas as the right hand side of the updating scheme for the velocity components at the fault plane:

$$(v_i^{\pm})^{N^1} = (v_i^{\pm})^N + \Delta t \left[(f_i^{\pm})^{N^{\frac{1}{2}}} \mp \Delta h^2 \left((T_i)^{N^{\frac{1}{2}}} - T_i^0 \right) \right] / M^{\pm}, \tag{2.20}$$

Slip rate is calculated from (2.2), as a difference between the velocity values in both split nodes:

$$(\dot{s}_i)^{N^1} = (\dot{s}_i)^N + \Delta t \left[\frac{(f_i^+)^{N^{\frac{1}{2}}}}{M^+} - \frac{(f_i^-)^{N^{\frac{1}{2}}}}{M^-} + \frac{(T_i)^{N^{\frac{1}{2}}} - T_i^0}{\Delta h^{-2} M^-} - \frac{(T_i)^{N^{\frac{1}{2}}} - T_i^0}{\Delta h^{-2} M^+} \right], \tag{2.21}$$

which can be rearanged to:

$$(\dot{s}_i)^{N^1} = (\dot{s}_i)^N + \frac{\Delta t \, (M^- + M^+)}{\Delta h^{-2} M^- M^+} \left[\frac{M^- (f_i^+)^{N^{\frac{1}{2}}} - M^+ (f_i^-)^{N^{\frac{1}{2}}}}{\Delta h^2 (M^- + M^+)} + (T_i)^{N^{\frac{1}{2}}} - T^0 \right]. \tag{2.22}$$

Next we can distinguish between two cases: with zero and with non zero slip rate $(\dot{s}_i)^{N^1}$. The traction in the former case is a trial traction and again denoted as T_i^T. We can simply express it from equation (2.22) considering $(\dot{s}_i)^{N^1} = 0$:

$$(T_i^T)^{N^{\frac{1}{2}}} = T_i^0 + \frac{\Delta t^{-1} M^- M^+ (\dot{s}_i)^N + M^- (f_i^+)^{N^{\frac{1}{2}}} - M^+ (f_i^-)^{N^{\frac{1}{2}}}}{\Delta h^2 (M^- + M^+)}. \tag{2.23}$$

This result is working even for faults that are neither vertical nor planar. From here, we will again continue with only vertical planar faults in the 13 plane. It means, that calculated trial traction has a normal component $(T_2^T)^{N^{\frac{1}{2}}}$ and two shear components $(T_1^T)^{N^{\frac{1}{2}}}$ and $(T_3^T)^{N^{\frac{1}{2}}}$.

When the value of trial shear traction $(T_i^T)^{N^{\frac{1}{2}}}$ is higher then frictional force $S^{N^{\frac{1}{2}}}$, faulting occurs and $(\dot{s})^{n^1} \neq 0$. Conditions (2.3) and (2.4) need to be enforced. What is the difference between the trial traction and the traction in the

case when the fault is slipping? It can be acquired by substracting (2.22) in the first case ($\dot{s}^{N^1} = 0, (T_i)^{N^{\frac{1}{2}}} = (T_i^T)^{N^{\frac{1}{2}}}$) from the same equation in the second case ($\dot{s}^{N^1} \neq 0$), which leads to

$$(\dot{s}_i)^{N^1} = \Delta t \frac{\Delta h^2 (M^- + M^+)}{M^- M^+} \left((T_i)^{N^{\frac{1}{2}}} - (T_i^T)^{N^{\frac{1}{2}}} \right). \tag{2.24}$$

The time dicretization of the used formulas led to the traction being calculated at time $(N+\frac{1}{2})\Delta t$, while the slip rate is acquired at the time $(N+1)\Delta t$. However, these quantities are both needed in the colinearity condition (2.6). Evaluation of both quantities at one time requires interpolation, which can cause unwanted oscillations. Values at different times are therefore used:

$$(T_i)^{N^{\frac{1}{2}}} \dot{s}^{N^1} - S^{N^{\frac{1}{2}}} (\dot{s}_i)^{N^1} = 0, \tag{2.25}$$

and inserting (2.24) substituted for $(\dot{s}_i)^{N^1}$ in 2.25 yields:

$$\left(S^{N^{\frac{1}{2}}} + (\Delta T)^{N^{\frac{1}{2}}} \right) (T_i)^{N^{\frac{1}{2}}} = S^{N^{\frac{1}{2}}} (T_i^T)^{N^{\frac{1}{2}}}. \tag{2.26}$$

Here $(\Delta T)^{N^{\frac{1}{2}}}$ is the absolute value of the difference between the shear traction and the shear trial traction. This formula ties value of $(T_i)^{N^{\frac{1}{2}}}$ with frictional force $S^{N^{\frac{1}{2}}}$. Solution to equation (2.26),

$$(T_i)^{N^{\frac{1}{2}}} = S^{N^{\frac{1}{2}}} \frac{(T_i^T)^{N^{\frac{1}{2}}}}{(T^T)^{N^{\frac{1}{2}}}}, \tag{2.27}$$

also fulfills the condition (2.3).

The final formula for shear traction is:

$$(T_i)^{N^{\frac{1}{2}}} = \begin{cases} (T_i^T)^{N^{\frac{1}{2}}}, & \text{if } (T^T)^{N^{\frac{1}{2}}} \leq S^{N^{\frac{1}{2}}} \\ S^{N^{\frac{1}{2}}} \frac{(T_i^T)^{N^{\frac{1}{2}}}}{(T^T)^{N^{\frac{1}{2}}}}, & \text{if } (T^T)^{N^{\frac{1}{2}}} > S^{N^{\frac{1}{2}}}, \end{cases} \qquad i = 1, 3. \tag{2.28}$$

Normal value of traction is not changing. This formula is formaly the same as in the case of the thick/thin layer methods (2.14). The major difference is that the trial traction is calculated in the same node as the slip rate. Traction at split node approach was typically utilized in combination with finite differences with partly staggered grid, whose advantage is the calculation of all components of stress or velocity at one point. Use of the staggered grid leads to certain complications, caused by the staggered position of the individual stress and velocity components [Dalguer and Day, 2007].

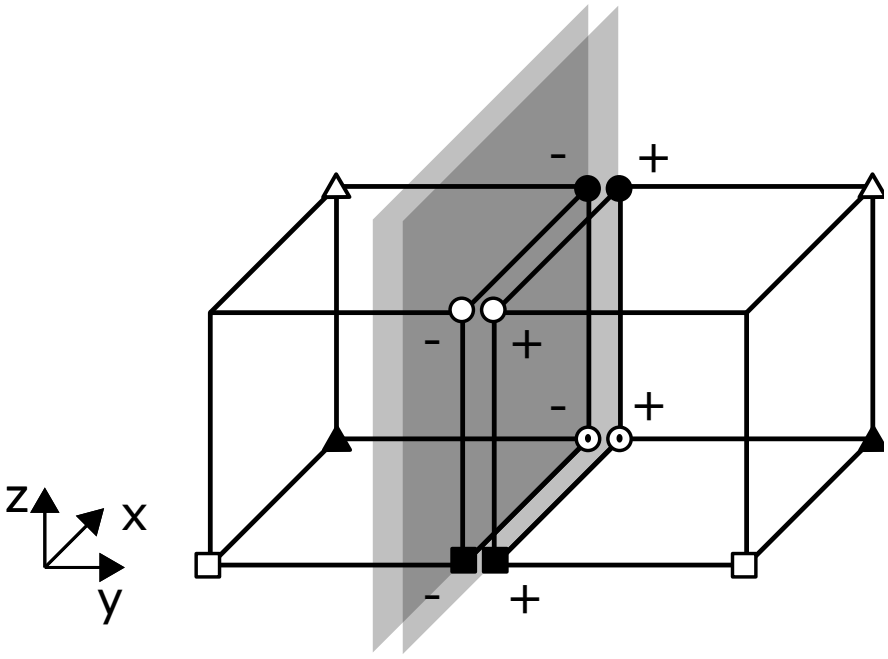

Figure 2.4: Fault plane dividing the FD staggered grid, when traction at split node method is applied. Discontinuus components calculated directly at the fault plane have their + and − value in the same node.

The first of them is again the calculation of the value of the trial traction – the interpolation or futher simplification of the faulting model to a plain strike slip or dip slip is needed. All components directly at the fault need to be calculated using the modified FD formulas, which take into account the division of the space by the fault boundary. The exception is σ_{13}, that doesn't require knowledge of any velocity components on the other side of the fault. Discontinuus $\sigma_{13}^{\pm}$ can be therefore acquired on both sides using the second or forth order FD formulas.

The shear velocity components $(v_1^{\pm})_{I,J_F,K}$ and $(v_3^{\pm})_{I\frac{1}{2},J_F,K\frac{1}{2}}$ will be calculated from (2.20). Index J_F denotes components directly at the fault. The elasto-dynamic forces at the fault $(f_1^{\pm})_{I,K}$ and $(f_3^{\pm})_{I\frac{1}{2},K\frac{1}{2}}$ need to be calculated using second order FD along 1 and 3 axes, but only one-sided FD along the 3 axis. For the purpose of the body force calculation, the traction components σ_{12}, σ_{23} are considered zero at the boundary:

$$(f_1^{\pm})_{I,K} = \Delta h^2 \Big[(D_1^{(2)} \sigma_{11}^{\pm})_{I,J_F,K} + (D_3^{(2)} \sigma_{13}^{\pm})_{I,J_F,K} \pm (\sigma_{12})_{I,J_F^{\pm\frac{1}{2}},K} \Big] \tag{2.29}$$

$$(f_3^{\pm})_{I\frac{1}{2},K\frac{1}{2}} = \Delta h^2 \Big[(D_1^{(2)} \sigma_{13}^{\pm})_{I\frac{1}{2},J_F,K\frac{1}{2}} + (D_3^{(2)} \sigma_{33}^{\pm})_{I\frac{1}{2},J_F,K\frac{1}{2}} \pm (\sigma_{23})_{I\frac{1}{2},J_F^{\pm\frac{1}{2}},K\frac{1}{2}} \Big] \tag{2.30}$$

Normal stress component σ_{22} is continuus at the fault, while σ_{11} and σ_{33} are not. They all require partial derivative of v_2 along the axis 3. The central difference formula is again switched to the one-sided one. The value $(v_2)_{I\frac{1}{2},J_F,K}$ is acquired from the condition on continuus σ_{22} and v_2. Equating formulas for its

plus and minus sides leads to (for spatialy constant λ and μ)

$$\frac{4(\lambda+2\mu)}{\Delta h}(v_2)_{I^{\frac{1}{2}},J_F,K} = \frac{2(\lambda+2\mu)}{\Delta h}\Big[(v_2)_{I^{\frac{1}{2}},J_F^{-\frac{1}{2}},K} + (v_2)_{I^{\frac{1}{2}},J_F^{\frac{1}{2}},K}\Big]$$
$$+\frac{\lambda}{\Delta h}\Big[-(D_1^{(2)}v_1^-)_{I^{\frac{1}{2}},J_F,K} - (D_3^{(2)}v_3^-)_{I^{\frac{1}{2}},J_F,K} + (D_1^{(2)}v_1^+)_{I^{\frac{1}{2}},J_F,K} + (D_3^{(2)}v_3^+)_{I^{\frac{1}{2}},J_F,K}\Big]. \tag{2.31}$$

One sided difference of v_2 is used to calculate the rest of the stress components at the fault:

$$\frac{(\sigma_{11}^{\pm})^{N^{\frac{1}{2}}}_{I^{\frac{1}{2}},J_F,K} - (\sigma_{11}^{\pm})^{N^{-\frac{1}{2}}}_{I^{\frac{1}{2}},J_F,K}}{\Delta t} = (\lambda+2\mu)(D_1^{(2)}v_1^{\pm})^N_{I^{\frac{1}{2}},J_F,K}$$
$$+\lambda(D_3^{(2)}v_3^{\pm})^N_{I^{\frac{1}{2}},J_F,K} \pm \lambda\frac{(v_2)^N_{I^{\frac{1}{2}},J_F,K} - (v_2)^N_{I^{\frac{1}{2}},J_F,K}}{\Delta h/2}, \tag{2.32}$$

$$\frac{(\sigma_{22})^{N^{\frac{1}{2}}}_{I^{\frac{1}{2}},J_F,K} - (\sigma_{22})^{N^{-\frac{1}{2}}}_{I^{\frac{1}{2}},J_F,K}}{\Delta t} = \lambda(D_1^{(2)}v_1^{\pm})^N_{I^{\frac{1}{2}},J_F,K}$$
$$+\lambda(D_3^{(2)}v_3^{\pm})^N_{I^{\frac{1}{2}},J_F,K} \pm (\lambda+2\mu)\frac{(v_2)^N_{I^{\frac{1}{2}},J_F,K} - (v_2)^N_{I^{\frac{1}{2}},J_F,K}}{\Delta h/2}, \tag{2.33}$$

$$\frac{(\sigma_{33}^{\pm})^{N^{\frac{1}{2}}}_{I^{\frac{1}{2}},J_F,K} - (\sigma_{33}^{\pm})^{N^{-\frac{1}{2}}}_{I^{\frac{1}{2}},J_F,K}}{\Delta t} = \lambda(D_1^{(2)}v_1^{\pm})^N_{I^{\frac{1}{2}},J_F,K}$$
$$+(\lambda+2\mu)(D_3^{(2)}v_3^{\pm})^N_{I^{\frac{1}{2}},J_F,K} \pm \lambda\frac{(v_2)^N_{I^{\frac{1}{2}},J_F,K} - (v_2)^N_{I^{\frac{1}{2}},J_F,K}}{\Delta h/2}. \tag{2.34}$$

The use of the second order FD formulas causes unwanted high frequency oscillations. Dalguer and Day [2007] uses artificial viscous damping of force $f_i^{\pm}$ to supress them. Damped force

$$\acute{f}_i^{\pm} = f_i^{\pm} + \eta\dot{f}_i^{\pm} \tag{2.35}$$

is used to calculate shear velocity components at the fault. Damping coefficient η depends on the time dicretization parameter $\eta = \eta_s\Delta t$, with ideal value of η_s being 0.3. This value was determined experimentally to have the lowest impact on rupture velocity speed by Dalguer and Day [2007]. Dependence on Δt ties damping also to the space discretization (through CFL criterium) and damps frequencies close to the grid Nyquist limit.

2.4 Slip weakening friction

Slip weakening friction law was first introduced by Ida [1973], and is extensively used in dynamic rupture simulations. Value of the frictional coefficient depends only on slip

$$S = \sigma_n\mu_f(s). \tag{2.36}$$

For the rupture to propagate, the frictional force needs to decrease with continual sliding (slip weakening). We consider linear slip weakening relationship in the form introduced by Andrews [1976]:

$$\mu_f(s) = \begin{cases} \mu_s - (\mu_s - \mu_d)s/D_c, & \text{if } s < D_c \\ \mu_d, & \text{if } s \geq D_c, \end{cases} \tag{2.37}$$

where μ_s, μ_d and D_c are model parameters: Static friction coefficient μ_s is a value of friction at the beginning of the sliding, friction then linearly drops to the dynamic friction $\mu_d < \mu_s$ over the slip interval of D_c as can be seen in Fig (2.5).

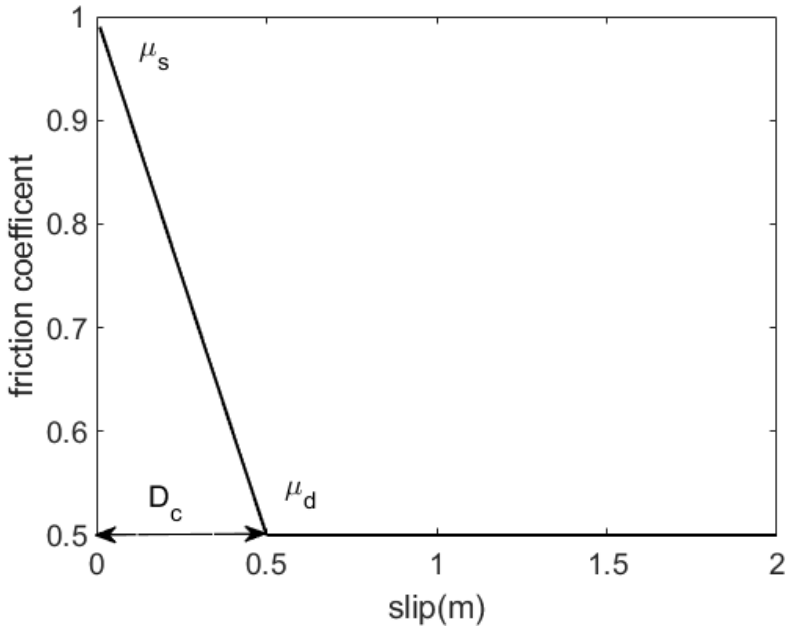

Figure 2.5: Slip weakening friction law (black line) with labeled values of static (μ_s) and dynamic (μ_d) friction coefficients. Critical slip D_c is marked by arrows.

The calculation of the frictional force during a dynamic rupture simulation requires knowledge of slip at every time level. That is acquired by the integration of the slip rate $\dot{s}$. Using the time staggered location of the slip and the slip rate, the integration is straightforward:

$$s^{N\frac{1}{2}} = s^{N^-\frac{1}{2}} + \Delta t \dot{s}^N. \tag{2.38}$$

Frictional strength can then be directly calculated at all desired time levels:

$$S^{N\frac{1}{2}} = \begin{cases} \sigma_n[\mu_s - (\mu_s - \mu_d)s^{N\frac{1}{2}}/D_c], & \text{if } s^{N\frac{1}{2}} < D_c \\ \sigma_n \mu_d, & \text{if } s^{N\frac{1}{2}} \geq D_c. \end{cases} \tag{2.39}$$

2.5 Rate and state friction with fast velocity weakening

2.5.1 The law of friction

Rate and state type laws were developed by Dieterich [1986] and Ruina [1983] based on friction experiments with changing sliding velocity (velocity jump and slide hold slide experiments). Friction depends on a sliding velocity and a state variable ψ

$$S = \sigma_n \mu_f(\dot{s}, \psi). \tag{2.40}$$

The state variable describes the state of the contacts at the surface boundary. Its behaviour follows the slip weakening law with contacts wearing down through sliding, ψ decreases during the sliding period. In addition to this behavior, increase of the state variable (and friction) during a period of slower sliding is possible, which simulates healing of the fracture. Behavior of the state is described by an evolution law, which is an ordinary differential equation:

$$\frac{d\psi}{dt} = F(s, \dot{s}, \psi). \tag{2.41}$$

Originally, the friction experiments were done at low speeds of the order of milimeters per second [Dieterich, 1979]. Experiments with higher rates became available when rotating disks of studied material were used. Two main effects were observed – frictional instability at medium rates between 1 mm/s and 10 cm/s [Reches and Lockner, 2010] and rapid decrease of the friction at rates above 10 cm/s [Di Toro et al., 2004, Goldsby and Tullis, 2011]. The first effect is attributed to the lubrication of the fault by spontaneous development of the gauge created at the frictional surface [Reches and Lockner, 2010]. The second effect is important for the rupture dynamics, since it occurs at slip rates observed typically during eartquakes. Flash heating of asperities (contacts) was suggested as a probable mechanism. The lifetime of the asperity was compared with time needed to weaken it through heating under a given velocity [Rice, 2006]. When the slip velocity is higher then weakening velocity $\dot{s}_w$, the asperity is weakened, when lower, it is not.

Unlike the slip weakening law, the rate and state type laws often do not allow for the surface to stop sliding ($\dot{s} = 0$). The whole fault is considered to be sliding, at initial non-zero slip rate $\dot{s}_{ini}$. This value is added rather as a regularization, it does not necessarily have a physical meaning. The traction is set to be always equal to the frictional strength, meaning that only the second case in (2.5) applies.

Several versions of the fast velocity weakening law are employed in the literature [Dunham et al., 2011, Gabriel et al., 2012]. We use the version used by Harris et al. [2018] because its use in their benchmark excercise will allow us to easily estimate the accuracy of the developed code. It consists of five interlinked

formulas:

$$
\begin{aligned}
S &= \sigma_n a \ \mathrm{arcsinh}\Big[\frac{\dot{s}}{2\dot{s}_0}\exp\Big(\frac{\psi}{a}\Big)\Big],\\
\frac{d\psi}{dt} &= -\frac{\dot{s}}{L}[\psi - \psi_{SS}],\\
\psi_{SS} &= a\log\Big[\frac{2\dot{s}_0}{\dot{s}}\ \sinh\Big(\frac{f_{SS}}{a}\Big)\Big],\\
f_{SS} &= f_w + \frac{f_{LV} - f_w}{\Big[1 + (\dot{s}/\dot{s}_w)^8\Big]^{1/8}},\\
f_{LV} &= f_0 - (b-a)\log\Big(\frac{\dot{s}}{\dot{s}_0}\Big).
\end{aligned}
\tag{2.42}
$$

When constant sliding velocity $\dot{s}$ is set and held for a sufficiently long time, the system develops into a steady state. The state variable ψ has its steady state value ψ_{SS} and frictional strength equals:

$$
\begin{aligned}
S_{SS} &= \sigma_n f_{SS}(\dot{s}),\\
f_{SS}(\dot{s}) &= f_w + \frac{f_{LV}(\dot{s}) - f_w}{\Big[1 + (\dot{s}/\dot{s}_w)^8\Big]^{1/8}},\\
f_{LV}(\dot{s}) &= f_0 - (b-a)\log\Big(\frac{\dot{s}}{\dot{s}_0}\Big).
\end{aligned}
\tag{2.43}
$$

Behavior in this steady state is explored first. For low values of $\dot{s}$, the steady state friction coefficient is basically equal to f_{LV} ('Low Velocity'). The developement of friction for increasing (but still small) $\dot{s}$ depends on the sign of $(b-a)$. For $b > a$ the friction law is velocity weakening and decreases, for $b < a$ it is velocity strenghtening. When $\dot{s} = \dot{s}_0$, $f_{SS} = f_0$. For very high values of $\dot{s}$ the friction coefficient drops to its minimal value f_w as $\sim 1/\dot{s}$.

The time dependent behavior of the friction for changing $\dot{s}$ is controlled by a differential equation for the state variable (2.42). The solution of the equation for the case of the velocity jump from one constant value toan other is an exponential increase or decrease of the state variable towards the steady state value:

$$
\psi(t) = [\psi(t_0) - \psi_{SS}(\dot{s})]\exp\left(-\frac{\dot{s}t}{L}\right) + \psi_{SS}(\dot{s}),
\tag{2.44}
$$

where $\psi(t_0)$ is the state variable value before the velocity jump, $\dot{s}$ is the new sliding velocity and ψ_{SS} the new steady state value. Time scale for this change is $L/\dot{s}$. In the case when the new velocity becomes smaller, the friction increases at the same time scale – the fault starts to heal. The development of friction for different velocities is shown in Fig 2.6.

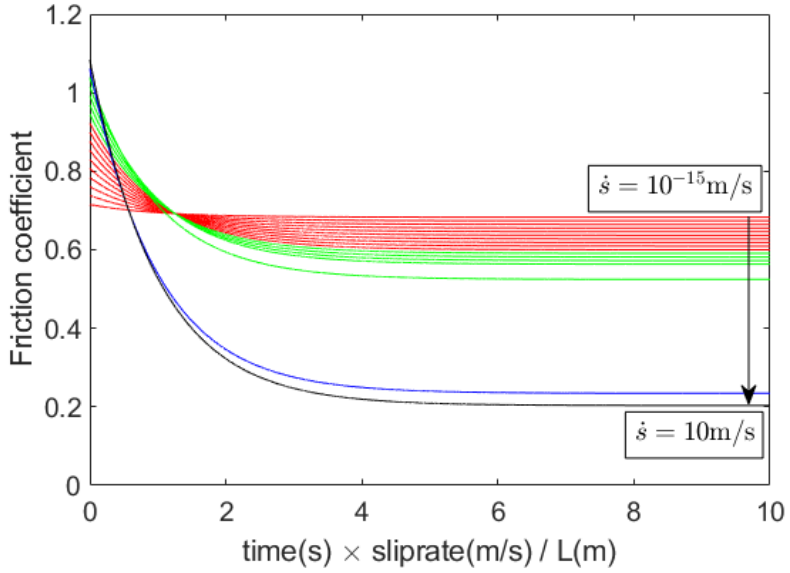

Figure 2.6: The development of friction coefficient after a velocity jump from $\dot{s}_{ini} = 10^{-16}$ to a higher velocity. Every line shows the development for the different velocity taken from the interval 10^{-15}m/s to 10m/s. The distribution of velocities is logarithmic $(10^{-15}, 10^{-14}, ...)$. Lines are colour-coded – red (from 10^{-15}m/s to 10^{-6}m/s $= \dot{s}_0$), green (from 10^{-5}m/s to 10^{-2}m/s $= \dot{s}_w$), blue (1m/s) and black (10m/s) . Friction parameters are in this case $f_0 = 0.6$ and $f_w = 0.2$.

2.5.2 Numerical implementation

Rupture simulation with the rate and state friction is more complicated then in the slip weakening case. It requires the solution of two coupled differential equations at the fault boundary – one for the shear velocity components (slip rate) and the other for the state variable ψ. The traction at split node method contains discretized formula for the slip rate based on the Newton's law (2.24). The second equation is the evolution law for the state variable. In the case of the fast velocity weakening friction from (2.42):

$$\frac{d\psi}{dt} = -\frac{\dot{s}}{L}[\psi - \psi_{SS}(\dot{s})] \tag{2.45}$$

The following approach to numerical discretization and solution of the velocity-state system of differential equations is adopted from Rojas et al. [2009]. Concrete procedure of solving this set of equations depends on the distribution of velocity and state variable between time levels. For the time staggered schemes, such as the scheme used in this work, the time-staggered distribution of slip rate and state variable (as in the Fig 2.7) is natural. The results are similarly accurate as using unstaggered distribution with high-order Rosenbrock integration [Rojas et al., 2009], while the coding is simpler.

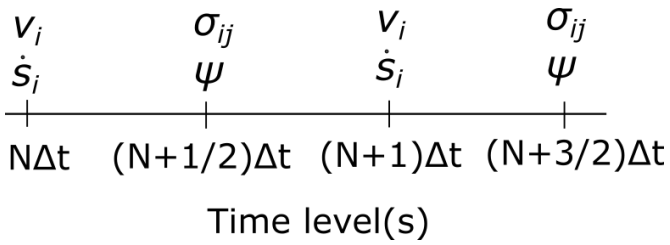

Figure 2.7: The time staggered position of slip rate and state variable

First step is the integration of the evolution law for ψ in the interval between two succesive time levels $(N-1/2)\Delta t$ and $(N+1/2)\Delta t$. Due to the time-staggered distribution, slip rate is positioned in the middle of this interval $N\Delta t$, and it will be approximated by this value over the whole interval $\dot{s}(t) = (\dot{s})^N, \forall t \in \Big((N-1/2)\Delta t, (N+1/2)\Delta t\Big)$. With the slip rate constant over the whole interval, the solution of the differential equation (2.44) applies:

$$\begin{aligned}
\psi^{N^{\frac{1}{2}}} &= (\psi^{N^{-\frac{1}{2}}} - \psi_{SS}(\dot{s}^N)) \exp(-\frac{\dot{s}^N \Delta t}{L}) + \psi_{SS}(\dot{s}^N), \\
\psi_{SS}(\dot{s}^N) &= a \log\Big[\frac{2s_0}{\dot{s}^N} \sinh\Big(\frac{f_{SS}(\dot{s}^N)}{a}\Big)\Big], \\
f_{SS}(\dot{s}^N) &= f_w + \frac{f_{LV}(\dot{s}^N) - f_w}{\Big[1 + (\dot{s}^N/s_w)^8\Big]^{1/8}}, \\
f_{LV}(\dot{s}^N) &= f_0 - (b-a) \log\Big(\frac{\dot{s}^N}{s_0}\Big).
\end{aligned} \tag{2.46}$$

Second step is the calculation of slip rate $(\dot{\mathbf{s}})^{N^1}$ from (2.22). Slipping will be allowed only in the direction of one shear component. Equation for the slip rate is therefore considered in scalar form:

$$(\dot{s})^{N^1} = (\dot{s})^N + \frac{\Delta t(M^- + M^+)}{\Delta h^{-2} M^- M^+} \left(\frac{M^-(f^+)^{N^{\frac{1}{2}}} - M^+(f^-)^{N^{\frac{1}{2}}}}{\Delta h^2 (M^- + M^+)} + (T)^{N^{\frac{1}{2}}} - T^0 \right). \tag{2.47}$$

Since the fault is considered to be always sliding, the second case from (2.28) will be directly substituted into (2.47) for traction and the first equation from (2.42) as the friction S:

$$(\dot{s})^{N^1} = (\dot{s})^N + \frac{\Delta t(M^- + M^+)}{\Delta h^{-2} M^- M^+} \left(\frac{M^-(f^+)^{N^{\frac{1}{2}}} - M^+(f^-)^{N^{\frac{1}{2}}}}{\Delta h^2 (M^- + M^+)} + S(\dot{s}^?, \psi^{N^{\frac{1}{2}}}) - T^0 \right). \tag{2.48}$$

Slip rate $\dot{s}^?$ on the right hand side of (2.48) cannot be set as a value of slip rate in the previous time level $\dot{s}^? = (\dot{s})^N$ (Forward Euler method), because the resulting scheme is highly unstable, especially for small values of slip rate, where the derivative of $\operatorname{arcsinh}(x)$ has its highest value. Backward Euler scheme ($\dot{s}^? = \dot{s}^{N^1}$) or trapezoidal scheme ($\dot{s}^? = (\dot{s}^N + \dot{s}^{N^1})/2$) needs to be used instead. Although trapezoidal scheme offers higher order accuracy, in reality it does not make much improvement. Backward Euler scheme will be used in this chapter, yieding

$$(\dot{s})^{N^1} = (\tilde{\dot{s}})^N + C \operatorname{arcsinh}\Big[\frac{(\dot{s})^{N^1}}{2s_0} \exp\Big(\frac{\psi^{N^{\frac{1}{2}}}}{a}\Big)\Big], \tag{2.49}$$

where

$$(\tilde{\dot{s}})^N = (\dot{s})^N + \frac{\Delta t(M^- + M^+)}{\Delta h^{-2} M^- M^+} \left(\frac{M^-(f^+)^{N^{\frac{1}{2}}} - M^+(f^-)^{N^{\frac{1}{2}}}}{\Delta h^2 (M^- + M^+)} - T^0 \right) \tag{2.50}$$

denotes the part of the formula (2.47) already explicitly calculated before the time level $(n+1)\Delta t$, and

$$C = \frac{\Delta t(M^- + M^+)}{\Delta h^{-2} M^- M^+} \sigma_n a. \tag{2.51}$$

Formula (2.49) is nonlinear and needs to be solved accordingly, for example with the Newton's method, which will be described next.

We want to find a new slip rate value $(\dot{s})^{N^1}$, that satisfies equation (2.49). This is equivalent to finding a root of a function

$$F\left((\dot{s})^{N^1}\right) = (\tilde{\dot{s}})^N - (\dot{s})^{N^1} + C \ \mathrm{arcsinh}\Big[\frac{(\dot{s})^{N^1}}{2s_0} \exp\Big(\frac{\psi^{N^{\frac{1}{2}}}}{a}\Big)\Big]. \tag{2.52}$$

In Newton's method the root w of the function $F(x)$, is found approximately by a succesive iteration:

$$w_{n+1} = w_n - \frac{F(w_n)}{F'(w_n)}, \tag{2.53}$$

where F' is the derivative of function F, and w_n is the approximate value of the root at the n-th iteration. Equation (2.49) is modified to simplify finding the solution. Solution is found for a substituted variable:

$$w = \ \mathrm{arcsinh}\Big[\frac{(\dot{s})^{N^1}}{2s_0} \exp\Big(\frac{\psi^{N^{\frac{1}{2}}}}{a}\Big)\Big] \tag{2.54}$$

instead of slip rate. This leads to a simple form of the function:

$$F(w) = (\tilde{\dot{s}})^N + Cw - \exp\Big(\frac{-\psi^{N^{\frac{1}{2}}}}{a}\Big) 2s_0 \mathrm{sinh}(w), \tag{2.55}$$

allowing to simply find its derivative:

$$F'(w) = C - \exp\Big(\frac{-\psi^{N^{\frac{1}{2}}}}{a}\Big) 2s_0 \mathrm{cosh}(w). \tag{2.56}$$

Natural choice of the starting value of w is its value at the previous time level:

$$w_0 = \ \mathrm{arcsinh}\Big[\frac{(\dot{s})^{N}}{2s_0} \exp\Big(\frac{\psi^{N^{\frac{1}{2}}}}{a}\Big)\Big]. \tag{2.57}$$

Formula (2.53) is then applied iteratively until the difference between succesive values of w (the error of the approximation) is lower then a chosen value – in our implementation 10^{-5} for a single precision calculation and 10^{-8} for a double precision one. The value of slip rate solving (2.49) is calculated from the substitution (2.54):

$$(\dot{s})^{N^1} = \frac{2s_0 \ \sinh(w)}{\exp\Big(\frac{\psi^{N^{\frac{1}{2}}}}{a}\Big)}. \tag{2.58}$$

The discrete solution of the fault boundary conditions with the fast velocity weakening rate and state law using the traction at split node method consists of application of formulas (2.46) to acquire new value of the state variable and Newton's method solution of (2.49) to acquire the new value of the slip rate. This is done at every node at the fault surface independently.

2.6 Cohesive zone

The part of the fault behind the crack-tip, where the traction drops from its static to its dynamic value, is called cohesive (or process) zone Λ. The resolution of the cohesive zone (amount of discrete points per cohesive zone) is the main parameter controlling the accuracy of the numerical simulation [Dalguer and Day, 2006]. Indeed, the cohesive zone is the part of the fault, where the nonlinear boundary condition on stress (2.5) is enforced, and where changes in tractions and slip rates are very sharp.

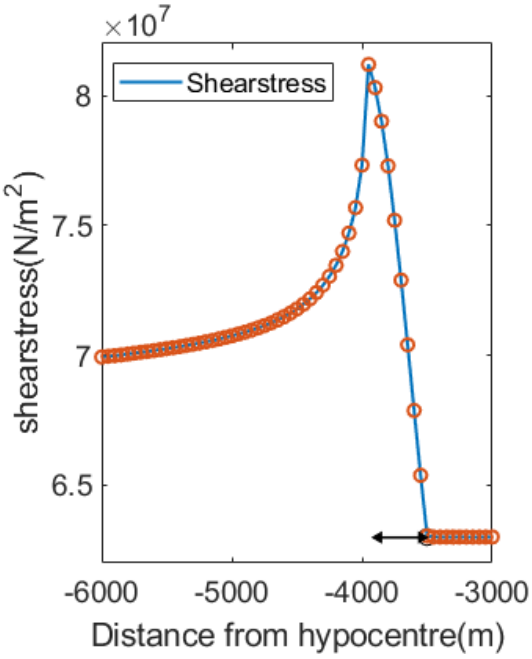

Figure 2.8: Cohesive zone behind a crack-tip – snapshot of spatial dependence of the shear stress for the linear slip weakening law. Arrow defines the cohesive zone. Red circles are values of the traction at discrete points.

Figure (2.8) shows an example of the spatial dependence of the traction in the rupture propagation, iliustrating the importance of the proper resolution of the cohesive zone. The discretization in this particular case was $\Delta h = 50$m; with lower resolution (higher Δh), the accuracy would drop considerably. Slip rate and traction behind the crack-tip vary quickly also in time. However, the situation is much better here, because the CFL criterion ensures that the time resolution of the 'cohesive time interval' will be much better resolved (see Fig 2.9 for temporal discretization of traction).

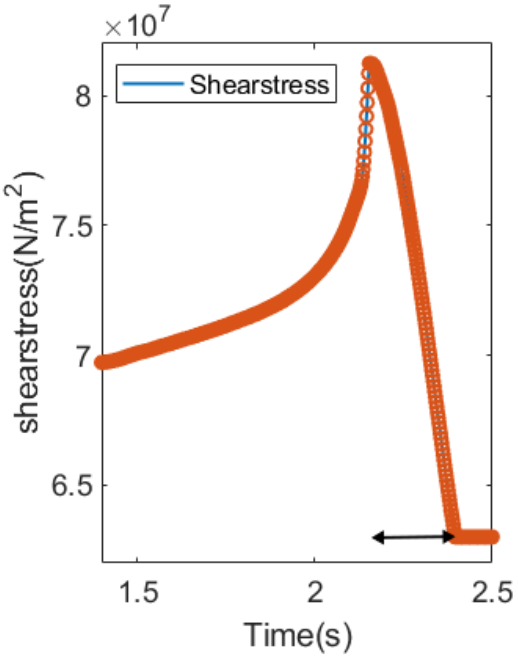

Figure 2.9: The same as in Fig 2.8, but for the temporal discretization.

Having the knowledge of the cohesive zone size before the simulation is run would be useful, because it would allow us to determine the disretization necessary to reach the desired accuracy. However, the dependence of the cohesive zone size on physical parameters of a heterogenous dynamic model is non-trivial. Several approximated estimations are used [Bizzarri et al., 2012]. Analysis of energy release rate and fracture energy offers an upper bound estimate (for the rupture velocity close to zero) of the cohesive zone size

$$\Lambda_{II}(\mathbf{x}) = \frac{9\pi D_c(\mathbf{x})\mu(\mathbf{x})}{32\sigma_n(\mathbf{x})(\mu_s(\mathbf{x}) - \mu_d(\mathbf{x}))} \tag{2.59}$$

for Mode II and

$$\Lambda_{III}(\mathbf{x}) = \frac{9\pi D_c(\mathbf{x})\mu(\mathbf{x})/(1-\nu(\mathbf{x}))}{32\sigma_n(\mathbf{x})(\mu_s(\mathbf{x}) - \mu_d(\mathbf{x}))} \tag{2.60}$$

for Mode III cracks (ν is Poisson ratio). For non-zero values of the rupture velocity, the cohesive zone will shrink below this estimate, by factors

$$A_{II} = \frac{(1-\nu)\beta^2\left(4(1-v_r^2/v_\beta^2)^{1/2}(1-v_r^2/v_\beta^2)^{1/2} - (2-v_r^2/v_\beta^2)^2\right)}{v_r^2(1-v_r^2/v_\beta^2)^{1/2}} \tag{2.61}$$

for a mode II crack and

$$A_{III} = (1-v_r^2/v_\beta^2)^{1/2}. \tag{2.62}$$

for a mode III crack [Day et al., 2005].

After the simulation, the cohesive zone can be established when knowing the whole field of traction (space and time dependent) by measuring the distance between the maximum and minimum tractions in the direction of the rupture propagation. This approach poses complications when the direction of the rupture propagation changes. In this work we will use the following local estimate of the cohesive zone where the rupture direction and rupture velocity is assumed to not

change locally during the propagation throughout the cohesive zone. For every point at the fault the rupture velocity v_r is calculated frrom the eikonal equation as the inverse value of the magnitudeof the gradient of the rupture time t_r

$$v_r(\mathbf{x}) = \frac{1}{\sqrt{\left(\frac{\partial t_r(\mathbf{x})}{\partial x_1}\right)^2 + \left(\frac{\partial t_r(\mathbf{x})}{\partial x_2}\right)^2 + \left(\frac{\partial t_r(\mathbf{x})}{\partial x_3}\right)^2}}, \tag{2.63}$$

The cohesive zone is then estimated as

$$\Lambda(\mathbf{x}) = v_r(\mathbf{x})\left[t_s(\mathbf{x}) - t_r(\mathbf{x})\right] \tag{2.64}$$

from the rupture time t_r (time of maximum traction in the position $\mathbf{x}$) and time t_s for which the traction is minimal in the position $\mathbf{x}$. For the slip weakening friction law, t_s is also the time in which the value of slip is equal to D_c.

When the fast velocity weakening friction is assumed, the traction doesn't drop at the same rate over the whole cohesive zone. Majority of the stress drop occurs in a much smaller area behind the crack-tip [Rojas et al., 2009], see Fig. 2.10.

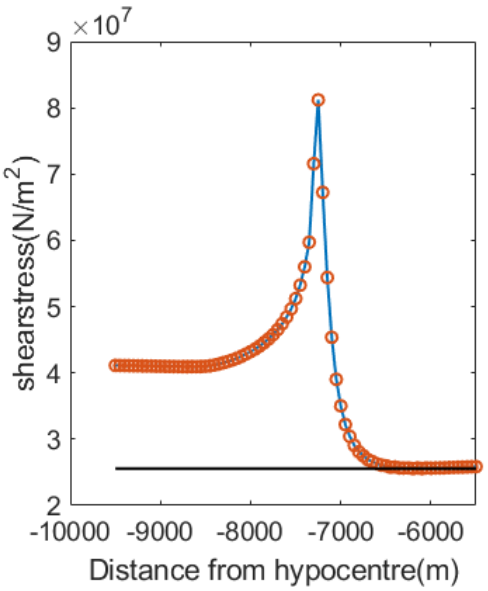

Figure 2.10: Cohesive zone behind a crack-tip – snapshot of spatial dependence of the shear stress for fast velocity weakening friction law. The black line shows the value of minimum traction.

The resolution of this effective cohesive zone is more important for the simulation accuracy. Effective cohesive zone $\Lambda_e(\mathbf{x})$ is calculated in this case as

$$\Lambda_e(\mathbf{x}) = v_r(\mathbf{x})\left[t_e(\mathbf{x}) - t_r(\mathbf{x})\right], \tag{2.65}$$

where t_e is set as a time, where the traction would reach the minimum value if the drop proceded linearly with the rate equal to the maximum derivative of the traction.

3. Outer boundary conditions

At the border of the computational domain the outer boundary conditions are in place. Two types of boundary conditions are described in this chapter – free surface (Section 3.1) and absorbing boundary condition (Section 3.2).

3.1 Free surface

The interface between the Earth material and atmosphere will be considered to coincide with the 1-2 plane, where zero traction condition is applied,

$$\sigma_{ij}\Big|_{(z=z_s)} n_j = T_i = (\sigma_{13}, \sigma_{23}, \sigma_{33}) = 0, \tag{3.1}$$

where $n_j = (0, 0, 1)$ is the normal to the free surface and z_s is the z position of the free surface plane.

The spatial differences of the velocity or stress components below and at the free surface are calculated using the 4th order central FD formula. This requires the knowledge of the velocity and stress components at nodes above the free surface. Their values will be set so that condition (3.1) is satisfied at the free surface for all the three components of traction. This is known as a stress imaging method [Graves, 1996]. Alternatives to this approch are to set material parameters ρ, λ, μ above the free surface to approach zero (vacuum formulation [Graves, 1996]), or to change the FD formulas near the free surface to one-sided ones (AFDA method [Kristek et al., 2002]), which brings improvement in the modeling of the surface waves over longer distances, but is probably unnecessary for the rupture propagagation simulations.

There are two ways in which the free surface (FS) plane can cut through the staggered FD grid – through nodes, where σ_{33} is explicitly calculated, or nodes with σ_{13} and σ_{23}. The first choice is called as the H formulation, while the second as the W formulation [Kristek et al., 2002]. In terms of the accuracy the difference between both formulations is minimal [Gottschämmer and Olsen, 2001]. The W formulation is used in this work – it is more natural choice because of the orientation of the FD grid. The position of the FS plane in our staggered grid is shown in Fig 3.1 together with the positions of the required imaged values above the FS. The position of the nodes directly at the plane on the third axis is $z_s = K_s \Delta h$.

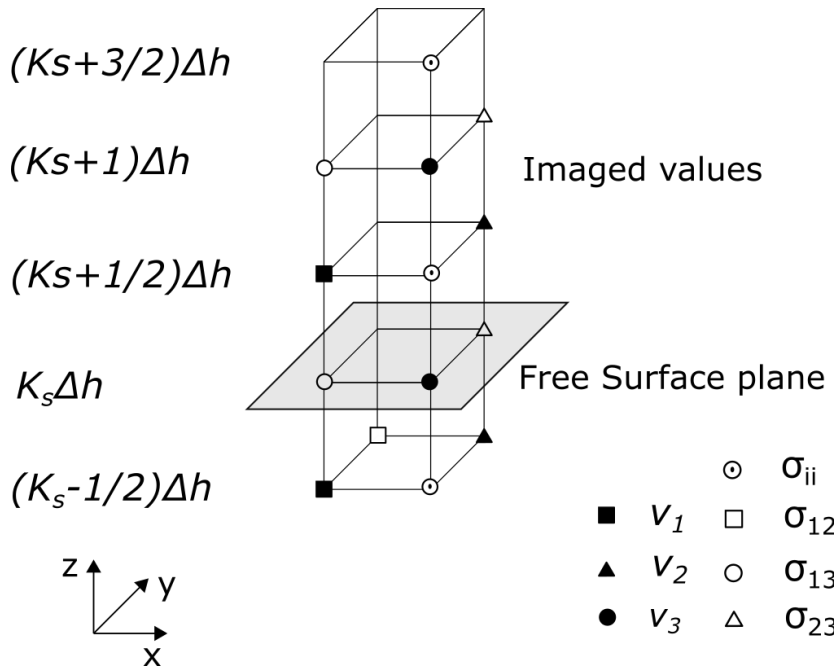

Figure 3.1: Position of the free surface plane in the staggered FD grid in the W formulation. Free surface plane is denoted by a grey plane. Nodes above the plane contain imaged values of the velocity and stress components. Only those imaged values necessary for the calculation are shown.

Both shear components of traction at the free surface are set to zero

$$\begin{aligned}(\sigma_{13})_{IJK_s} &= 0\\ (\sigma_{23})_{I^{\frac{1}{2}}J^{\frac{1}{2}}K_s} &= 0\end{aligned} \tag{3.2}$$

and velocity component 3 at the free surface can be calculated using the standard 4th order FD formula. There are 4 stress and 3 velocity values above the free surface required for the central FD formulas on nodes below and at the free surface. All will be set to impose the zero stress condition on traction either directly or for its interpolated value. Imaged values of the stress components 11, 22 and 12 are not needed in this respect.

The normal component of traction σ_{33} is not explicitly calculated at the free surface plane, therefore the value interpolated from two closest points$(\sigma_{33})_{I^{\frac{1}{2}}JK_s^{\frac{1}{2}}}$ and $(\sigma_{33})_{I^{\frac{1}{2}}JK_s^{-\frac{1}{2}}}$ is set to zero. This yields antisymmetry of the normal traction component below free surface and the imaged value above:

$$(\sigma_{33})_{I^{\frac{1}{2}}JK_s^{\frac{1}{2}}} = -(\sigma_{33})_{I^{\frac{1}{2}}JK_s^{-\frac{1}{2}}}. \tag{3.3}$$

Similarly, the other imaged values of stress components above the free surface are set antisymetrically to their values below:

$$\begin{aligned}(\sigma_{13})_{IJK_s^1} &= -(\sigma_{13})_{IJK_s^{-1}}\\ (\sigma_{23})_{I^{\frac{1}{2}}J^{\frac{1}{2}}K_s^1} &= -(\sigma_{23})_{I^{\frac{1}{2}}J^{\frac{1}{2}}K_s^{-1}}\\ (\sigma_{33})_{I^{\frac{1}{2}}JK_s^{\frac{3}{2}}} &= -(\sigma_{33})_{I^{\frac{1}{2}}JK_s^{-\frac{3}{2}}},\end{aligned} \tag{3.4}$$

which yields average zero value between the node below the surface and the imaged one.

Imaged velocity components are set from second order spatial discretization of time derivated Hooke's law at the free surface. It is written for the component of traction, with the right-hand side set to be zero due to (3.1). Hooke's law for 13 component of traction at the free surface gives:

$$\begin{aligned} 0 = (D_t\sigma_{13})^N_{IJK_s} &= \frac{\mu}{\Delta h}\left[(v_1)^N_{IJK_s^{\frac{1}{2}}} - (v_1)^N_{IJK_s^{-\frac{1}{2}}} + (v_3)^N_{I^{\frac{1}{2}}JK_s} - (v_3)^N_{I^{-\frac{1}{2}}JK_s}\right] \\ (v_1)^N_{IJK_s^{\frac{1}{2}}} &= (v_1)^N_{IJK_s^{-\frac{1}{2}}} - \left[(v_3)^N_{I^{\frac{1}{2}}JK_s} - (v_3)^N_{I^{-\frac{1}{2}}JK_s}\right] \end{aligned} \tag{3.5}$$

Similarly, for the 23 component of stress at the free surface:

$$\begin{aligned} 0 = (D_t\sigma_{23})^N_{I^{\frac{1}{2}}J^{\frac{1}{2}}K_s} &= \frac{\mu}{\Delta h}\left[(v_2)^N_{I^{\frac{1}{2}}J^{\frac{1}{2}}K_s^{\frac{1}{2}}} - (v_2)^N_{I^{\frac{1}{2}}J^{\frac{1}{2}}K_s^{-\frac{1}{2}}} + (v_3)^N_{I^1J^{\frac{1}{2}}K_s} - (v_3)^N_{IJ^{\frac{1}{2}}K_s}\right] \\ (v_2)^N_{I^{\frac{1}{2}}J^{\frac{1}{2}}K_s^{\frac{1}{2}}} &= (v_2)^N_{I^{\frac{1}{2}}J^{\frac{1}{2}}K_s^{-\frac{1}{2}}} - \left[(v_3)^N_{I^{\frac{1}{2}}J^1K_s} - (v_3)^N_{I^{\frac{1}{2}}JK_s}\right] \end{aligned} \tag{3.6}$$

The 33 component of stress is not calculated directly at the free surface, but Hooke's law can be written for the time differences of both sides in (3.3),

$$\begin{aligned} (D_t\sigma_{33})^N_{I^{\frac{1}{2}}JK_s^{\frac{1}{2}}} &= \frac{\lambda+2\mu}{\Delta h}\left[(v_3)^N_{I^{\frac{1}{2}}JK_s^1} - (v_3)^N_{I^{\frac{1}{2}}JK_s}\right] \\ &\quad + \frac{\lambda}{\Delta h}\left[(v_1)^N_{I^1JK_s^{\frac{1}{2}}} - (v_1)^N_{IJK_s^{\frac{1}{2}}} + (v_2)^N_{I^{\frac{1}{2}}J^{\frac{1}{2}}K_s^{\frac{1}{2}}} - (v_2)^N_{I^{\frac{1}{2}}J^{-\frac{1}{2}}K_s^{\frac{1}{2}}}\right] \\ (D_t\sigma_{33})^N_{I^{\frac{1}{2}}JK_s^{-\frac{1}{2}}} &= \frac{\lambda+2\mu}{\Delta h}\left[(v_3)^N_{I^{\frac{1}{2}}JK_s} - (v_3)^N_{I^{\frac{1}{2}}JK_s^{-1}}\right] \\ &\quad + \frac{\lambda}{\Delta h}\left[(v_1)^N_{I^1JK_s^{-\frac{1}{2}}} - (v_1)^N_{IJK_s^{-\frac{1}{2}}} + (v_2)^N_{I^{\frac{1}{2}}J^{\frac{1}{2}}K_s^{-\frac{1}{2}}} - (v_2)^N_{I^{\frac{1}{2}}J^{-\frac{1}{2}}K_s^{-\frac{1}{2}}}\right] \end{aligned} \tag{3.7}$$

After substituting these into the time derivative of (3.3), we can express imaged velocity component 3

$$\begin{aligned} (v_3)^N_{I^{\frac{1}{2}}JK_s^1} = (v_3)^N_{I^{\frac{1}{2}}JK_s^{-1}} - \frac{\lambda}{\lambda+2\mu}\Big[&(v_1)^N_{I^1JK_s^{\frac{1}{2}}} - (v_1)^N_{IJK_s^{\frac{1}{2}}} \\ +&(v_1)^N_{I^1JK_s^{-\frac{1}{2}}} - (v_1)^N_{IJK_s^{-\frac{1}{2}}} + (v_2)^N_{I^{\frac{1}{2}}J^{\frac{1}{2}}K_s^{\frac{1}{2}}} - (v_2)^N_{I^{\frac{1}{2}}J^{-\frac{1}{2}}K_s^{\frac{1}{2}}} \\ &+(v_2)^N_{I^{\frac{1}{2}}J^{\frac{1}{2}}K_s^{-\frac{1}{2}}} - (v_2)^N_{I^{\frac{1}{2}}J^{-\frac{1}{2}}K_s^{-\frac{1}{2}}}\Big] \end{aligned} \tag{3.8}$$

Formulae (3.2, 3.4, 3.5, 3.6, 3.8) together constitute the stress imaging free surface method. When applied (with all other components at nodes at and below the free surface calculated using the standard 4th order FD formulas), the zero traction condition at the free surface is imposed.

3.2 Absorbing boundary conditions

Absorbing boundary conditions (ABCs) occupy domain borders, where further continuation of the material needs to be simulated. Free propagation of waves without any reflections is modeled at these boundaries. Two major approaches

are used in elastodynamic simulations [Moczo et al., 2007] – constructing the boundary condition from the extrapolation of waves or adding an absorbing layer, where the wave amplitude is gradually decreased.

The extrapolation of waves offers an attractively fast code, when a simple model of the wave is introduced and the extrapolation is performed with low order FD fomulas [Clayton and Engquist, 1977]. Improvements in accuracy [Higdon, 1991] typically come at the cost of very complicated equations and more memory demand [Moczo et al., 2007].

Absorbing layers are computationally more demanding, since the FD calculation is required in the added layer of non-zero thickness, i.e. the size of the computational domain increases. The main advantage of this approach is, however, that further improvement in accuracy can be achieved by simply widening the absorbing layer, while the extrapolation methods require direct changes in the code and using formulas of increasing complexity.

In this section the popular version of the absorbing layer approach called Perfectly Mached Layers (PML) is described. It was introduced for electromagnetic waves by [Berenger, 1994]. Here we follow papers by Kristek et al. [2009] and Collino and Tsogka [2001]. The second subsection describes approach calculation of the reflection coefficient of the PML layer, which we use to set the damping profile values.

3.2.1 Perfectly matched layers

Without loss of generality, let us assume wave propagation in the x_1 direction. At the border of the computational domain an absorbing layer is introduced, where the wave amplitude decrease by propagation in the x_1 direction is desired. This effect is attained by changing elastodynamic equation(1.4) in the layer as follows. We introduce a complex coordinate $\tilde{x}_1$ instead of x_1:

$$\begin{aligned} \rho\frac{\partial v_i}{\partial t} &= \frac{\partial \sigma_{1i}}{\partial \tilde{x}_1} + \frac{\partial \sigma_{ji}}{\partial x_j}, & j \neq 1 \\ \frac{\partial \sigma_{ij}}{\partial t} &= c_{ijk1}\frac{\partial v_k}{\partial \tilde{x}_1} + c_{ijkl}\frac{\partial v_k}{\partial x_l}, & l \neq 1, \end{aligned} \tag{3.9}$$

With relation between $\tilde{x}_1$ and x_1 defined in frequency domain as

$$\tilde{x}_1 = x_1 - \frac{\iota}{\omega}\int_0^{x_1} d_x(s)ds, \tag{3.10}$$

where 0 is set at the divide between both areas and d_x is a chosen damping profile (real, non-negative function of x_1). Plane wave solution of (3.9) now depends on the complex coordinate:

$$v_j = V_j \exp\left[-\iota(k_1\tilde{x}_1 + k_2x_2 + k_3x_3 - \omega t)\right] \tag{3.11}$$

which after resubstituting from [3.10], leads to the desired attenuated solution:

$$v_j = V_j \exp\left[-\iota(k_1x_1 + k_2x_2 + k_3x_3 - \omega t)\right] \exp\left[-\frac{k_1}{\omega}\int_0^{x_1} d_x(s)ds\right]. \tag{3.12}$$

This solution has same amplitude constants V_j, wave vector $k_i = (k_1, k_2, k_3)$ and angular frequency ω as (1.8) would have in the same area (with same material parameters), but its amplitudedecreases with the distance from $x_1 = 0$.

The relation (3.10) is defined in the frequency domain and the simulation is executed with equations in the time domain. Altered version of the elastodynamic equation in the layer is first obtained in the frequency domain by sustitution of (3.10) into (3.9). Return into the time domain provides the form for FD discretization.

First, we concentrate on the relationship between the partial derivative with respect to x_1 and with respect to $\tilde{x}_1$. It will be defined in the frequency domain for arbitrary function $\hat{f}(x_1, \omega)$:

$$\frac{\partial \hat{f}}{\partial x_1} = \frac{\partial \hat{f}}{\partial \tilde{x}_1} \frac{\partial \tilde{x}_1}{\partial x_1} \tag{3.13}$$

The derivative of (3.10) provides

$$\frac{\partial \tilde{x}_1}{\partial x_1} = 1 - \frac{\iota}{\omega} d_x \tag{3.14}$$

and by substituting, we get a formula to be substituted into the frequency domain elastodynamic equation

$$\frac{\partial \hat{f}}{\partial \tilde{x}_1} = \frac{\iota\omega}{\iota\omega + d_x} \frac{\partial \hat{f}}{\partial x_1} \tag{3.15}$$

Sums in equations (3.9) are splitted into two parts. The first part consists of all terms without $\frac{\partial}{\partial \tilde{x}_1}$, while the second with. Equations are decomposed accordingly into two parts – tangent part $\hat{\sigma}_{ij}^{\perp}, \hat{v}_i^{\perp}$ and parallel $\hat{\sigma}_{ij}^{\parallel}, \hat{v}_i^{\parallel}$:

$$\begin{aligned}
\rho\iota\omega\hat{v}_i^{\parallel} &= \frac{\partial \hat{\sigma}_{1i}}{\partial \tilde{x}_1} \\
\rho\iota\omega\hat{v}_i^{\perp} &= \frac{\partial \hat{\sigma}_{ji}}{\partial x_j} \\
\hat{v}_i &= \hat{v}_i^{\parallel} + \hat{v}_i^{\perp} \\
\iota\omega\hat{\sigma}_{ij}^{\parallel} &= c_{ijk1} \frac{\partial \hat{v}_k}{\partial \tilde{x}_1} \\
\iota\omega\hat{\sigma}_{ij}^{\perp} &= c_{ijkl} \frac{\partial \hat{v}_k}{\partial x_l}, \quad l \neq 1 \\
\hat{\sigma}_{ij} &= \hat{\sigma}_{ij}^{\parallel} + \hat{\sigma}_{ij}^{\perp}
\end{aligned} \tag{3.16}$$

where the parallel part means the part, whose evolution depends on the spatial derivative in the direction of attenuation. The tangent parts are not attenuated, and don't need any further changes. The substitution for $\partial \tilde{x}_1$ from is done in tangent parts:

$$\begin{aligned}
\rho\iota\omega\hat{v}_i^{\parallel} &= \frac{\iota\omega}{\iota\omega + d_x} \frac{\partial \hat{\sigma}_{1i}}{\partial x_1} \\
\iota\omega\hat{\sigma}_{ij}^{\parallel} &= \frac{\iota\omega}{\iota\omega + d_x} c_{ijk1} \frac{\partial \hat{v}_k}{\partial x_1},
\end{aligned} \tag{3.17}$$

and after simple algebra we get

$$\begin{aligned}
\rho(\iota\omega + d_x)\hat{v}_i^{\parallel} &= \frac{\partial \hat{\sigma}_{1i}}{\partial x_1} \\
(\iota\omega + d_x)\hat{\sigma}_{ij}^{\parallel} &= c_{ijk1} \frac{\partial \hat{v}_k}{\partial x_1},
\end{aligned} \tag{3.18}$$

which leads to the final form in the time domain:

$$\begin{aligned}
\rho\left(\frac{\partial v_i^{\parallel}}{\partial t} + d_x v_i^{\parallel}\right) &= \frac{\partial \sigma_{1i}}{\partial x_1} \\
\rho\frac{\partial v_i^{\perp}}{\partial t} &= \frac{\partial \sigma_{ji}}{\partial x_j}, \qquad j \neq 1 \\
v_i &= v_i^{\parallel} + v_i^{\perp} \\
\frac{\partial \sigma_{ij}^{\parallel}}{\partial t} + d_x \sigma_{ij}^{\parallel} &= c_{ijk1}\frac{\partial v_k}{\partial x_1} \\
\frac{\partial \sigma_{ij}^{\perp}}{\partial t} &= c_{ijkl}\frac{\partial v_k}{\partial x_l}, \quad l \neq 1 \\
\sigma_{ij} &= \sigma_{ij}^{\parallel} + \sigma_{ij}^{\perp},
\end{aligned} \tag{3.19}$$

The discretization of the partial derivatives on the right-hand side of (3.19) can be performed by using the second order (1.13) or forth order [1.16] finite difference formulas. Second order FD formulas and the intepolation in time looks like:

$$\begin{aligned}
\left(\frac{\partial v_i}{\partial t}\right)^{N^{\frac{1}{2}}} &= \frac{(v_i)^{N^1} - (v_i)^N}{\Delta t} \qquad \left(\frac{\partial \sigma_{ij}}{\partial t}\right)^{N} = \frac{(\sigma_{ij})^{N^{\frac{1}{2}}} - (\sigma_{ij})^{N^{-\frac{1}{2}}}}{\Delta t} \\
(v_i)^{N^{\frac{1}{2}}} &= \frac{(v_i)^{N^1} + (v_i)^N}{2} \qquad\qquad (\sigma_{ij})^N = \frac{(\sigma_{ij})^{N^{\frac{1}{2}}} - (\sigma_{ij})^{N^{-\frac{1}{2}}}}{2}.
\end{aligned} \tag{3.20}$$

These lead to the explicit formulas for both the stress and velocity components:

$$\begin{aligned}
(v_i^{\parallel})^{N^1} &= \frac{(v_i^{\parallel})^N(1 - \frac{1}{2}\Delta t d_x) + \frac{1}{\rho}D_1^{(2)}(\sigma_{i1})^{N^{\frac{1}{2}}}}{1 + \frac{1}{2}\Delta t d_x} \\
(v_i^{\perp})^{N^1} &= (v_i^{\perp})^N + \frac{1}{\rho}\left[D_2^{(2)}(\sigma_{i2})^{N^{\frac{1}{2}}} + D_3^{(2)}(\sigma_{i3})^{N^{\frac{1}{2}}}\right] \\
(v_i)^{N^1} &= (v_i^{\parallel})^{N^1} + (v_i^{\perp})^{N^1} \\
(\sigma_{ji}^{\parallel})^{N^{\frac{1}{2}}} &= \frac{(\sigma_{ji}^{\parallel})^{N^{-\frac{1}{2}}}(1 - \frac{1}{2}\Delta t d_x) + c_{ijk1}D_1^{(2)}(v_k)^N}{1 + \frac{1}{2}\Delta t d_x} \\
(\sigma_{ji}^{\perp})^{N^{\frac{1}{2}}} &= (\sigma_{ji}^{\perp})^{N^{-\frac{1}{2}}} + c_{ijkl}D_l^{(2)}(v_k)^N, \qquad l \neq 1 \\
(\sigma_{ij})^{N^{\frac{1}{2}}} &= (\sigma_{ij}^{\parallel})^{N^{\frac{1}{2}}} + (\sigma_{ij}^{\perp})^{N^{\frac{1}{2}}}
\end{aligned} \tag{3.21}$$

There is a summation over index k on the left-hand side of the formula for $(\sigma_{ji}^{\parallel})^{N^{\frac{1}{2}}}$ and the summation over k and l indexes in the formula for $(\sigma_{ji}^{\perp})^{N^{\frac{1}{2}}}$. The staggered position of the components is not explicitly written down in 3.21, formulas work in every node of the PML layer, with the exception of the outer boundary of the PML layer, where the components can be set to zero (Dirichlet condition).

3.2.2 Reflection and the damping profile

The absorbing layer has a finite thickness δ. Dirichlet boundary condition $v_i = 0$ is set at the outer border $x_1 = \delta$. We will calculate the reflection cofficient for

a planar wave for the combination of both the absorbing layer and the Dirichlet boundary condition to obtain an estimate on the damping profile shape. The extensive analysis of the wave reflection in the PML layer is done in Collino and Tsogka [2001]. We will consider a simplified case in this section, with only normal incident wave.

Let the Dirichlet boundary have a reflection coefficient R, dependent on the type of incident and reflected wave and wave vector k_i. In the case of normal incident wave with $k_2 = 0, k_3 = 0$, the reflection koefficient is equal to 1. Phase velocity of this wave is $v_f = \omega/k_1$. Reflection of the whole layer is weakened by attenuation - the wave travels the distance δ through the absorbing layer to the Dirichlet boundary and than travels back through the absorbing layer again.

The decrease in amplitude of the incident wave is given by $\exp\left[-\frac{k_1}{\omega}\int_0^\delta d_x(s)ds\right]$. The reflected wave propagates in the opposite direction, therefore its wave vector has opposite sign and the limits of the integration interchange, therefore the decrease in amplitude of the reflected wave is again $\exp\left[-\frac{k_1}{\omega}\int_0^\delta d_x(s)ds\right]$. Reflection coefficient of the whole layer is then:

$$R_{PML} = 1 \exp\left[-2\frac{k_1}{\omega}\int_0^\delta d_x(s)ds\right]. \tag{3.22}$$

Typical form of the damping profile is a power function [Komatitsch and Martin, 2007]:

$$d_x(x) = d_0\left(\frac{x}{\delta}\right)^N, \tag{3.23}$$

where $N > 1, d_0 > 0$ are chosen constants. Substituting (3.23) into the integral in (3.22), we get

$$R_{PML} = \exp\left[-\frac{d_0 2\delta}{v_f(N+1)}\right]. \tag{3.24}$$

We can acquire arbitrarily small reflection coefficient by increasing the value of d_0. However, this applies only for the case of continuus PDE. The discretized case (FD equations) will introduce reflections proportional to d_0, caused by the numerical numerical dispersion [Collino and Tsogka, 2001]. The concrete numerical application of PML then requires setting d_0 as a compromise between both the numerical dispersion that increases the reflection, and the size of the parameters of the damping profile, that (formula 3.24) decrease it.

4. Synthetic benchmarks

The assesment of accuracy of FD rupture propagation simulations is complicated because of the shortage of model cases with analytical solutions. The analytical solutions exist only for simplified models with prescribed rupture velocity [Madariaga, 1976, Aki and Richards, 2002].

Widely used discrete methods are typically consistent with partial differential equations (discretized formulas become PDR when taking limit of Δh and Δt to zero). For a sufficiently small discretization step, the solution is practically invariant to further decrease of the step, but that doesn't prove convergence, because the real solution is unknown.

It is possible to test several different methods (finite difference, boundary integral, finite element, discontinuus Galerkin) and asses the similarity of the solutions. This was done first for a homogenous medium and a vertical fault model for the finite difference and boundary integral methods [Day et al., 2005].

The tests in this Thesis follow a popular successor of these original tests – the SCEC/USGS Spontaneous Rupture Code Verification Project [Harris et al., 2009, 2018], which is a set of benchmark excercises used to compare a wide range of numerical methods. The main webpage of this benchmark suite is `http://scecdata.usc.edu/cvws/`. It contains descriptions of the excercises and results generated by 10–20 different solvers. There are three types of results that are compared: time evolution of physical quantities at chosen points at the fault (slip, slip rate, traction, state variable), seismograms at off-fault positions and rupture time contour plots – lines showing the position of the rupture tip at every second.

We evaluate the accuracy of the improved FD3D_TSN code using two benchmarks – TPV5 (Section 4.1) and TPV104 (Section 4.2) using rupture model with the slip weakening and fast velocity weakening friction, respectively. Our solution will be compared with results of the FaultMod code [Barall, 2009], whose author is also one of the main authors of this benchmark. FaultMod uses finite elements method with its own technique to accomodate the fault boundary condition (called differential node) and using artificial damping in the whole domain.

Expectations on the accuracy differ among benchmarks. First benchmark TPV5 (description and results in Section 4.1) is a well established problem and all methods are routinely tested with it. The variability between solutions generated by different solvers is very small as can be seen in Fig 4.1. Despite the diversity of the methods, the lines are practically indistinguishable. Oscillations are a typical part of discrete solutions and are not visible in the graph due to the use of artifical damping (as will be in the case of FD3D) or due to the application of a filter on the simulated time series.

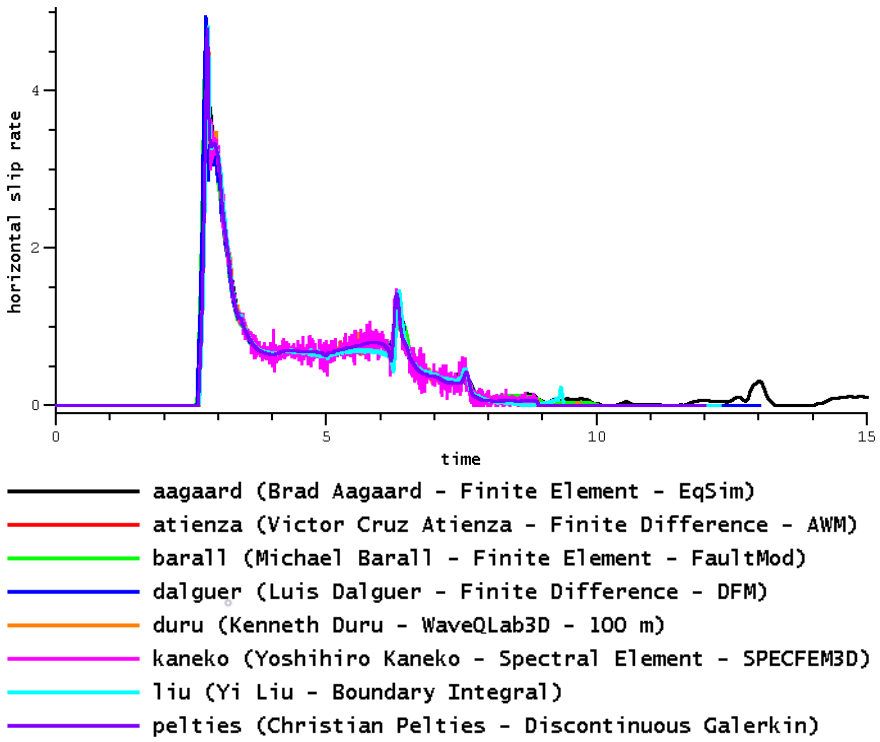

Figure 4.1: Slip rates at a chosen point on the fault (P8 in Fig 4.4) in the TPV5 benchmark calculated using different solvers (adopted from the webpage of Harris et al. [2018]).

The TPV104 benchmark (Section 4.2) is more numerically challenging, due to the more complex friction law, higher slip rates and narrower cohesive zone. Fig 4.2 shows solutions provided by several authors, with more noticable differences in slip rates and rupture time.

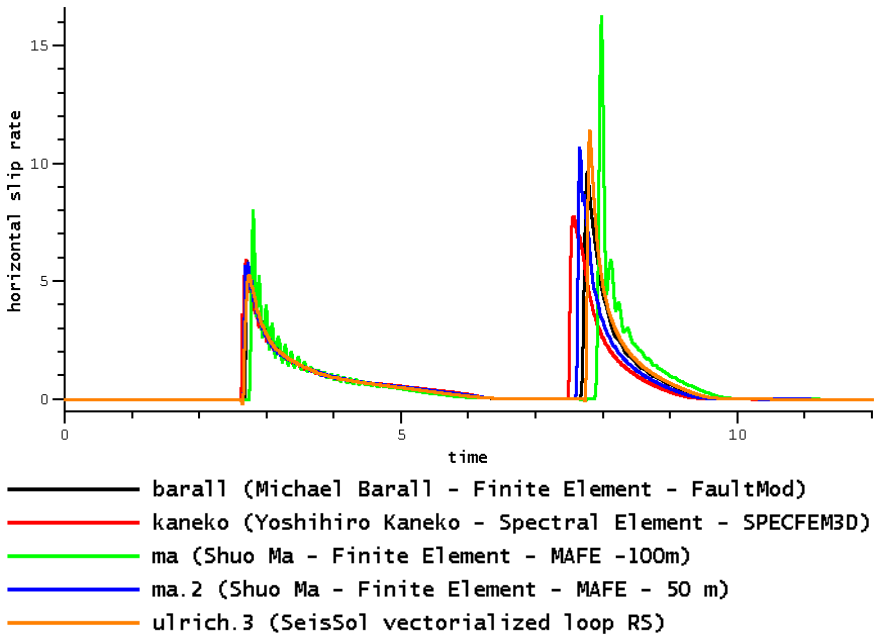

Figure 4.2: Slip rates at a chosen point on the fault (P8 in Fig 4.21) in the TPV104 benchmark calculated using different solvers (adopted from the webpage of Harris et al. [2018]).

4.1 TPV5 benchmark

The TPV5 benchmark tests the accuracy in the case of the slip-weakening friction law. The material around the fault is considered to be homogeneous, parameters ρ, v_p and v_s are specified in Table 4.1.

ρ	v_p	v_s
2670kg/m^3	6000m/s	3434m/s

Table 4.1: Material parameters for the TPV5 benchmark.

The space is bounded by a planar free surface boundary at the top and the fault is vertical. The rupture propagates over a 30x15 km large area. The static friction coefficient μ_s is set to 10000 outside of this area, thus effectvely stopping the rupture. The prestress is set to act in the horizontal direction, $\mathbf{T_0} = (T_0, 0, 0)$, which implies a strike-slip rupture. Dynamic parameters in the fault area are specified in the Table 4.2.

σ_n	μ_s	μ_d	T_0	D_c
120MPa	$0,677$	$0,525$	70MPa	0.4m

Table 4.2: Dynamic parameters for the TPV5 benchmark.

There are three heterogeneities in the prestress on the fault. All of them are square shaped, with the side equal to 3km. Coordinates of their centers and values of their prestress are described in Table 4.3 and displayed in Fig 4.3. Reference coordinate point is in the left down corner of the fault plane (Fig 4.3).

The prestress value at the central heterogeneity is higher than the static friction value of $0.677 \times 120\text{MPa} = 81,24\text{MPa}$, thus representing the nucleation patch.

Left heterogeneity	Vertical position $7,5$km	Horizontal position $7,5$km	T_0 78MPa
Nucleation zone	Vertical position $7,5$km	Horizontal position 15km	T_0 $81,6$MPa
Right heterogeneity	Vertical position $7,5$km	Horizontal position $22,5$km	T_0 62MPa

Table 4.3: Heterogeneity parameters for the TPV5 benchmark.

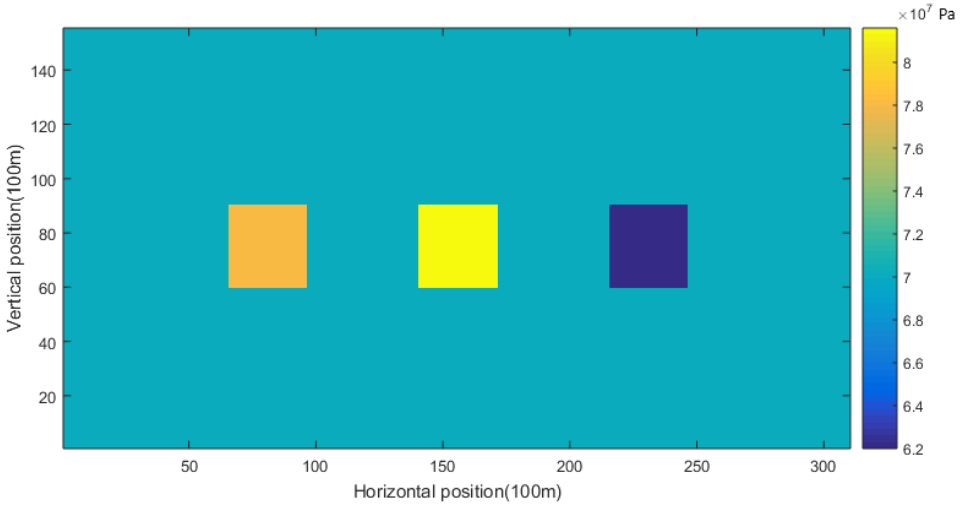

Figure 4.3: Horizontal prestress for the TPV5 benchmark.

The accuracy of the rupture properties is examined at predefined on-fault positions. There are 16 chosen positions in the TPV5 benchmark, as displayed in Fig 4.4.

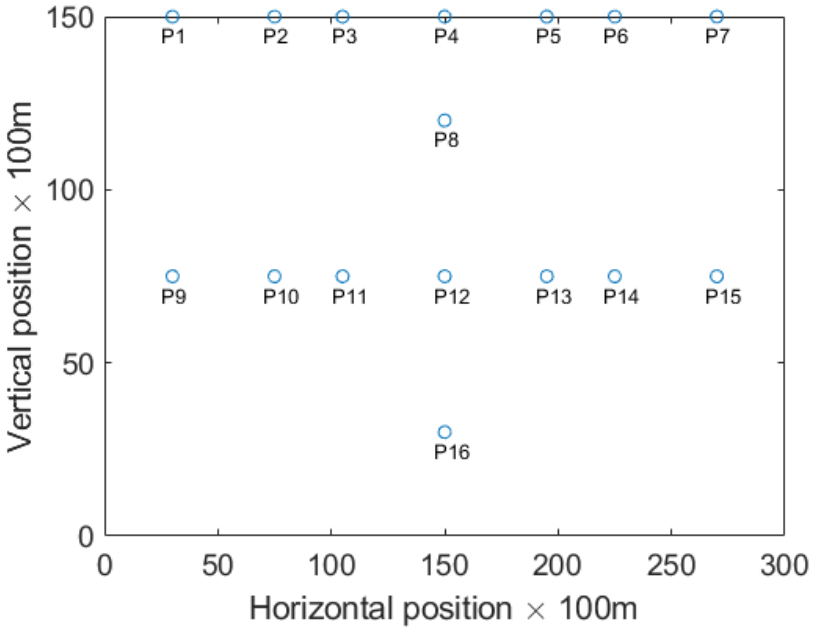

Figure 4.4: Positions of on-fault stations for the TPV5 benchmark.

4.1.1 Cohesive zone estimate

The upper bound estimate of the cohesive zone for the TPV5 benchmark is 465.6m for a Mode III crack based on formula (2.60), and 560m for a Mode II crack based on formula (2.59). If we had an estimate of typical rupture velocities in the problem, we could further refine the estimate by application of shrinking factors (2.62) for Mode III and (2.61) for Mode II crack.

We can gain a better picture of the cohesive zone size after the simulation is run. The local estimate of the cohesive zone from rupture time t_r, slip time t_s and rupture velocity can be calculated using formula (2.64). It is shown for the TPV5 benchmark (calculated with $\Delta h = 100$m) in Fig 4.5. It is not given at areas where the rupture speed is not defined, i.e. at the nucleation patch and the not-rupturing layers around the fault – estimate of the cohesive zone is assigned to be zero at these areas.

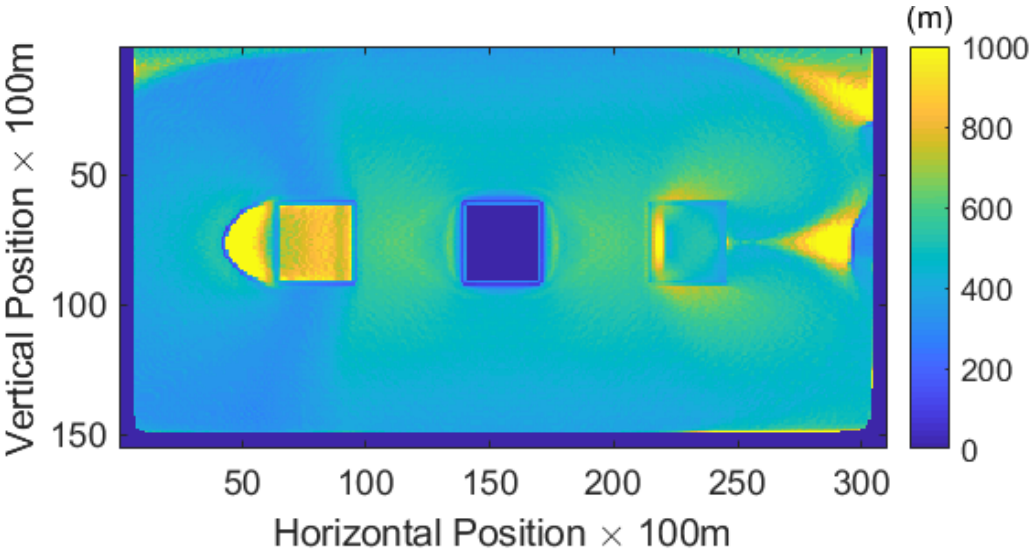

Figure 4.5: Cohesive zone estimate for the TPV5 benchmark.

How does this figure connect with pre simulation estimates (2.60) and (2.59) and the rupture velocity dependence (2.62) and (2.61)? The rupture velocity is highly variable through the fault plan., As can be seen in Fig 4.6, it spans the interval from 100m/s to supershear values above $v_s = 3464$m/s.

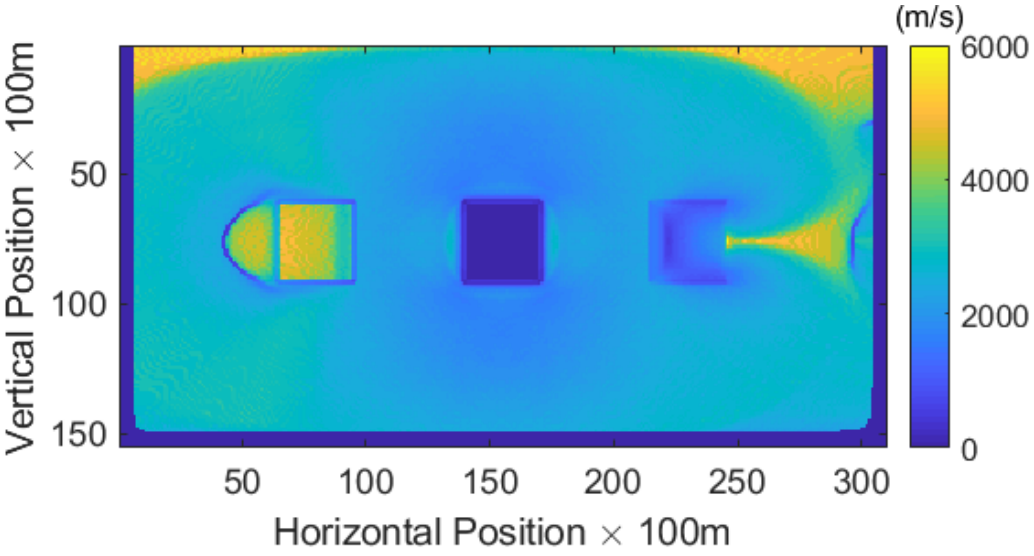

Figure 4.6: Rupture velocity in the TPV5 benchmark.

The situation is more complex then that described by approximated formulas (2.61) and (2.62). The fracture mode of the strike slip earthquake is a mix of mode III (propagation in the vertical direction) and mode II (propagation in the horizontal direction) fractures. Large areas of the fault also rupture at supershear speeds. This leads to a more variable relationship between the rupture velocity and the cohesive zone size as can be seen in Fig 4.7.

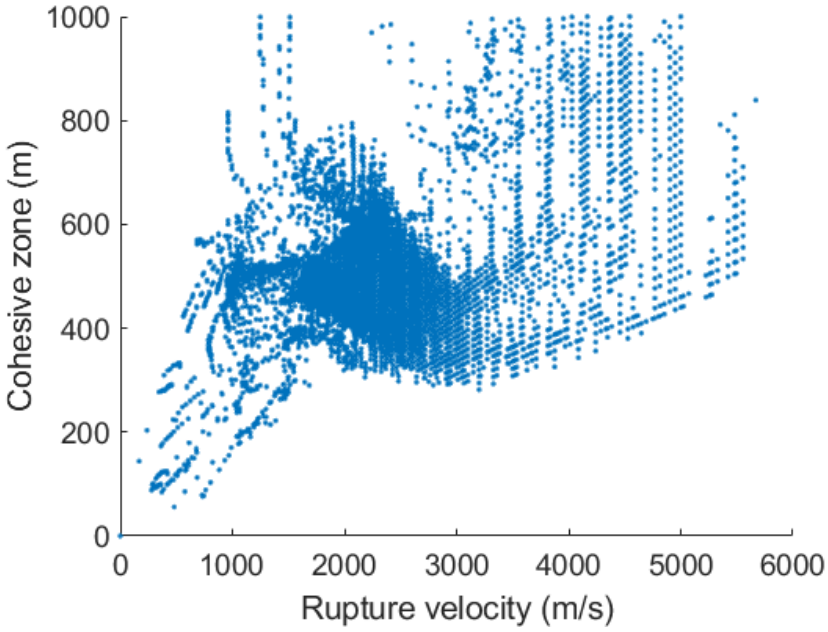

Figure 4.7: Rupture velocity vs cohesive zone size in the TPV5 benchmark.

The rupture propagates as a Mode III fracture in the vertical direction, allowing for a direct comparison with formula (2.62), see Fig 4.8, where local estimate is only larger then the theoretical (but also approximated) value by less then 10%. It is a good agreement, given the approximate nature of both estimates. Mode II crack model gives lower estimates of the cohesive zone size than Mode III crack, it is therefore the bounding value when trying to asses the accuracy.

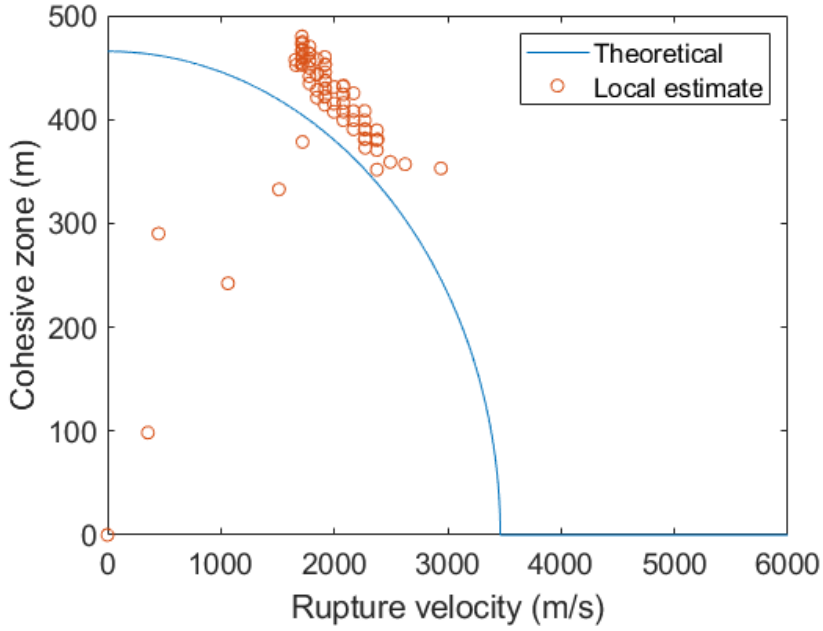

Figure 4.8: Dependence of the cohesive zone on rupture velocity in the TPV5 benchmark for the Mode III crack (blue line) and vertically propagating crack in the TPV5 (red circles).

FD codes typically require the cohesive zone resolution to be at least three points per cohesive zone, optimal value is five [Day et al., 2005]. Discretization with $\Delta h = 100$m will be at the border of this interval with minimum value of the resolution of 3.5 points per cohesive zone, while $\Delta h = 50$m should give very accurate results (resolution of 7 points per cohesive zone).

4.1.2 Convergence

The development of the accuracy of the solution with Δh in the TPV5 benchmark was studied by assesing errors in two important kinematic rupture properties – rupture time and slip. The normalized root mean square difference from the most accurate solution (FD3D_TSN with $\Delta h = 50$m) was calculated for the original thin zone zone version and the improved traction at split node (TSN) version solutions calculated for different discretizations. The results are in Fig 4.9 and 4.10 for rupture time and slip, respectively.

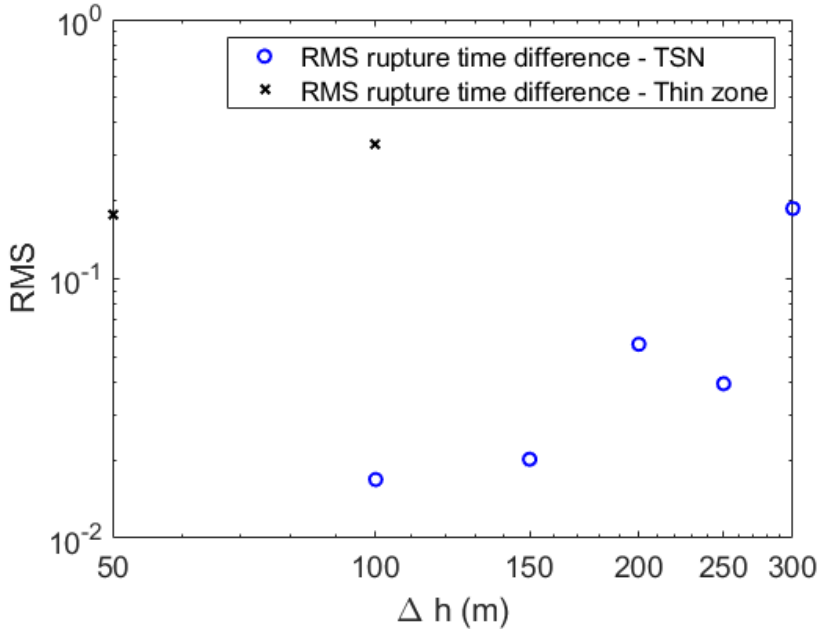

Figure 4.9: Normalized root mean square difference of the rupture times in the TPV5 benchmark. Results of FD3D_TSN version for $\Delta h = 50$m are taken as a reference solution with RMS equal to zero. Blue circles are results of FD3D_TSN, black crosses are results of the thin zone version.

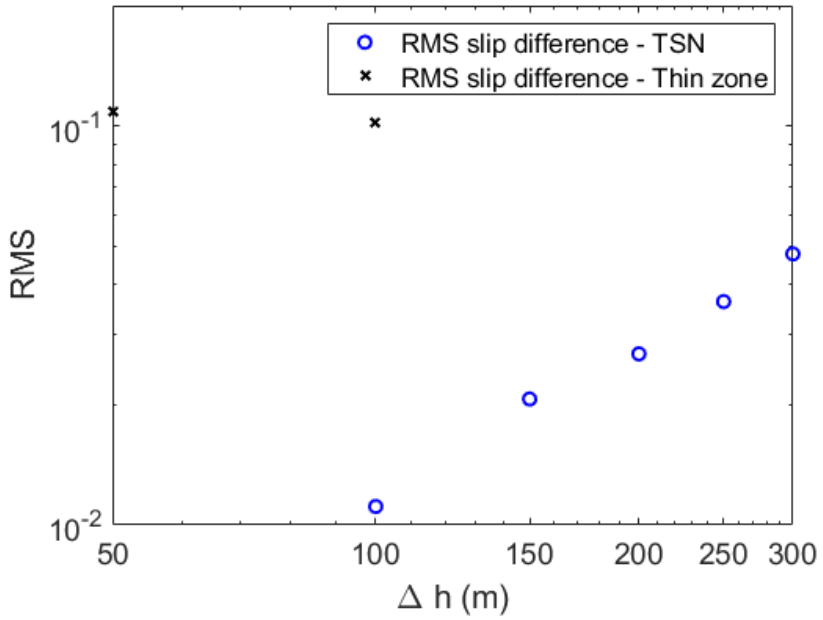

Figure 4.10: Same as in Fig 4.9, but for the slip distribution.

The thin zone version did not work with higher discretization steps above 200m, where the rupture did even not propagate outside of the nucleation zone. Moreover, its results do not imply convergence of the solution for presented Δh, finer discretization would be required.

Results of FD3D_TSN are in a good agreement with our expectations based on the cohesive zone resolution. The difference between results calculated with $\Delta h = 100$m and those with $\Delta h = 50$m is only about one percent. Such a difference from the true solution would be acceptable.

4.1.3 Results of the thin zone approach

The performance of the original thin fault version of FD3D in the TPV5 benchmark was tested first. Presented are two major benchmark outputs – rupture time contour plot in Fig 4.15 and sliprates and tractions in on-fault stations in Fig 4.12 and 4.13. The results were calculated using spatial discretization parameter set to $\Delta h = 50$m. All graphs are overlayed over the reference results of the FaultMod code.

The results in the previous section imply that the solution propably did not converge even for the generous discretization withresolution of 7 points per cohesive zone. Typical symptom of insufficient resolution is decreased rupture velocity/increased rupture time. This can be observed in all figures, when comparing with the reference solution – the rupture si much slower, especially around the prestress heterogeneities.

Shapes of the rupture time contours are very similar between both solvers, when thegeneral decrease of the rupture velocity is neglected. The contours at the right hand side of the fault, where the difference in rupture time is 1s, are very close to each other.

Major observable difference between solvers in slip rate and traction plots (Fig 4.12 and 4.13) is again in the rupture times, but significant differences in

maximum slip rates are also observed, such as at points P4, P7, P16. The second peak in the slip rate at points that are not directly at the free surface (P8-P16) is a secondary rupture reflected form the free surface.

The graphs of the traction measured closer to the border of the fault plane (P1, P2, P9, P14) show sudden increase above the dynamic traction value at later times in the FD3D solution. This is caused by the performance of the original absorbing boundary conditions, which reflect part of the radiated energy back to the fault. This would be observed at all parts of the fault for longer time intervals. The increase of the traction above the dynamic friction does not cause further slip because reaching the static value again after the slip rate decreased to zero was required as a regularization.

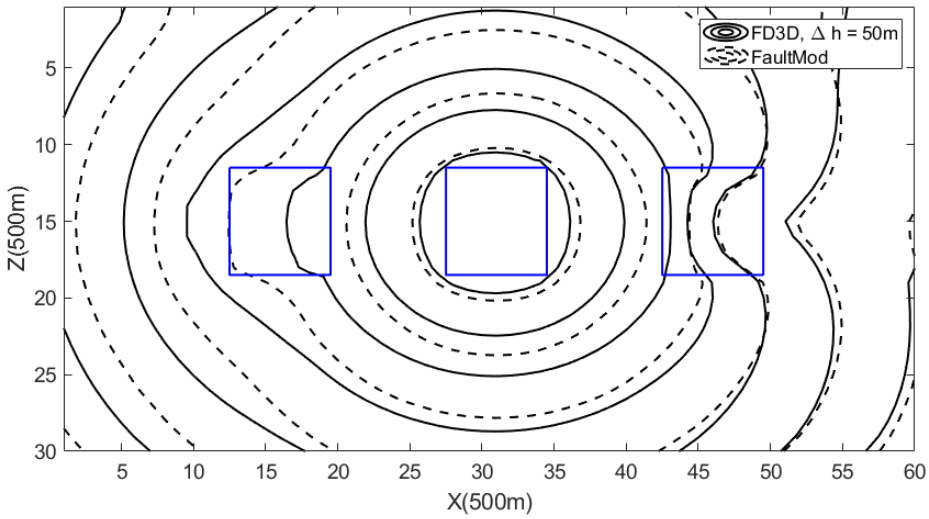

Figure 4.11: Rupture time contour plot comparison for thin zone FD3D, with $\Delta h = 50$m (solid line) and FaultMod (dashed line) in the TPV5 benchmark. Lines display rupture front position at time 1s, 2s,... . Blue squares mark positions of the prestress heterogenities (Fig 4.3).

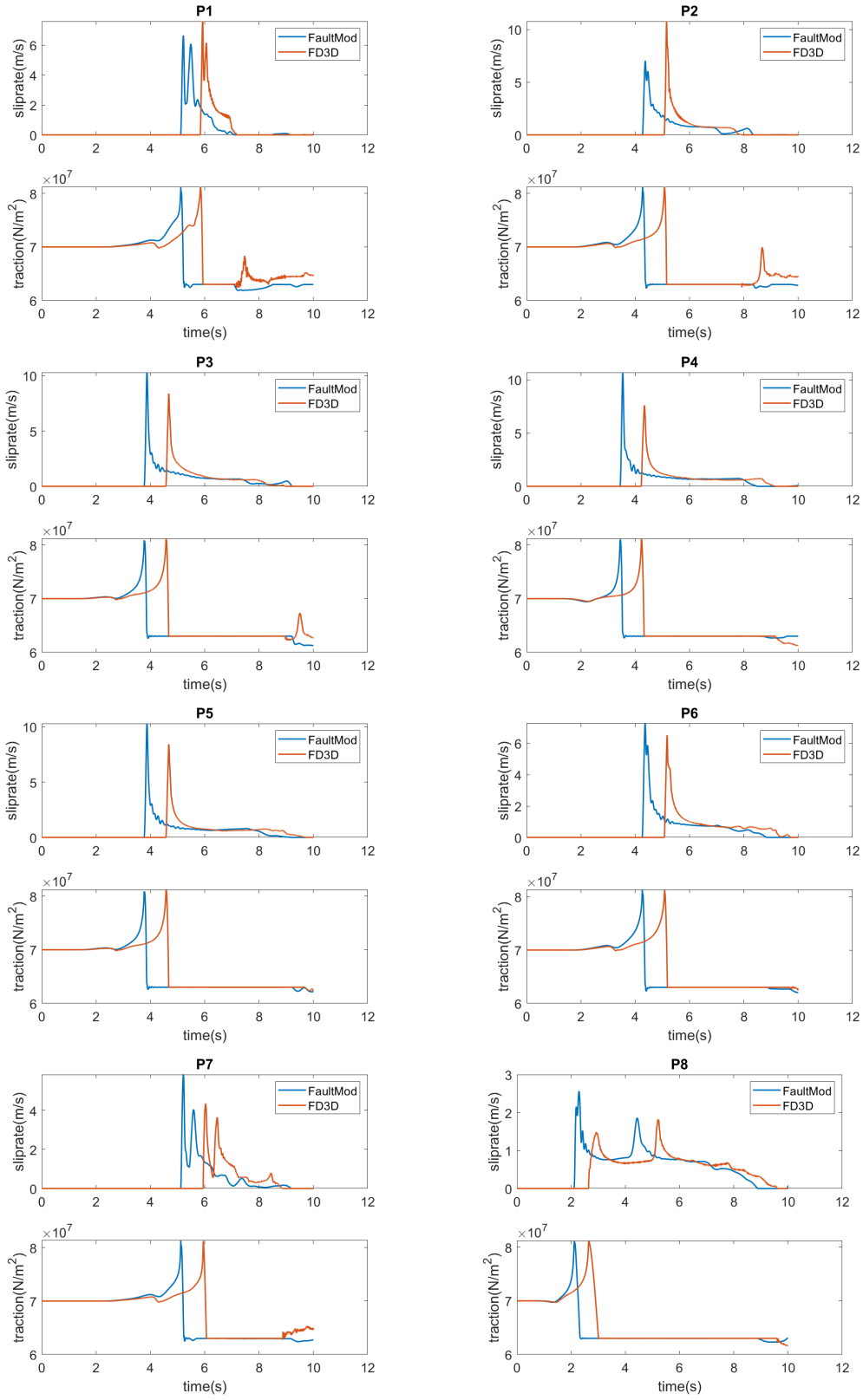

Figure 4.12: Sliprates and tractions for points P1–P8 (positions are in Fig 4.4) in the TPV5 benchmark. Results of the thin zone FD3D and the reference results of the FaultMod code are denoted by red and blue lines, respectively.

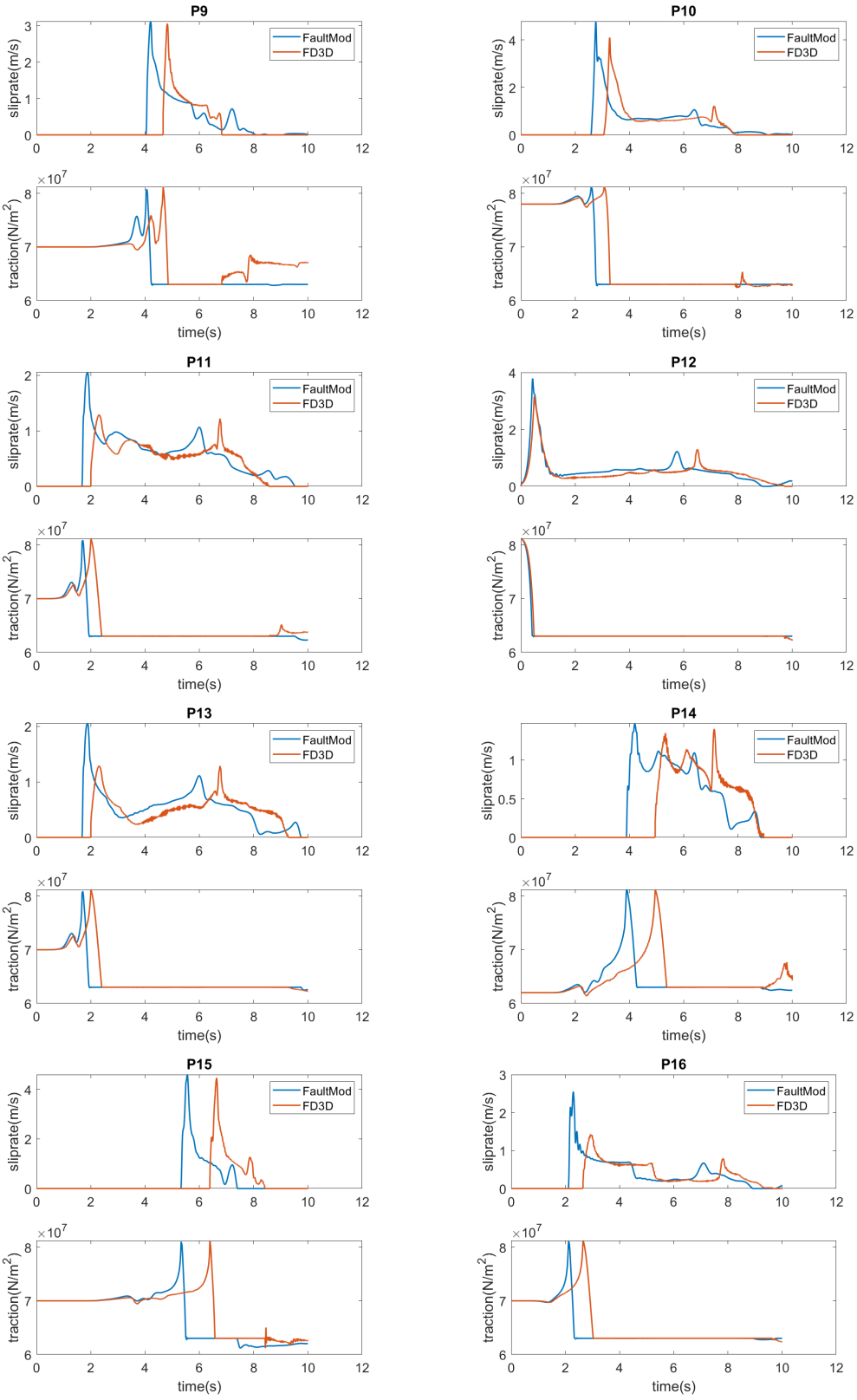

Figure 4.13: Same as Fig 4.12 but for points P9–P16.

4.1.4 Results of the traction at split node approach

Tests of the new FD3D_TSN with TSN fault boundary implementation and perfectly matched layer absorbing conditions, for two spatial discretizations $\Delta h =$ 100m (Fig 4.14, 4.16, 4.17) and $\Delta h =$ 50m (Fig 4.15, 4.18, 4.19) are shown in this section.

Differences between results of coarser and finer discretizations are minimal, as can be expected from the results in section about convergence (Section 4.1.2), suggesting (but not proving) convergence of the solution. Good agreement with the results of the FaultMod code is also observed.

Error in rupture velocity depends on the direction, which can be seen especially for coarser discretization in Fig 4.14. This is an effect caused by the staggered position of the velocity and stress components in the FD grid and its impact on the discretization of the nucleation zone. The horizontal traction component σ_{12} is positioned on the left side of every grid cell. The area with increased prestress is therefore larger to the left of the hypocentre (position at the centre of the fault). Connection between the discretization of the nucleation zone and rupture velocity was studied for example in Galis et al. [2014]. The effect practically disappears for the finer discretization (Fig 4.15).

There are small differences in the shape of the slip rate time series (especially in the shape of the rupture reflected from the free surface) between FD3D_TSN and FaultMod, that do not dissapear for finer discretization. This can be explained by the artificial damping used to supress high frequency oscillations, that is used in both codes but in different forms. Agreement between both codes in slip rate shapes is otherwise very good, including maximum slip rates.

The traction drops below the dynamic friction value during the simulation. Concrete value of the minimum traction is influenced by many small factors that are not set in the benchmark and therefore differ between presented methods. The size of the non-rupturing layer around fault (distance between fault and absrbing boundary condition in the horizontal and vertical directions) is one of them. Variance in this value can be therefore expected and has minimal impact on the overall accuracy.

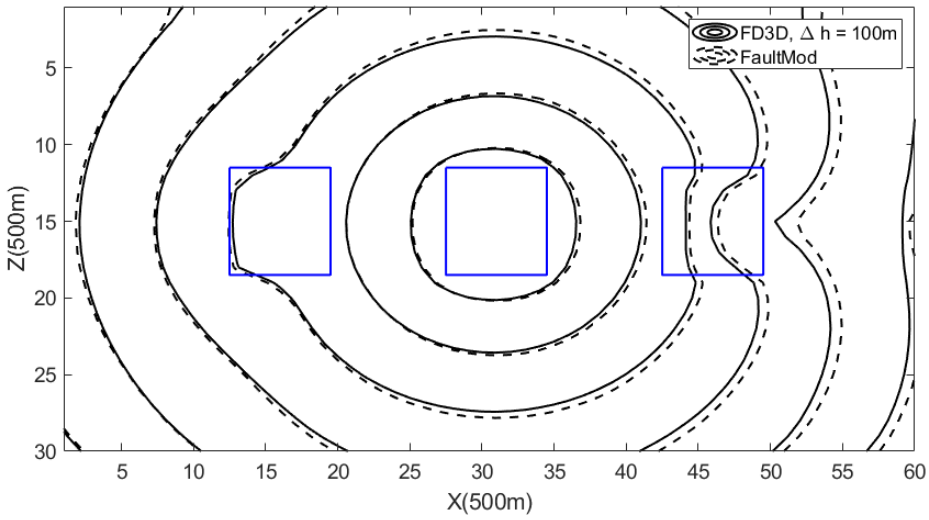

Figure 4.14: Rupture time contour plot for FD3D_TSN, with $\Delta h = 100$m (solid line) and FaultMod (dashed line). Lines display rupture front position at time 1s, 2s,... . Blue squares mark positions of the prestress heterogenities.

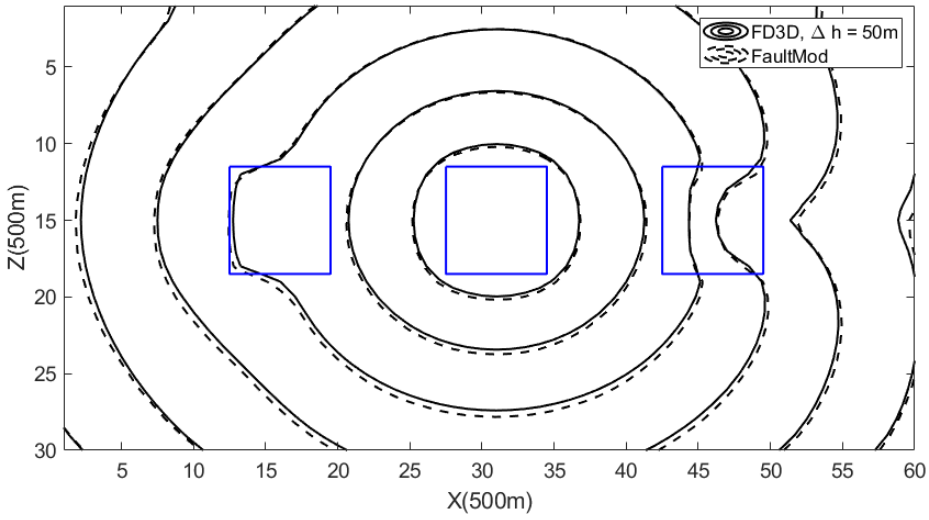

Figure 4.15: Same as Fig 4.14 but using discretization step $\Delta h = 50$m.

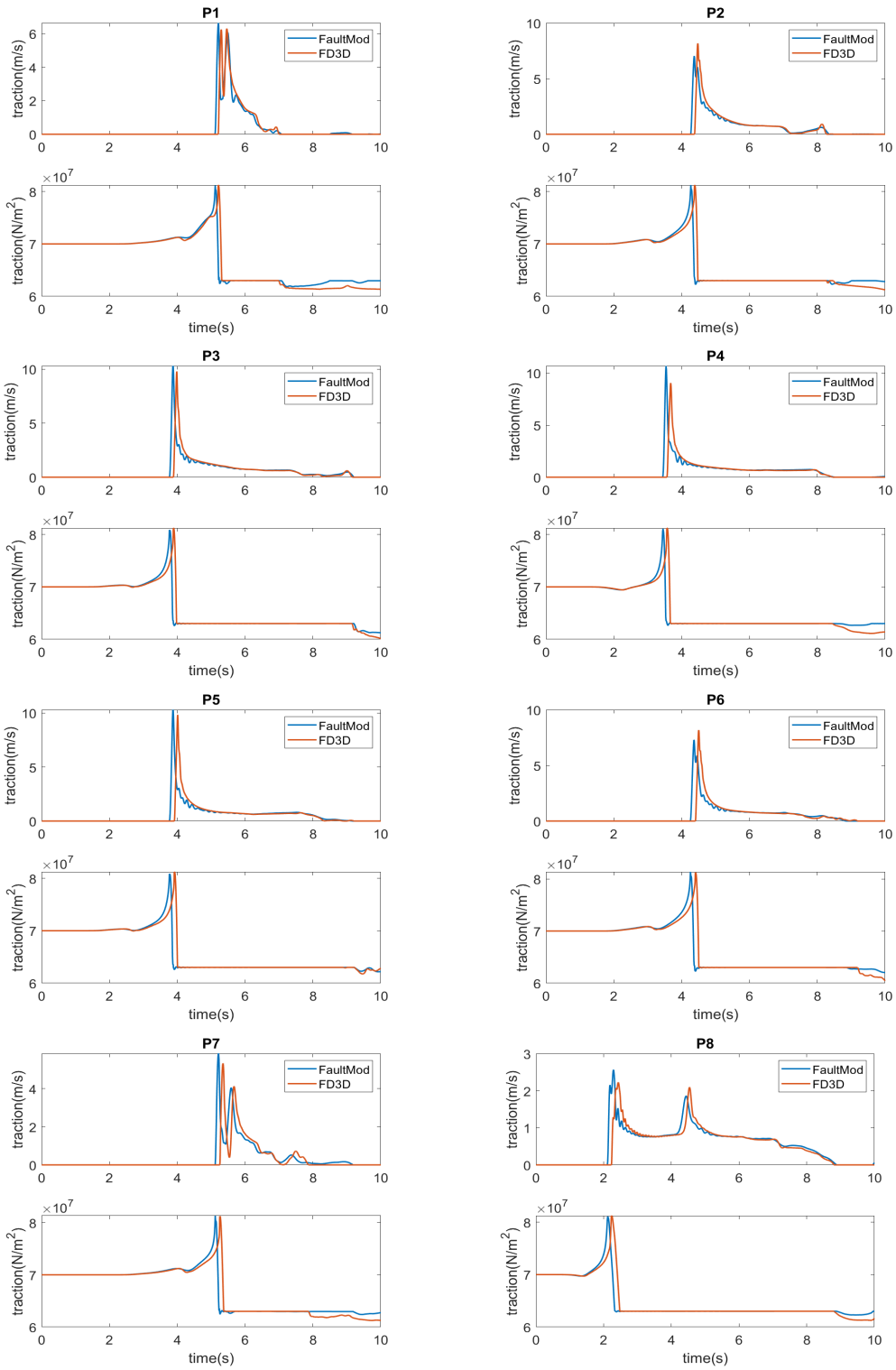

Figure 4.16: Sliprates and tractions for points P1–P8 (positions are in Fig 4.4) in the TPV5 benchmark. Results of the FD3D_TSN code using $\Delta h = 100$m and the reference results of the FaultMod code are denoted by red lines and blue lines, respectively.

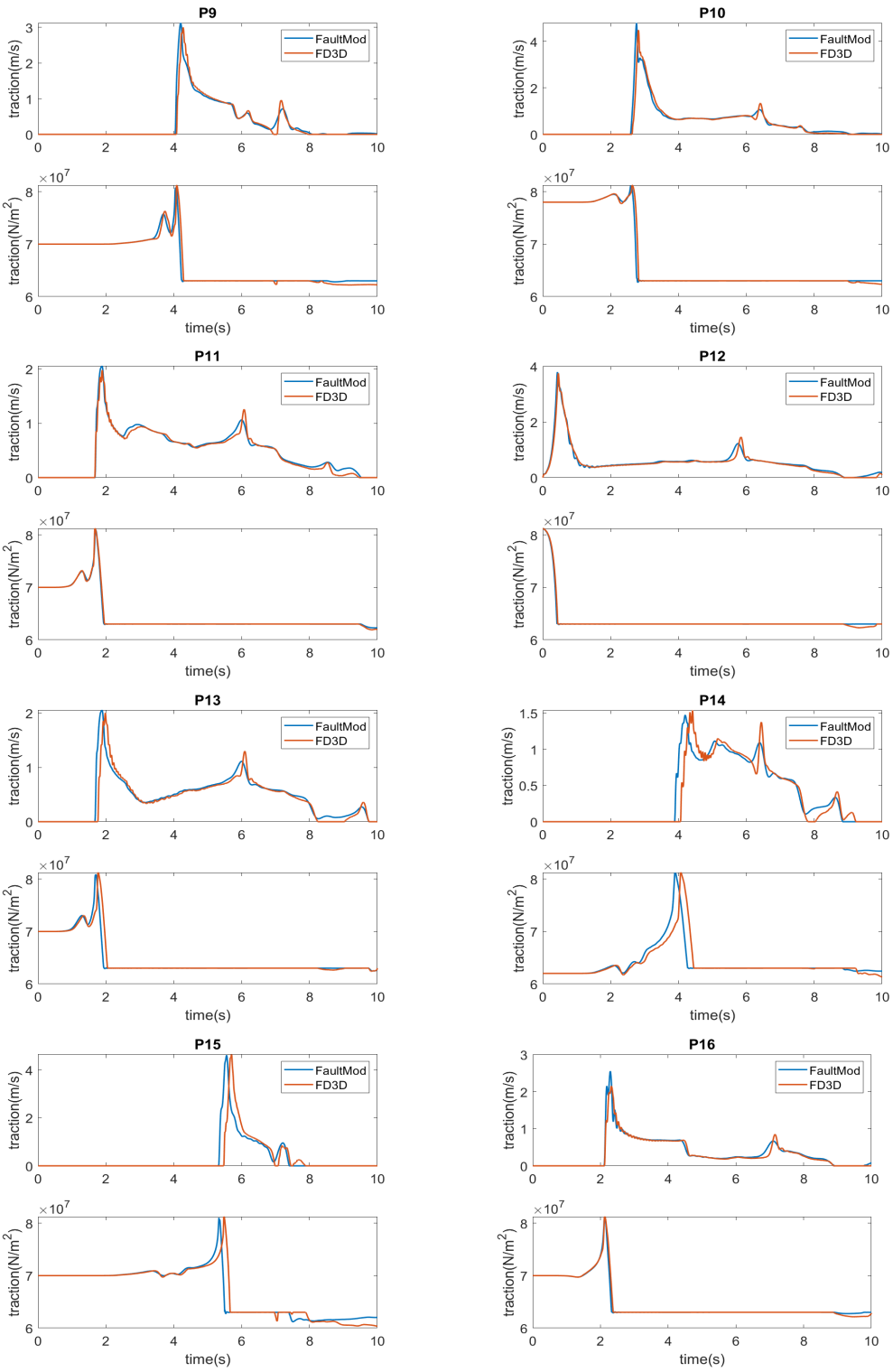

Figure 4.17: Same as Fig 4.16 but for the points P9–P16.

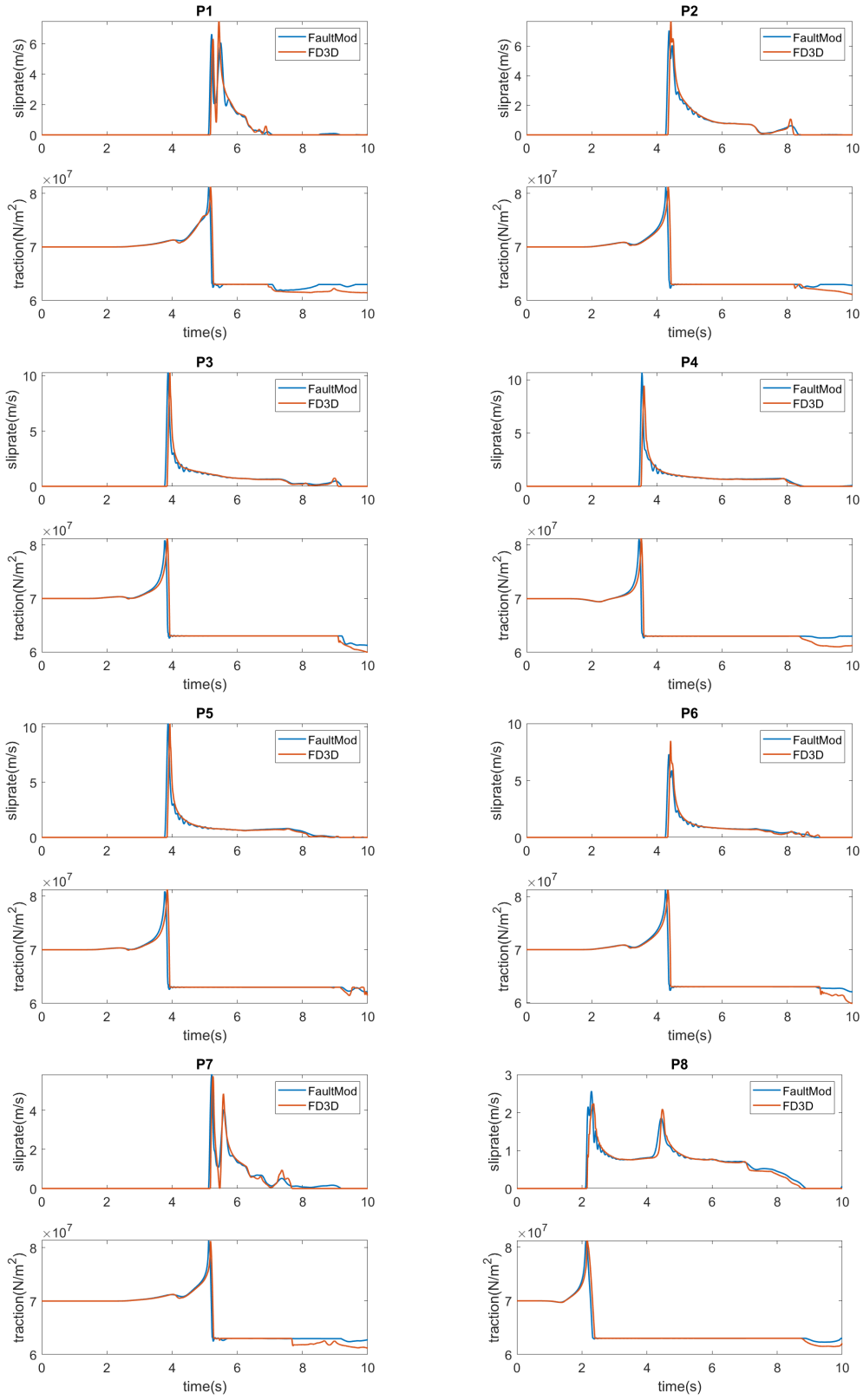

Figure 4.18: Sliprates and tractions for points P1–P8 (positions are in Fig 4.4) in the TPV5 benchmark. Results of the FD3D_TSN code using $\Delta h = 50$m and the reference results of the FaultMod code are denoted by red lines and blue lines, respectively.

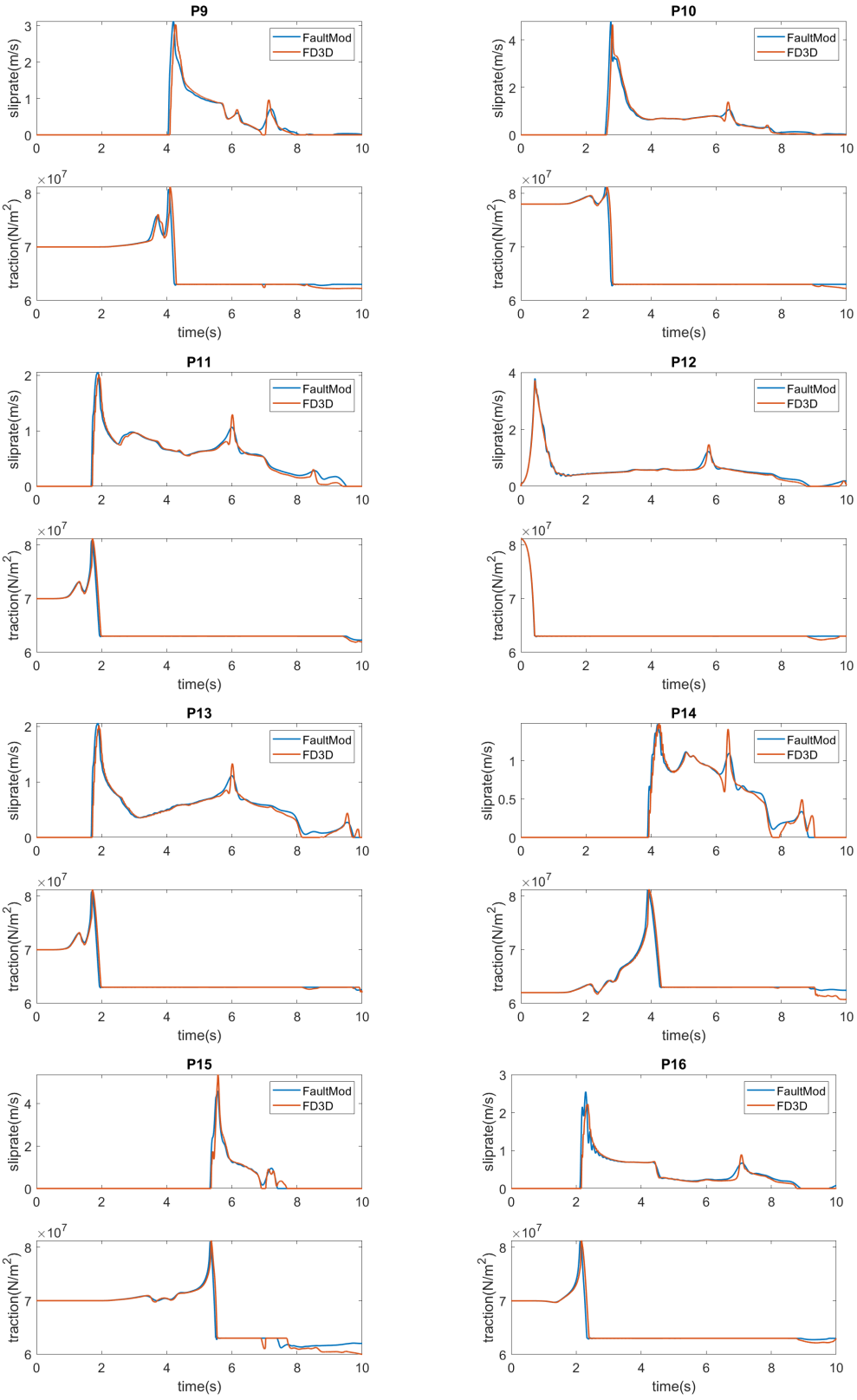

Figure 4.19: Same as Fig 4.18 but for the points P9–P16.

4.2 TPV104 benchmark

The TPV104 benchmark is similar to the TPV5 benchmark, but the fast velocity weakening friction law is used. Material in the domain has the same properties as in TPV5 (Table 4.1). The fault consists of a velocity weakening (VW) area of size 30×15km, surounded by a transition layer and a velocity strenghtening layer (VS). The rupture is again a strike-slip. Parameters of the fast velocity weakening friction law (2.42) in the VW area are shown in Table 4.4. Only values of parameters a and $\dot{s}_w$ are different in the VS layer then in the VW area, the values are shown in Table 4.5.

f_0	$\dot{s}_0$	$a^{(VW)}$	b	L	f_w	$\dot{s}_w^{(VW)}$
0.6	10^{-6}m/s	0.01	0.014	0.4m	0.2	0.1m/s

Table 4.4: Friction parameters for the TPV104 benchmark – the VW zone.

$a^{(VS)}$	$\dot{s}_w^{(VS)}$
0.02	1m/s

Table 4.5: Friction parameters for the TPV104 benchmark – the VS zone.

The transition layer between the VW and VS zones is $w = 3$km wide. Both parameters $a^{(T)}$ and $\dot{s}_w^{(T)}$ smoothly increase from the VW zone to the VS zone as

$$\begin{aligned} a^{(T)}(\Delta x, \Delta z) &= a^{(VW)} + (a^{(VS)} - a^{(VW)}) \times (1 - B(\Delta x, w)B(\Delta z, w)) \\ \dot{s}_w^{(T)}(\Delta x, \Delta z) &= \dot{s}_w^{(VW)} + (\dot{s}_w^{(VS)} - \dot{s}_w^{(VW)}) \times (1 - B(\Delta x, w)B(\Delta z, w)) \\ B(\Delta, w) &= \frac{1}{2}\left[1 + \tanh\left(\frac{w}{\Delta - w} + \frac{w}{\Delta}\right)\right], \end{aligned} \tag{4.1}$$

where Δx and Δz are distances from the VW zone in the x and z direction, respectively. The shape of the $B(\Delta, w)$ function is shown in Fig 4.20.

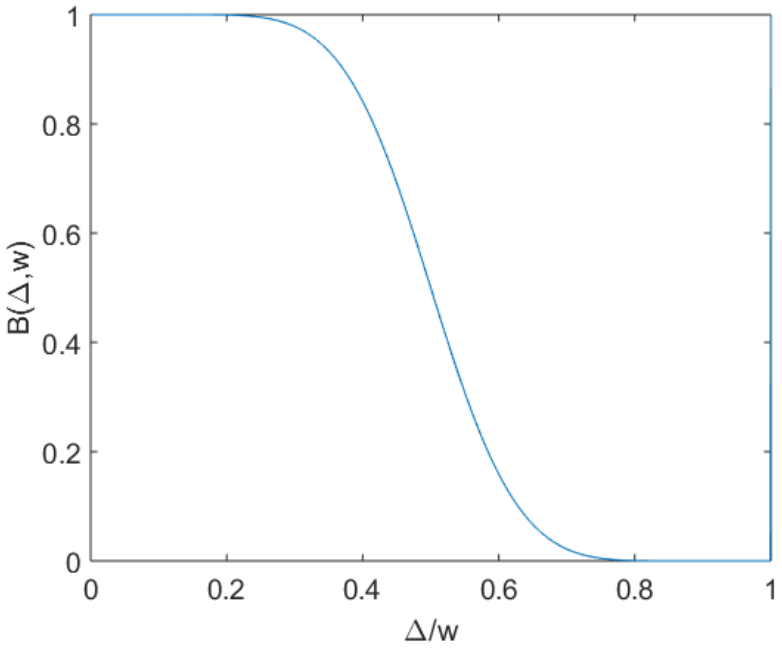

Figure 4.20: $B(\Delta, w)$ function through the transition zone.

Initial values of the field dynamic parameters are shown in Table 4.6.

$\dot{s}^{(INI)}$	σ_n	$T_0^{(INI)}$
10^{-16}m/s	120MPa	40MPa

Table 4.6: Friction parameters for TPV104 benchmark – Initial values

Initial value of the state variable is set to accomodate these initial values from (2.42):

$$\psi^{(INI)} = a\log\left[\frac{2\dot{s}_0}{\dot{s}^{(INI)}}\sinh\left(\frac{T_0}{a\sigma_n}\right)\right] \tag{4.2}$$

Nucleation is handled by imposing the following time and space dependent increase of the prestress in a round patch at the centre of the fault – $(x_1^c, x_3^c) = (7, 5km, 15km)$. The maximum increase is $\Delta T^0 = 45$MPa. The prestress is set to increase as

$$\begin{aligned} T^0(x_1, x_3, t) &= T_0^{(INI)} + \Delta T^0\left[C\left(\sqrt{(x_1 - x_1^c)^2 + (x_3 - x_3^c)^2}\right) D(t)\right] \\ C(r) &= \begin{cases} exp\left(\frac{r^2}{r^2 - r_0^2}\right) & : r < r_0 \\ 0 & : r \geq r_0 \end{cases} \\ D(t) &= \begin{cases} exp\left(\frac{(t-t_0)^2}{t(t-2t_0)}\right) & : t < t_0 \\ 1 & : t \geq t_0, \end{cases} \end{aligned} \tag{4.3}$$

where parameters $t_0 = 1$s and $r_0 = 3$km define the time of the maximum shear stress increase and the patch radius, respectively.

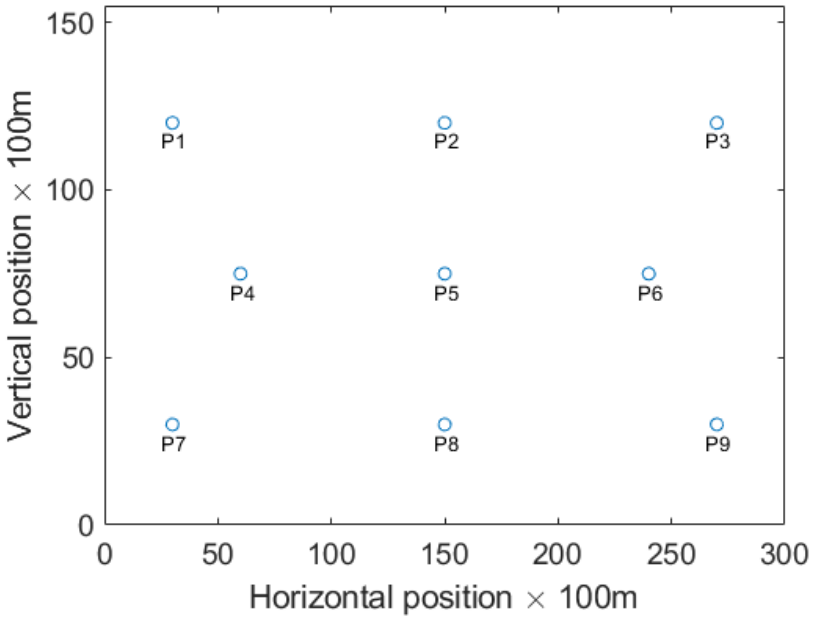

Figure 4.21: Positions of the on-fault stations for the TPV104 benchmark.

4.2.1 Cohesive zone estimation

Cohesive zone size for the TPV104 benchmark estimated using formula (2.65) is shown in Fig 4.22. Oscillations in the rupture velocity probably cause oscillation in the calculated values. Typical size of the cohesive zone through the fault is between 250m 300m, with large variability around nuclation zone in the centre of the fault. Cohesive zone resolution with ($\Delta h = 100$m) is again at the border of acceptable values of 2.5 - 3 points per cohesive zone. Discretizations with ($\Delta h = 50$m) should offer sufficient resolution of at least 5 points per cohesive zone in most of the fault.

Exception to that is near free surface, where the size of the cohesive zone drops to values around 100m. The rupture propagation through this area should show signs of the insufficient cohesive zone resolution. This perhaps explains the variability among different solvers in Fig 4.2, when looking at the secondary slip pulse (reflected from the free surface).

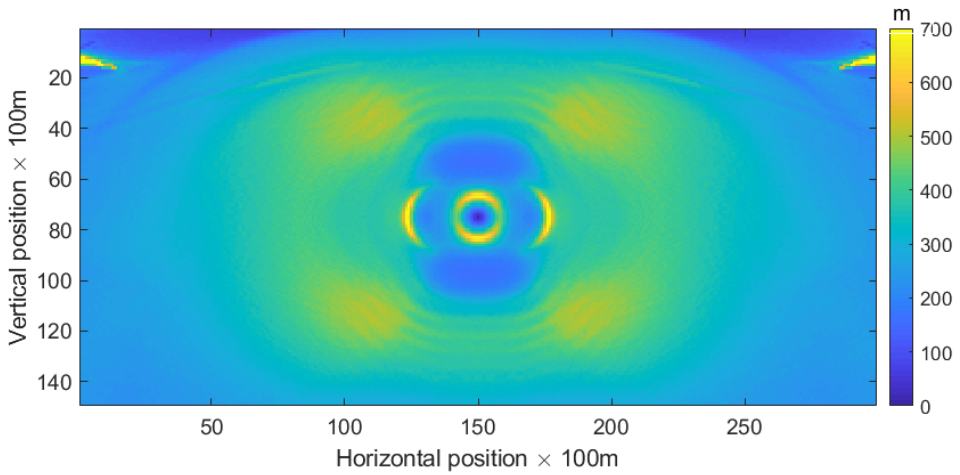

Figure 4.22: Cohesive zone size in the TPV104 benchmark estimated using formula (2.65).

4.2.2 Results

Results of the FD3D_TSN in the TPV104 benchmark are presented in this section. The convergence of average RMS difference of rupture time and slip was again tested and are shown in Fig 4.23 and 4.24, respectively. Difference between the results of coarser discretization with $\Delta h = 100$m and the finer one with $\Delta h = 50$m suggesting proximity to the converged solution.

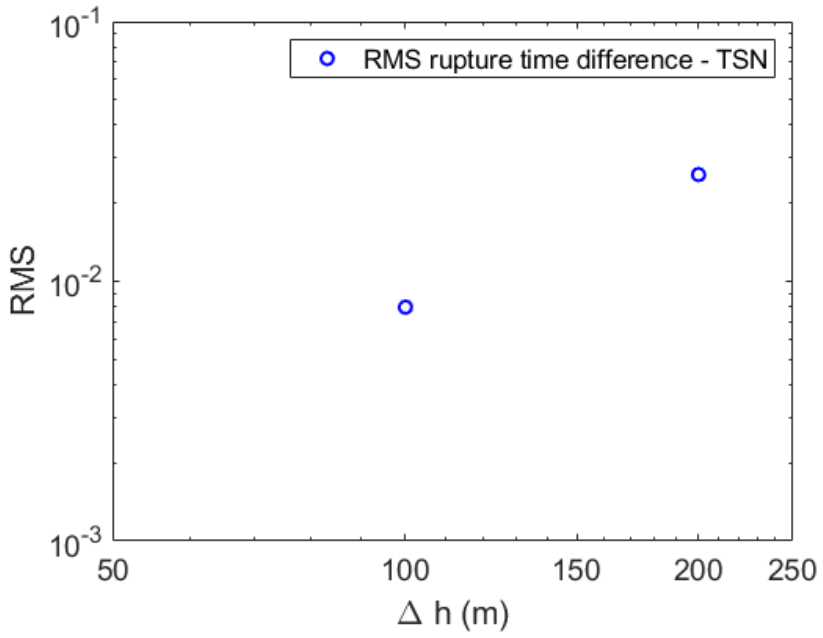

Figure 4.23: Normalized root mean square difference of the rupture times in the TPV104 benchmark. Results of FD3D_TSN version for $\Delta h = 50$m are taken as a reference solution with RMS equal to zero. Blue circles are results of the TSN version for different discretizations.

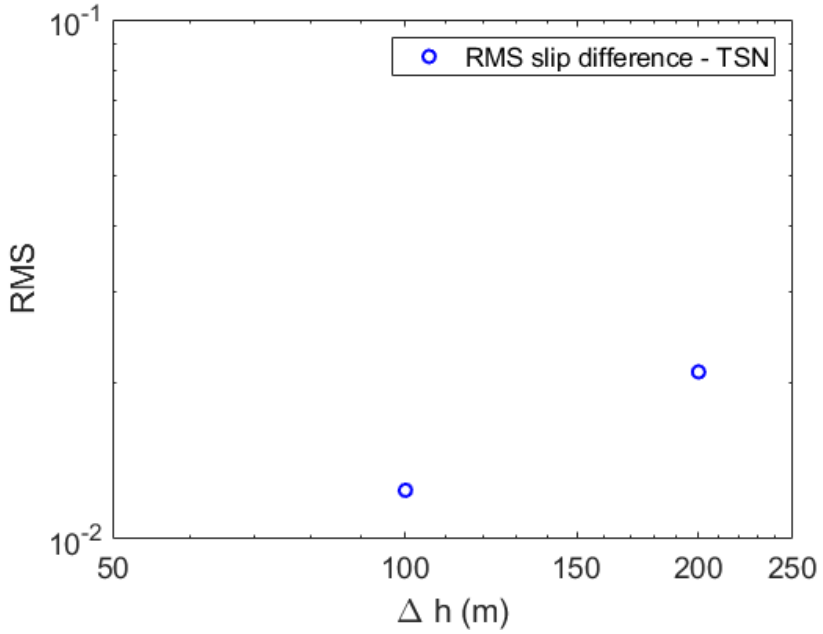

Figure 4.24: The same as Fig 4.23, but for the slip.

Benchmark results (rupture time contours, slip rates, tractions and state variables) for two finest resolutions, those with spatial discretization $\Delta h = 100$m (Fig 4.25, 4.27, 4.28) and $\Delta h = 50$m (Fig 4.26, 4.29, 4.30) are discussed next.

Rupture time contour plots for both discretizations (Fig 4.25 and 4.26) show noticable difference in the rupture velocity between FD3D_TSN and FaultMod results, with rupture in the FD3D_TSN solution being faster. The difference is comparable with differences between other codes (Fig 4.2). It can be caused for example by the implementation of the nucleation procedure. The assymetry of the rupture time contours is again observable, with the rupture on the left hand side of the fault being quicker. This is again caused by the staggered position of the components in the FD grid causing assymetries in the nucleation zone shape. The effect is again minimized for the finer grid.

Shapes of slip rates are practically identical. The most visible discrepancy is in the shape of the rupture reflected from the free surface (second peak), especially in their maximum slip rates in points P5 and P8 (Fig 4.28).

The difference in behaviour between the slip weakening and fast velocity weakening friction can be observed throughout the plots with traction time series in this section. With the slip weakening friction in the TPV5 benchmark the traction dropped to a dynamic value and possibly then further decreased below it. Here the traction starts to grow near the end of every slip pulse, due to healing (increase of the state variable). The development of the traction at point P8 is a good example of this.

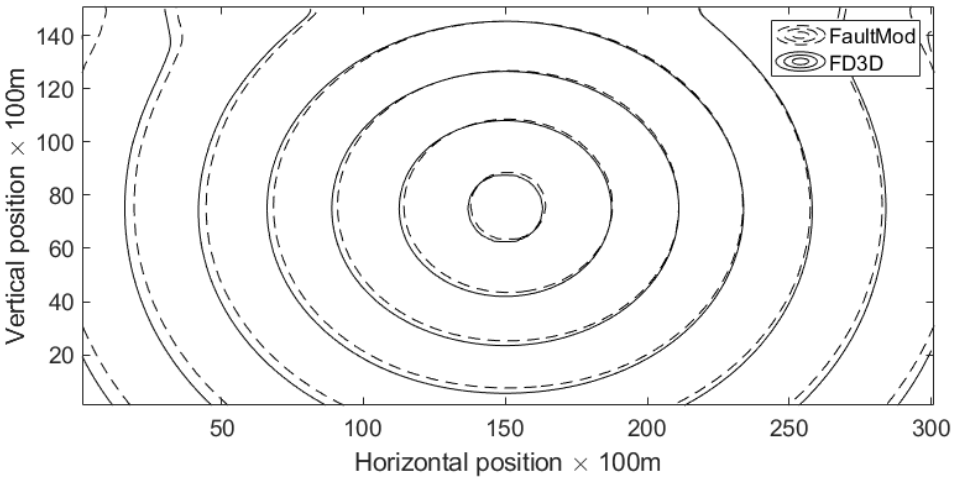

Figure 4.25: Rupture time contour plot for TPV104. Dashed line is for the solution of FaultMod, full line is the solution of FD3D_TSN, with $\Delta h = 100$m.

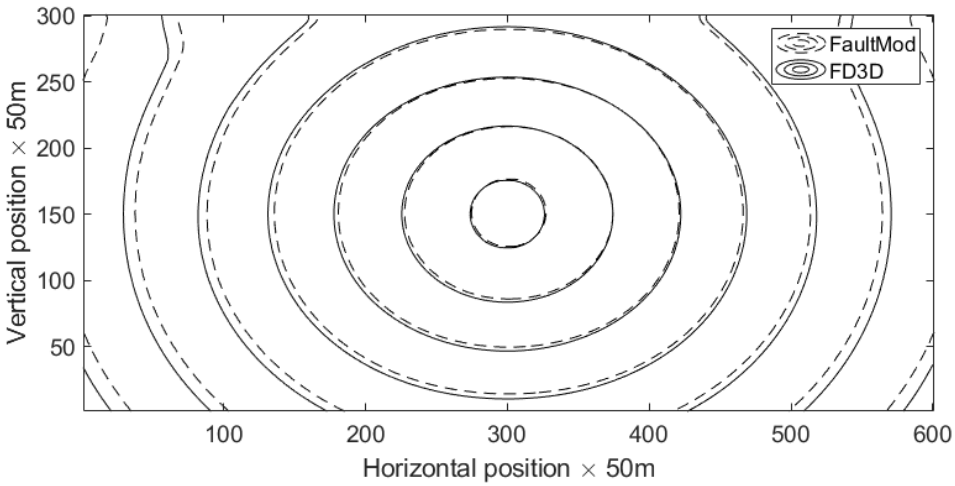

Figure 4.26: Same as Fig 4.25, but for $\Delta h = 50$m.

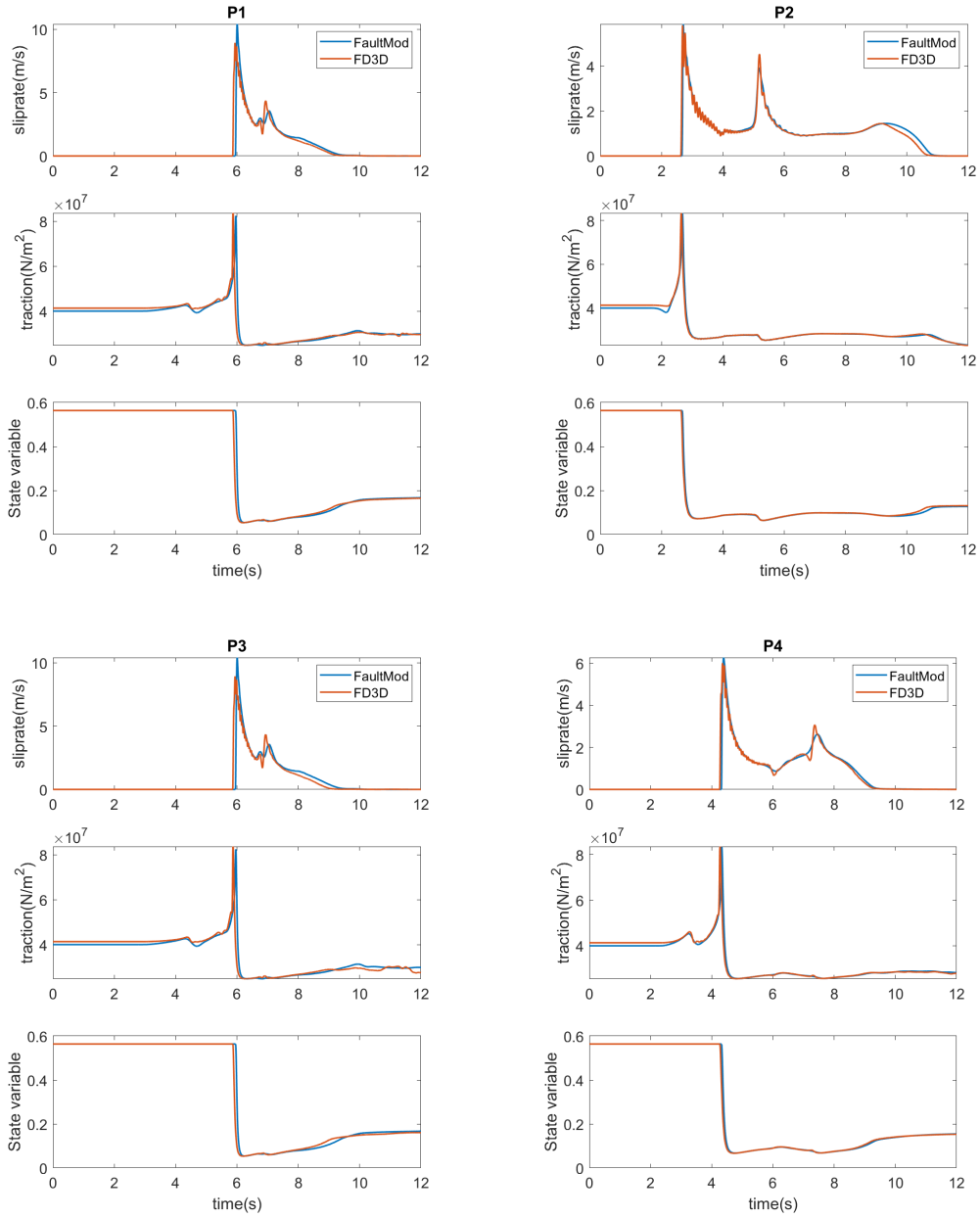

Figure 4.27: Sliprates and tractions for points P1–P4 (positions are in Fig 4.4) in the TPV104 benchmark. Results of the FD3D_TSN code using $\Delta h = 100$m and the reference results of the FaultMod code are denoted by red lines and blue lines, respectively.

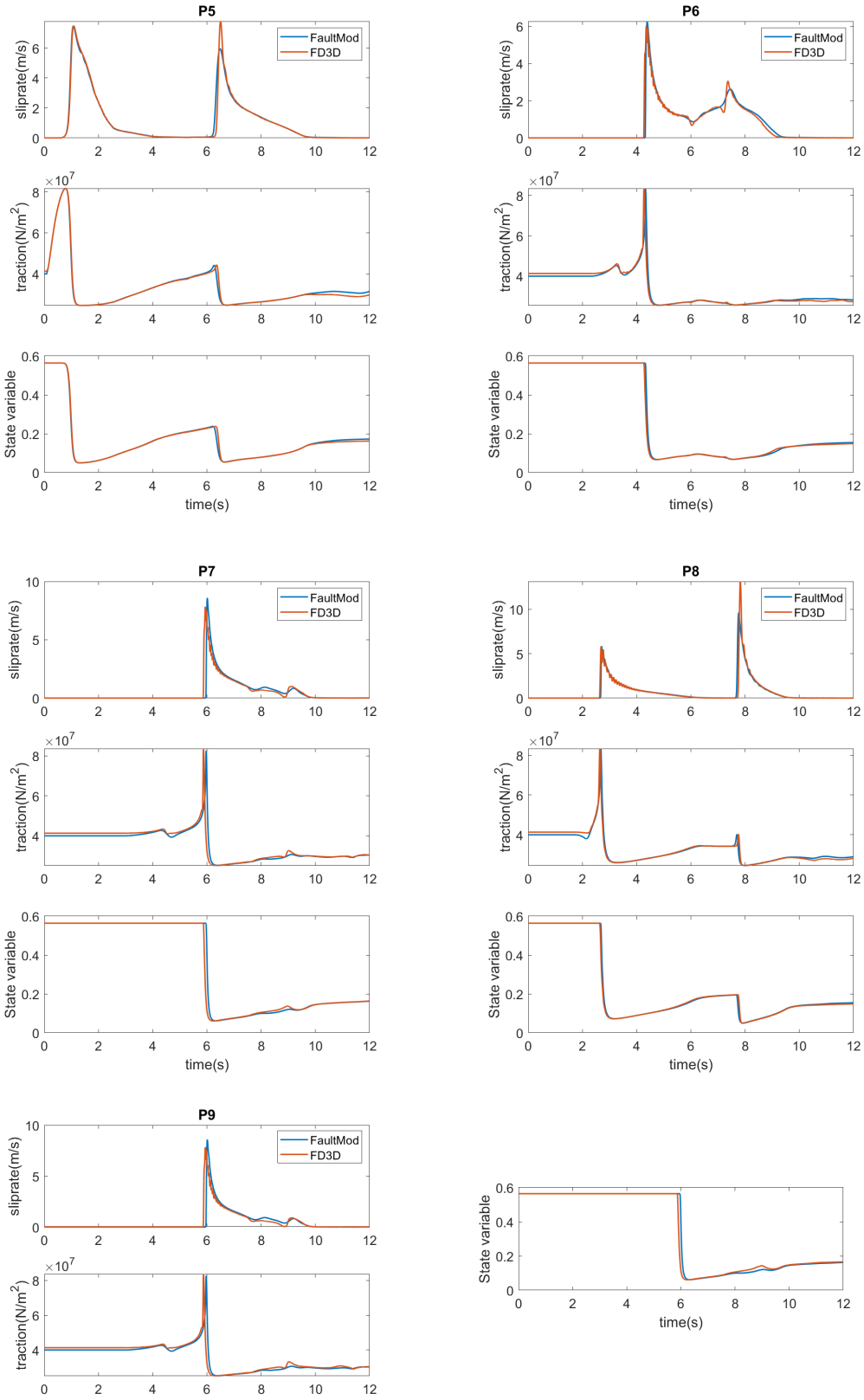

Figure 4.28: The same as Fig 4.27, but for the points P5–P9.

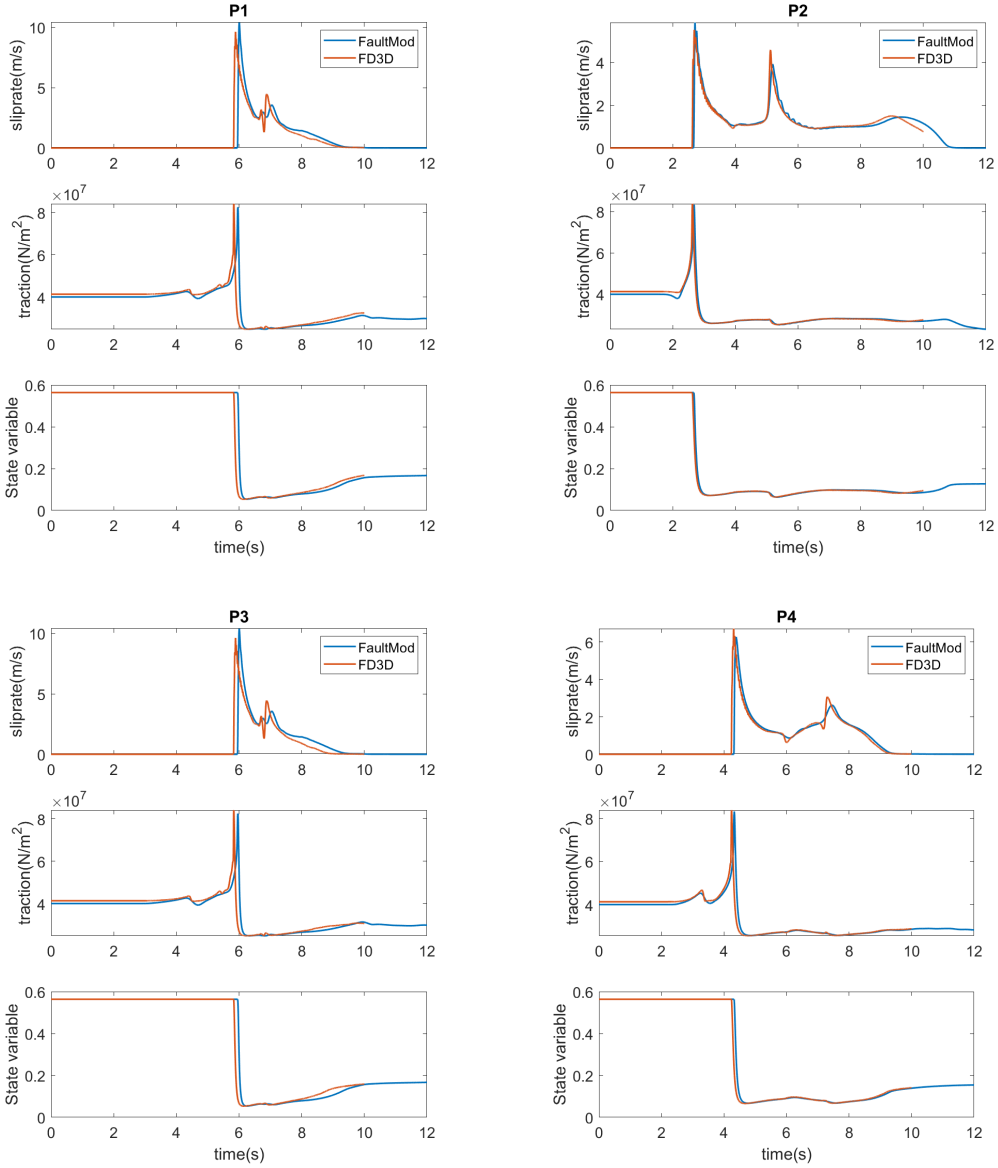

Figure 4.29: Sliprates and tractions for points P1–P4 (positions are in Fig 4.4) in the TPV104 benchmark. Results of the FD3D_TSN code using $\Delta h = 50$m and the reference results of the FaultMod code are denoted by red lines and blue lines, respectively.

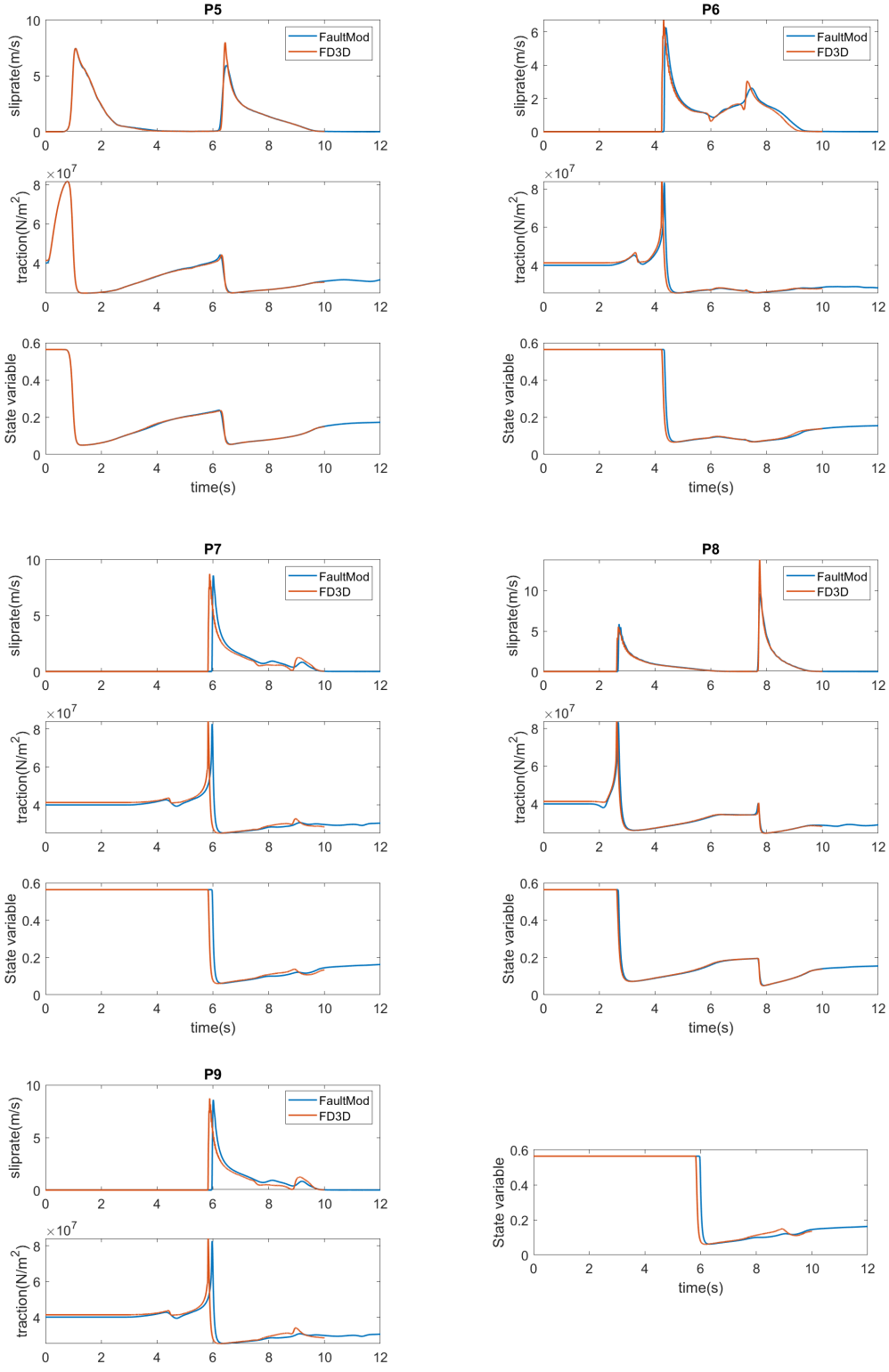

Figure 4.30: Same as Fig 4.29, but for the points P5–P9.

Conclusions

Dynamic simulation of the spontaneous rupture propagation is a numerically difficult problem. The problem of the seismic wave propagation in the izotropic continuum modelled by solving the elastodynamic equation is supplemented by the introduction of the fault boundary condition with nonlinear relation between velocity and stress. Main goal of this Thesis was the development of an efficient code solving the rupture propagation problem by a finite difference method. Motivation for the development was the potential further use of the code as a forward solver in the dynamic inversion of specific earthquakes [Gallovic et al., 2019]. This requires efficient and fast code, due to the necessity of running a large number of forward simulations, caused by nonlinear relationship between dynamic parameters (governing the rupture propagation) and seismograms.

The code is based on the original FD3D code by Madariaga et al. [1998]. Calculation speed of the original code was acceptable, especially with the parallelization for GPU using OpenACC directives, but the thin zone implementation of the fault boundary condition did not performe well when compared with methods used in other codes [Dalguer and Day, 2006]. Two major changes to the original code were made – implementation of the different fault boundary condition and the absorbing bundary condition.

Description of the finite difference numerical method for the elastodynamic equation and the implementation of various boundary conditions constitute the main part of this Thesis. Staggered grid finite difference scheme is described in Chapter 1, the fault boundary condition in Chapter 2 (including the original thin zone method and the updated traction at split node method) and the free surface and absorbing boundary condition in Chapter 3. Additionaly, Chapter 2 contains Sections 2.4 and 2.5 describing laws of friction currently used in the dynamic modelling of earthquakes, and Section 2.6 describing the estimation of the cohesive zone.

The applicability of the code was further expanded by implementing the fast velocity weakening friction law (Section 2.5). This posed numerical complications, because additional differential equation needs to be solved at the fault boundary.

The accuracy of the new code FD3D_TSN was tested using two excercises (TPV5 and TPV104) from The SCEC/USGS Spontaneous Rupture Code Verification Project [Harris et al., 2009, 2018]. The comparison with the old thin zone version shows large improvement in the accuracy of physical quantities (slip and rupture velocity) and the shape of slip rate functions at chosen points on the fault. New code compares well with those of other authors (the solution of Barall [2009] was chosen as a reference in this thesis). Tests with various discretization steps Δh show that the difference between the solutions is around 1 percent in rupture velocity and slip when we use a discretization step $\Delta h = 100$m. This holds for both tests.

There is a large number of ways of further development from this work. Implementation of an irregular finite difference grid with finer discretization around the fault boundary could further improve accuracy/efficiency and might be necessary for studying more complex dynamic models like those including fault zones.

Studies of specific physical effects are also possible. Rupture models with fault

zones (layers of damaged material with lowered seismic velocities around the fault) might be an interesting venue of further expanding the complexity of our model. Also, tests with mostly homogenous parameters (like both benchmark excercises analyzed in this Thesis) show a strong secondary rupture front reflected from the free surface, which is a phenomenon not observed in real eartquakes [Kaneko et al., 2008], as studied by kinematic inversions. Mechanism stopping the rupture when using slip-weakening friction law while allowing slip at the free surface is unclear.

Dynamic inversion of real eartquakes using a rupture model with fast velocity friction is possible with the new code. It might still become limitated by the approximations in the dynamic model that were not adressed in this work – only planar and vertical fault is allowed in the simulation. Although the set of studiable events will be somewhat bounded by these limitations and large eartquakes on multiple faults like the 2016 Kaikoura earthquake ($M_w = 7.8$) are yet out of the scope of dynamic inversions, large number of events, for example the 2014 South Napa earthquake ($M_w = 6.0$) or the 2016 Central Italy earthquake ($M_w = 6.2$), can be studied succesfully promising significant new insight into the mechanics of the earthquake source.

Bibliography

K. Aki and P. G. Richards. *Quantitative Seismology, 2nd Ed.* University Science Books, 2002.

D. J. Andrews. A numerical study of tectonic stress release by underground explosions. *Bulletin of the Seismological Society of America*, 63(4), 1973.

D. J. Andrews. Rupture velocity of plane strain shear cracks. *Journal of Geophysical Research*, 81(32), 1976. doi: 10.1029/JB081i032p05679.

B. Barall. A grid-doubling finite-element technique for calculating dynamic three-dimensional spontaneous rupture on an earthquake fault. *Geophysical Journal International*, 178, 2009. doi: 10.1111/j.1365-246X.2009.04190.x.

Jean-Pierre Berenger. A perfectly matched layer for the absorption of electromagnetic waves. *Journal of Computational Physics*, 114(2), 1994. doi: 10.1006/jcph.1994.1159.

A. Bizzarri, H. S. Bhat, L. Dalguer, G. Festa, and A. Zollo. *The Mechanics of Faulting: From Laboratory to Real Earthquakes*. Research Signpost, 2012. ISBN 978-81-308-0502-3.

R. Clayton and B. Engquist. Absorbing boundary conditions for acoustic and elastic wave equations. *Bulletin of the Seismological Society of America*, 67, 1977.

Francis Collino and Chrysoula Tsogka. Application of the perfectly matched absorbing layer model to the linear elastodynamic problem in anisotropic heterogeneous media. *GEOPHYSICS*, 66, 2001. doi: 10.1190/1.1444908.

V. M. Cruz-Atienza, J. Virieux, and H. Aochi. 3d finite-difference dynamic-rupture modeling along nonplanar faults. *GEOPHYSICS*, 72(5), 2007. doi: 10.1190/1.2766756.

L. A. Dalguer and S. M. Day. Comparison of fault representation methods in finite difference simulations of dynamic rupture. *Bulletin of the Seismological Society of America*, 2006. doi: 10.1785/0120060024.

Luis A. Dalguer and Steven M. Day. Staggered-grid split-node method for spontaneous rupture simulation. *Journal of Geophysical Research: Solid Earth*, 112 (B2), 2007.

S. M. Day. *Finite element analysis of seismic scattering problems*. PhD thesis, California Univ., San Diego, 1977.

S. M. Day, L. A. Dalguer, N. Lapusta, and Y. Liu. Comparison of finite difference and boundary integral solutions to three-dimensional spontaneous rupture. *Journal of Geophysical Research: Solid Earth*, 110, 2005. doi: 10.1029/2005JB003813.

G. Di Toro, D. L. Goldsby, and T. E. Tullis. Friction falls towards zero in quartz rock as slip velocity approaches seismic rates. *Nature*, 2004. doi: 10.1038/nature02249.

J. H. Dieterich. A model for the nucleation of earthquake slip. *Washington DC American Geophysical Union Geophysical Monograph Series*, 37, 1986. doi: 10.1029/GM037p0037.

James H. Dieterich. Modeling of rock friction: 1. experimental results and constitutive equations. *Journal of Geophysical Research: Solid Earth*, 1979. doi: 10.1029/JB084iB05p02161.

E. M. Dunham, D. Belanger, L. Cong, and J. E. Kozdon. Earthquake ruptures with strongly rate-weakening friction and off-fault plasticity, part 1: Planar faults. *Bulletin of the Seismological Society of America*, 101, 2011. doi: 10.1785/0120100075.

Kenneth Duru and Eric M. Dunham. Dynamic earthquake rupture simulations on nonplanar faults embedded in 3d geometrically complex, heterogeneous elastic solids. *Journal of Computational Physics*, 305:185 – 207, 2016. doi: 10.1016/j.jcp.2015.10.021.

A.-A. Gabriel, J.-P. Ampuero, L. A. Dalguer, and P. M. Mai. The transition of dynamic rupture styles in elastic media under velocity-weakening friction. *J. Geophys. Res.*, 117, 2012. doi: 10.1029/2012JB009468.

M. Galis, P. M. Mai, C. Pelties, J. Kristek, P. Moczo, and J.-P. Ampuero. On the initiation of sustained slip-weakening ruptures by localized stresses. *Geophysical Journal International*, 200(2), 2014. doi: 10.1093/gji/ggu436.

F. Gallovic, L. Valentova, J.-P. Ampuero, and A.-A. Gabriel. Bayesian dynamic finite-fault inversion: 1. method and synthetic test. *EarthArXiv*, 2019. doi: https://doi.org/10.31223/osf.io/tmjv4.

D. L. Goldsby and T. E. Tullis. Flash heating leads to low frictional strength of crustal rocks at earthquake slip rates. *Science*, 334(6053), 2011. doi: 10.1126/science.1207902.

Ellen Gottschämmer and K. B. Olsen. Accuracy of the explicit planar freesurface boundary condition implemented in a fourth-order staggered-grid velocity-stress finite-difference scheme. *Bulletin of The Seismological Society of America - BULL SEISMOL SOC AMER*, 91:617–623, 2001. doi: 10.1785/0120000244.

R. W. Graves. Simulating seismic wave propagation in 3d elastic media using staggered-grid finite differences. *Bulletin of the Seismological Society of America*, 86:1091–1106, 08 1996.

A. R. Harris, K. Bai, and J. P. Ampuero. A suite of exercises for verifying dynamic earthquake rupture codes. *Bulletin of the Seismological Society of America*, 2018.

R. Harris, M. Barall, R. Archuleta, E. Dunham, B. T. Aagaard, Jean Paul Ampuero, H. Bhat, V. Cruz-Atienza, L. Dalguer, P. Dawson, S. Day, Duan , G. Ely, Y. Kaneko, Y. Kase, N. Lapusta, Y. Liu, S. Ma, D. Oglesby, and E. Templeton. The scec/usgs dynamic earthquake rupture code verification exercise. *Seismological Research Letters*, 80, 2009. doi: 10.1785/gssrl.80.1.119.

C. Herrera, S. Ruiz, R. Madariaga, and P. Poli. Dynamic inversion of the 2015 jujuy earthquake and similarity with other intraslab events. *Geophysical Journal International*, 02 2017. doi: 10.1093/gji/ggx056.

R. L. Higdon. Absorbing boundary conditions for elastic waves. *GEOPHYSICS*, 56(2), 1991. doi: 10.1190/1.1443035.

Yoshiaki Ida. Stress concentration and unsteady propagation of longitudinal shear cracks. *Journal of Geophysical Research*, 1973. doi: 10.1029/JB078i017p03418.

Y. Kaneko, N. Lapusta, and J.-P. Ampuero. Spectral element modeling of spontaneous earthquake rupture on rate and state faults: Effect of velocity-strengthening friction at shallow depths. *Journal of Geophysical Research: Solid Earth*, 113(B9), 2008. doi: 10.1029/2007JB005553.

Dimitri Komatitsch and Roland Martin. An unsplit convolutional perfectly matched layer improved at grazing incidence for the seismic wave equation. *GEOPHYSICS*, 72, 2007. doi: 10.1190/1.2757586.

Jozef Kristek, Peter Moczo, and Ralph J. Archuleta. Efficient methods to simulate planar free surface in the 3d 4th-order staggered-grid finite-difference schemes. *Studia Geophysica et Geodaetica*, 46(2), 2002. doi: 10.1023/A:1019866422821.

Jozef Kristek, Peter Moczo, and Martin Galis. A brief summary of some pml formulations and discretizations for the velocity-stress equation of seismic motion. *Studia Geophysica et Geodaetica*, 53(4), 2009. doi: 10.1007/s11200-009-0034-6.

Alan R. Levander. Fourth-order finite-difference p-sv seismograms. *GEOPHYSICS*, 53(11), 1988. doi: 10.1190/1.1442422.

R. Madariaga. Dynamics of an expanding circular fault. *Bulletin of the Seismological Society of America*, 66(3), 1976. ISSN 0037-1106.

R. Madariaga, K B. Olsen, and R. Archuleta. Modeling dynamic rupture in a 3d earthquake fault model. *Bulletin of the Seismological Society of America*, 88, 10 1998.

A. Mirwald, V. M. Cruz-Atienza, J. Díaz-Mojica, A. Iglesias, S.K. Singh, C. Villafuerte, and J. Tago. The 19 september 2017 (mw7.1) intermediate-depth mexican earthquake: A slow and energetically inefficient deadly shock. *Geophysical Research Letters*, 46(4), 2019. doi: 10.1029/2018GL080904.

P. Moczo, J. Kristek, and L. Halada. 3d fourth-order staggered-grid finite-difference schemes: Stability and grid dispersion. *Bulletin of the Seismological Society of America*, 90(3), 2000. doi: 10.1785/0119990119.

P. Moczo, J. Robertsson, and L. Eisner. The finite-difference time-domain method for modeling of seismic wave propagation. *Advances in Geophysics*, 48, 2007. doi: 10.1016/S0065-2687(06)48008-0.

Ch. Pelties, Y. Huang, and J.-P. Ampuero. Pulse-like rupture induced by three-dimensional fault zone flower structures. *Pure and Applied Geophysics*, 172(5), 2015. doi: 10.1007/s00024-014-0881-0.

Z. Reches and D. A. Lockner. Fault weakening and earthquake instability by powder lubrication. *Nature*, 2010. doi: 10.1038/nature09348.

J. R. Rice. Heating and weakening of faults during earthquake slip. *Journal of Geophysical Research: Solid Earth*, 111, 2006. doi: 10.1029/2005JB004006.

O. Rojas, E. M. Dunham, S. M. Day, L. A. Dalguer, and J. E. Castillo. Finite difference modelling of rupture propagation with strong velocity-weakening friction. *Geophysical Journal International*, 179(3), 2009. doi: 10.1111/j.1365-246X.2009.04387.x.

A. Ruina. Slip instability and state variable friction laws. *Journal of Geophysical Research*, 881, 1983. doi: 10.1029/JB088iB12p10359.

T. Ulrich, A.-A. Gabriel, J.-P. Ampuero, and W. Xu. Dynamic viability of the 2016 mw 7.8 kaikōura earthquake cascade on weak crustal faults. *Nature Communicationsvolume*, 10, 2019. doi: 10.1038/s41467-019-09125-w.

J. Virieux. P-sv wave propagation in heterogeneous media: Velocity-stress finite-difference method. *GEOPHYSICS*, 51, 1986. doi: 10.1190/1.1442147.

S. Wollherr, A.-A. Gabriel, and C. Uphoff. Off-fault plasticity in three-dimensional dynamic rupture simulations using a modal Discontinuous Galerkin method on unstructured meshes: implementation, verification and application. *Geophysical Journal International*, 214, 2018. doi: 10.1093/gji/ggy213.

List of Figures

List of Tables